Alma Mater Studiorum · University of Bologna

School of Science
Department of Physics and Astronomy
Master Degree in Astrophysics and Cosmology

Incidence of afterglow plateaus in gamma-ray bursts associated with binary neutron star mergers

Graduation Thesis

Supervisor:
Prof. Marcella Brusa

Co-supervisors:
Dr. Giulia Stratta
Dr. Simone Dall'Osso

Presented by:
Luca Guglielmi

Academic Year 2022/2023
Graduation date IV

Abstract

Gamma-ray bursts (GRBs) have been a great astrophysical mystery since their discovery in the late 60's. It was only in the early 90's that high-energy telescopes (e.g. BATSE, *BeppoSAX*) unveiled their cosmological origin and then discovered the X-ray afterglows which follow the main γ-ray events.

A new breakthrough came with the *Swift* satellite which was able to observe the X-ray afterglow at unprecedentedly early times. This led to a flurry of discoveries, and to the definition of a "canonical shape" for X-ray afterglow light-curves, likely reflecting the changing physical conditions in the emitting region: an initial steep decay marking the switching off of the prompt emission, followed by a shallow phase (so-called "plateau") which then transitions to a characteristic power-law flux decay. While the latter is in agreement with the theory of synchrotron emission by a relativistic shock, the plateau could not be explained in the same framework, requiring additional physics.

Plateaus occur in $\sim 50\%$ of long GRBs, *i.e.* those associated to the collapse of massive stars. Short GRBs (SGRBs), associated to binary neutron star (BNS) mergers (and possibly neutron star-black hole mergers), proved harder to study: to date, the frequency of plateaus in SGRBs is uncertain.

In this Thesis, we study the most complete sample of SGRBs with known redshift, in order to confidently identify or rule out the presence of a shallow phase in each of them, and to derive physical constraints on its origin. The sample contains 85 bursts detected by *Swift* from May, 2005 to December, 2022: for each GRB, a detailed analysis of the X-ray afterglow light-curve is carried out. Our study finds 15 SGRBs with a robust plateau in their X-ray afterglow light-curve, implying a "plateau" fraction $0.176 < f_{\rm plateau} < 0.375$.

The 15 SGRBs were used to test the magnetar model, one of the leading theoretical interpretations for the plateau in terms of an extra energy injection in the afterglow shock, due to magnetic dipole radiation of a millisecond-spinning magnetar which was formed in the BNS merger producing the SGRB. Fitting X-ray afterglow light-curves with the magnetar model we estimated the magnetar birth spin period (P) and dipole magnetic field (B): 12 bursts gave good magnetar candidates, with parameters perfectly in line with theoretical expectations ($P \sim 1-10$ ms, $B \sim 10^{14}-10^{15}$ G), implying a magnetar fraction $0.141 < f_{\rm mag} < 0.245$. Interestingly, 3 of the 15 SGRBs were inconsistent with the magnetar model, and call for further study.

Finally, we used $f_{\rm mag}$ to constrain the maximum mass $M_{\rm max}$ of a stable NS in the framework of the magnetar model, assuming that *(i)* all SGRBs originate from BNS mergers, and *(ii)* only stable NS remnants can be associated to

X-ray plateaus whose typical duration is $\sim 10^3$ s. In this case, $f_{\rm mag}$ reflects exactly the fraction of stable NS formed in BNS mergers. By simulating a population of 10^5 mergers, with a characteristic mass distribution for both NS components, we derive a range of values for $M_{\rm max}$ corresponding to the $f_{\rm mag}$ range found above, namely $2.20 < M_{\rm max}/{\rm M}_\odot < 2.31$. Our result could be tested by the upcoming scientific runs of *Advanced* LIGO and *Virgo*, and may be directly confirmed with the advent of the *Einstein Telescope*, which will be able to observe a large population of BNS mergers.

Contents

Chapter 1

Gamma-ray bursts

Gamma-ray bursts (GRBs) are one of the most intriguing events in modern high energy astrophysics. One of the reasons making them so compelling is that they represent the most luminous known phenomena in the Universe spanning a redshift range from the local Universe to $z \sim 9$ (as GRB 090429B, Cucchiara et al., 2011), making them very important cosmological probes too. Indeed, despite the fact that they originate in extremely compact regions (of sizes $\lesssim 10^2$ km), they release huge amounts of energies (up to $\sim 10^{52}$ ergs) in extremely short time scales (ranging from less than 1 s to $\sim 10^2$ s). Moreover, thanks to the recent association of GRB 170817 with the binary neutron star (BNS) merger GW 170817, observed in gravitational waves (GW) by the *Advanced LIGO/Virgo* detectors, GRBs have heralded the new era of multi-messenger astrophysics.

In the following, we provide a brief historical introduction and a summary of the main theoretical results that were fundamental for the work carried out in this Thesis.

1.1 Historical context

GRBs were serendipitously discovered by the Vela military satellite system in the late 1960s. The original aim of these satellites, launched by the U.S. Department of Defense, was to monitor nuclear activity of the Soviet Union and prevent the detonation of nuclear devices in space, safeguarding the Nuclear Test Ban Treaty. On July 2, 1967 the very first GRB was detected, GRB670702, but the first paper about this discovery was published only six years later (Klebesadel et al., 1973), likely because of the complicated analysis process.

In the same years, two other new types of objects were discovered: Active Galactic Nuclei (AGN) and neutron stars (NS). While research on these latter sources saw a rapid progress, the theoretical understanding of GRBs proceeded extremely slowly. Indeed, the gamma-ray detectors available in that period had poor spatial resolution, making it impossible to identify electromagnetic counterparts at lower energies for GRBs. Consequently, even though more than 500 GRBs were detected in the eighteen years from 1973 to 1991, they remained mysterious phenomena and a huge number of theories and models were proposed to interpret them (e.g. Colgate, 1974; Ruderman, 1975).

A first step forward occurred in 1991 thanks to the Burst And Transient Source Experiment (BATSE), one of the four instruments carried by the Compton Gamma-Ray Observatory (*CGRO*). BATSE managed to detect thousands of GRBs (Fourth BATSE Gamma-Ray Burst Catalog, Paciesas et al., 1999), and even though it was not possible to find a low-frequency counterpart for any of them, it allowed to make great improvements in understanding their nature. In particular, the all-sky survey showed that GRBs were isotropically distributed, suggesting for the first time their cosmological origin. Moreover, the observed bimodal distribution of burst duration (Kouveliotou et al., 1993, see Section 1.2) gave strong confirmation to the previously only hypothesized existence of two separate classes of GRBs: the *long* and the *short* GRBs, with a clear separation around ~ 2s.

The real barrier that prevented a further comprehension of GRBs was the lack of information about distances, something that could be obtained only after finding a counterpart at longer wavelengths. This indeed was achieved in 1997 thanks to the Italian-Dutch *BeppoSAX* satellite for X-ray astronomy, that featured a wide-field X-ray camera with a much better localization capability relative to γ-ray detectors: in this way, it was possible to find the first X-ray counterpart of a GRB (GRB 970228, Costa et al., 1997). This counterpart was called *afterglow*, using the name that was previously given to it in a theoretical work by P. Meszaros and Rees (1993). Thanks to this discovery, optical and radio afterglows were observed for the first time too, and this eventually led to the first accurate identification of the host galaxy and to the first measurement of a GRB redshift ($z = 0.835$ for GRB 970508) (M. R. Metzger et al., 1997), confirming their cosmological origin. This new possibility of carrying out multi-wavelength observations of GRBs allowed a deeper comprehension of the physics underlying these events and led to the association, for the first time, of a long GRB with the death of a special category of massive stars (Type Ic supernova, Galama et al., 1998).

Another breakthrough was achieved in 2004 when the *Swift* observatory was launched (Gehrels, Chincarini, et al., 2004). The unique feature of *Swift* (that has been officially renamed Neil Gehrels Swift Observatory in 2015) is that it carries a γ-ray, an X-ray and a UV telescope all together on the same satellite, with an extremely fast automatic repointing of the X-ray and optical-UV telescopes every time that a burst is observed by the γ-ray detector Burst Alert Telescope (BAT). *Swift* made it possible to study the faint afterglow of short GRBs, something that was not viable before its launch. This led to the realisation that short GRBs are indeed not linked to the death of massive stars as long GRBs, but more likely to the coalescence of two neutron stars or a black hole and a neutron star. Moreover, by its ability to carry out much earlier observations of GRB afterglows than ever before, *Swift* demonstrated that the separation between long and short GRBs is not so sharp, presenting some degree of overlap at the interface between the two duration distributions.

The launch of *Fermi* Gamma-Ray Space Telescope in 2008 increased even more the number of GRBs that were to be discovered from that year on. In particular, thanks to its two main instruments, the Large Area Telescope (LAT: 20 MeV−300 GeV) and the Gamma-ray Burst Monitor (GBM: 8 keV−40 MeV), *Fermi* allowed to study the spectral properties of GRB prompt emission in an unprecedented detail, covering more than 7 orders of magnitude in the high energy range and leading to the discovery of > 100 MeV emission (or simplified as "GeV" emission) in several GRBs (Ackermann et al., 2010). Nevertheless, it is important to recall that *Fermi* GRBs are poorly localized (Meegan et al., 2009).

In 2017, the theories predicting that short GRBs were associated to the coalescence of compact binary systems, and should thus be sources of copious GWs, were finally confirmed: the detection of the binary neutron star merger GW 170817, made by the interferometers *LIGO* and *Virgo*, and its direct association with GRB 170817 (see Section 1.4) formally marked the beginning of the "multi-messenger era" of GRBs (Abbott et al., 2017).

1.2 Standard classification

Even though at the time BATSE was launched the theoretical understanding of GRBs was still in an early stage, the great number of events observed by BATSE allowed to discover a bimodality in the GRBs duration distribution (Kouveliotou et al., 1993). Upon defining T_{90} as the time interval between the instants at which 5% and 95% of the total fluence[1] are detected, the distribution of the GRBs observed by BATSE showed a clear bimodality

---

[1] The fluence is defined as the time integral of the flux and is expressed in units of erg cm^{-2}

(Fig. 1.1a): the dip around $T_{90} \sim 2$ s suggested a distinction between short GRBs (SGRBs, with T_{90} peaking at 0.2–0.3 s) and long GRBs (LGRBs, with T_{90} peaking at 20–30 s).

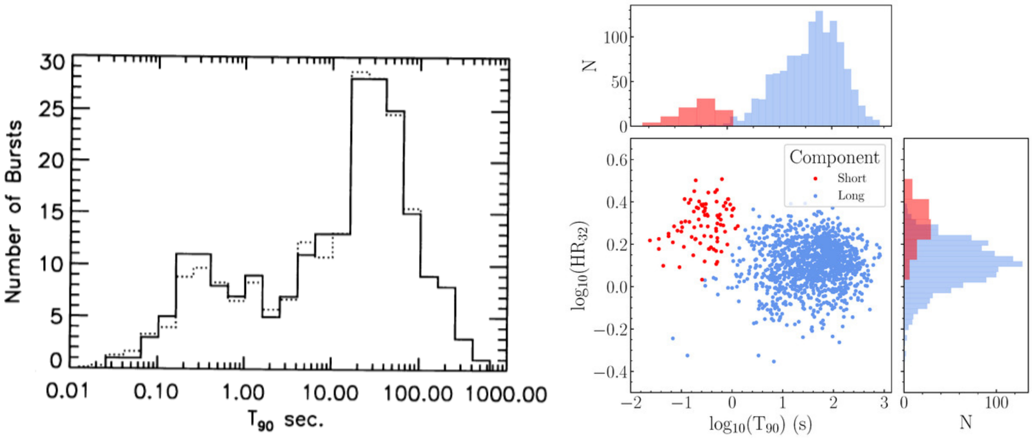

(a) **(b)**

Figure 1.1: **(a)** Distribution of T_{90} for the 222 GRBs of the first BATSE catalog. Solid line is the histogram of raw data, while dotted line is the error-convolved histogram, obtained considering for each T_{90} a Gaussian with width δT_{90} and adding to each bin the overlapping areas of all the Gaussian falling within the bin boundaries (Kouveliotou et al., 1993). **(b)** 2D diagram reporting T_{90} on the x-axis and the hardness ratio HR_{32}, calculated in the energy range 3 $(50 - 100$ keV) and energy range 2 $(25 - 50$ keV), on the y-axis, using data from the Third Swift/BAT Catalogue (1388 burst, Lien et al., 2016): it is evident how the bimodality of bursts is not only in duration but also in the softness/hardness of the prompt emission, with SGRBs (in red) appearing on average harder with respect to LGRBs (in blue, Salmon et al. (2022)).

It is important to keep in mind that, as explained by Kumar and B. Zhang (2015), T_{90} is an arbitrary definition and it is very subjective: it strongly depends on the sensitivity and energy range of the instruments, it does not take into account the differences in redshift between the different bursts, it does not discriminate between prompt emission and early afterglow emission and between different light-curves morphologies. Nevertheless, T_{90} is the most commonly used parameter to describe the duration of GRB main (prompt) emission. Contextually, a bimodality in the GRB hardness ratio (HR) distribution was also discovered, with long GRBs being on average softer than SGRBs[2] (see Fig. 1.1b). This resulted in a further and more complete (but not ultimate) classification into the two classes "long/soft"

---

[2] We recall that the hardness ratio (HR) is the normalized difference of the counts in two different energy bands A (high energy) and B (low energy), and it is typically defined as $\mathrm{HR} = (A - B)/(A + B)$.

and "short/hard" GRBs.

Swift observations introduced a revolution in the field, enabling multi-wavelength studies that demonstrated that these two GRB classes were associated to two different source classes, which were linked to two types of progenitor systems (but its important to point out that the progenitor class is not univocally defined by the duration).

Long GRBs were the first class for which the nature of the progenitor was discovered: they were proposed to originate during the death of a special type of massive stars, as proposed for the first time by S. E. Woosley (1993). This was confirmed for the first time in 1998, when a Type Ic supernova[3] discovered in a nearby galaxy at $z = 0.0085$, SN 1998bw, was found out to lie in the error box of GRB 980425, a burst detected by *BeppoSAX* (Galama et al., 1998). Initially, this was classified as just a "probable" association, but this hypothesis was later strengthened by the discovery that long GRBs are mainly found in regions of intense star formation in distant galaxies (Paczyński, 1998) and by observing the presence of 'bumps' in the optical afterglow light-curves attributable to a supernova (Castro-Tirado, A. J. & Gorosabel, J., 1999). All these observations supported but did not conclusively prove the association between the death of massive stars and LGRBs. Eventually, the first strong evidence was obtained by Hjorth et al. (2003), with the discovery of a very energetic supernova light-curve, SN 2003dh, emerging from the afterglow of GRB 030329, at $z = 0.1685$: they were temporally and spatially coincident, and this conclusively confirmed the association.

In the following years, the *Swift* satellite led to the detection of a large number of short GRBs and, in particular, of their faint afterglows. This allowed the association of SGRBs with their host galaxies, showing a larger heterogeneity with respect to the LGRBs hosts. In particular, Gehrels, Sarazin, et al. (2005) discovered that the short burst GRB 050509b was located in close proximity of an elliptical, non star-forming galaxy at z=0.225: this was very different from what observed for long GRBs and was instead expected if short GRBs were originated from an evolved progenitor system, not associated to recent star formation, like a population of compact objects binary systems. In support of this hypothesis, the fact that SGRBs occur on average five time farther from the center of their host galaxies compared to LGRBs (W. Fong, Berger, & Fox, 2010) is consistent with progenitors like compact object binaries, that have a long time (typically of the order of $0.1 - 10$ Gyr,

---

[3] A Type Ic supernova is a supernova for which the spectrum lacks hydrogen lines present instead in Type II, silicon lines present instead in Type Ia and helium lines present instead in Type Ib: essentially, they are originate by star which lost most of their envelope before the collapse.

Eichler et al., 1989; Nakar, 2007) to travel far from the galactic center before merging. Recently, the discovery of the BNS merger GW 170817 made by *Advanced LIGO* and *Virgo* detectors, of its associated GRB 170817 made by *Fermi* GBM, and of its multi-wavelength counterparts from X-ray to radio bands, provided a spectacular confirmation of the compact binary scenario. A deeper analysis of this GW 170817 will be given in Section 1.4. Today the leading model proposes short GRBs to be consistent with the coalescence between two neutron stars (NS-NS) or between a neutron star and a black hole (NS-BH), as theorized at first in Paczynski (1986) and Eichler et al. (1989).

Several works have proposed, even until recent years (Mukherjee et al., 1998; Ripa and A. Meszaros, 2015), that a third class of events in the T_{90} distribution might exist, so-called intermediate GRBs. However there is no clear evidence that this additional class has a distinct physical origin.

The continuous detection of new GRBs has led to the conclusion that this classification is by the way too simplistic to account for the heterogeneity of these events. In a large number of cases, it is not possible to securely fit an event in one of the two categories presented above. Two main exceptions to the "long/soft" and "short/hard" classification are reported in the following.

1.2.1 Ambiguities in the standard classification

In 2006, the *Swift* satellite detected GRB 060614, at $z = 0.125$: its duration of $T_{90} = 102$ s left no doubt in classifying it as a long GRB. However, observing it in more detail, it was not possible to associate to it any supernova light-curve (as expected for long GRBs) despite its low redshift and, moreover, it showed many features typical of short GRBs (like its low luminosity, Gehrels, Norris, et al., 2006). In addition to that, it was also associated with a kilonova-like feature (Yang et al., 2015), which is a type of emission expected in the case of a binary neutron star merger. This led to classifying it in a class called "hybrid GRBs", which are characterized by a long duration but lack the association with a supernova.

An even more striking case is represented by GRB 211211A, at $z = 0.0763$: it was characterized by an undoubtedly long duration (~ 60 s), but the lack of an association with a supernova emission and several other short GRB-like features made it another case of hybrid GRB. Additionally, a kilonova emission was later possibly associated to this GRB (Rastinejad et al., 2022), adding evidence to the scenario according to which compact merger events can give birth to long γ-ray emission too.

Extended emission (EE) SGRBs

The standard classification is complicated even further if we consider a fraction of short GRBs which, after the initial short/hard spike, occasionally show a softer and prolonged emission, lasting tens of seconds: these are labelled as short GRBs with extended emission (SEE, Norris and Bonnell, 2006; Norris, Gehrels, et al., 2010). EE is characterized by a very strong flux and spectral time variability. In particular, during EE the value of the photon index Γ is expected to increase: this means that the power-law spectrum is becoming stepper and this is commonly referred to as "spectral softening", because less high energy photons are produced. The apparently long duration make SEE similar to LGRBs but during the first seconds, corresponding to the spike phase, they show spectral features that are likely associated to SGRBs. In this perspective, EE is often interpreted as the component of the prompt emission coming from larger angles that, because of relativistic effects, takes more time to reach us and thus is observed at later times. These ambiguous cases are not well understood yet, but discovering their origin could provide powerful means to deeper understand the nature of GRBs progenitors.

1.3 Theoretical framework

Gamma-ray bursts are the most powerful explosions in the Universe (Band et al., 1993; Kouveliotou et al., 1993; P. Meszaros, 2006). The advent of *BeppoSAX* in 1997 made it evident that these extreme events can happen at enormous distance from us and the fact that we are able to observe them even from cosmological distances (the most distant burst ever detected is GRB 090429B at $z = 9.4$, Cucchiara et al., 2011) ascertained the fact that GRBs are originated by the sudden release of a huge amount of energy, even capable to outshine their host galaxy, on very small scales (suggesting the stellar origin of their progenitors).

This vast and concentrated energy release gives rise to two types of emission. Prompt gamma-rays, having markedly a non-thermal spectrum, are thought to originate from internal shocks within a relativistic outflow. The same outflow later impacts against the external medium, driving a relativistic forward shock into it, which sweeps up the circumburst material until it eventually starts to decelerate, giving rise to the long-lived emission called afterglow (Fig. 1.2). The following sections provide a schematic description of the physics behind prompt and afterglow emissions.

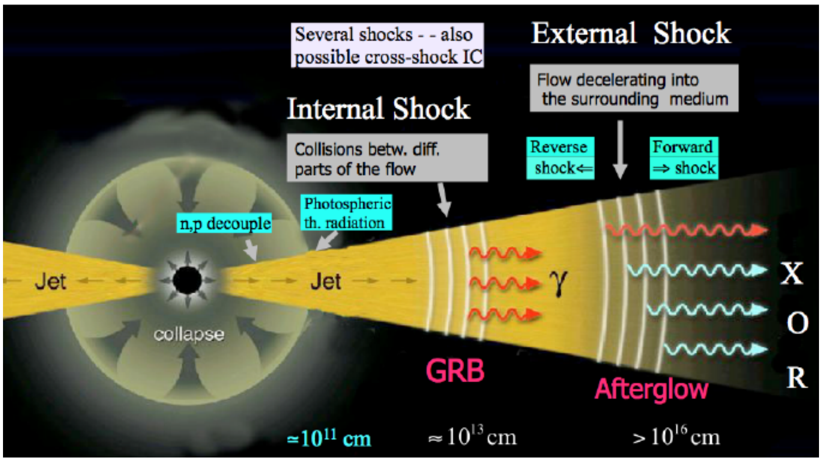

Figure 1.2: Cartoon portraying the GRB fireball model. Here, the event is generated by the collapse of a massive star, while the cases of binary neutron stars merger or neutron star-black hole merger are not shown. A huge amount of energy is funneled into a jet ("fireball"). Part of the jet kinetic energy is dissipated by internal shocks, producing the gamma-ray "prompt" emission (red arrows). When the jet impacts with the surrounding medium, external shocks are generated, the remaining kinetic energy heats up the medium and produces emission at lower frequencies (X-ray, optical and radio, orange and light blue arrows), that is what is commonly called "afterglow" (Mészáros & Rees, 2014).

1.3.1 Prompt emission and fireball model

The prompt emission is the primary component of GRBs and the one that was first discovered in the '60s. A good definition of the prompt emission is given in B. Zhang (2018): *"the prompt emission is the temporal phase during which excessive sub-MeV emission is detected by the GRB triggering detectors above the instrumental background emission level"*. The T_{90} (Section 1.2) is typically used to characterize the duration of this phase but what strikes mostly in the prompt light-curves of GRBs is their diversity: some appear to be very smooth while others show a strong time variability on very short timescales, together with the presence of several peaks, and the values of T_{90} span a wide from milliseconds to thousands of seconds, as shown for example in Fig 1.3.

The few salient features mentioned above make already possible to infer important constraints on the physics underlying GRB emission. Starting from the short timescale variability and using causality arguments, one can easily prove that the gamma-ray production must happen in a very compact region: indeed, supposing a temporal variability on timescales $\delta T = 10$ ms, it is reasonable to impose as an upper limit to the source scale $R_i < c\delta T \simeq 3000$ km. This is the starting assumption of the so called "fireball model", first proposed by Cavallo and Rees (1978). This model predicts that a fireball

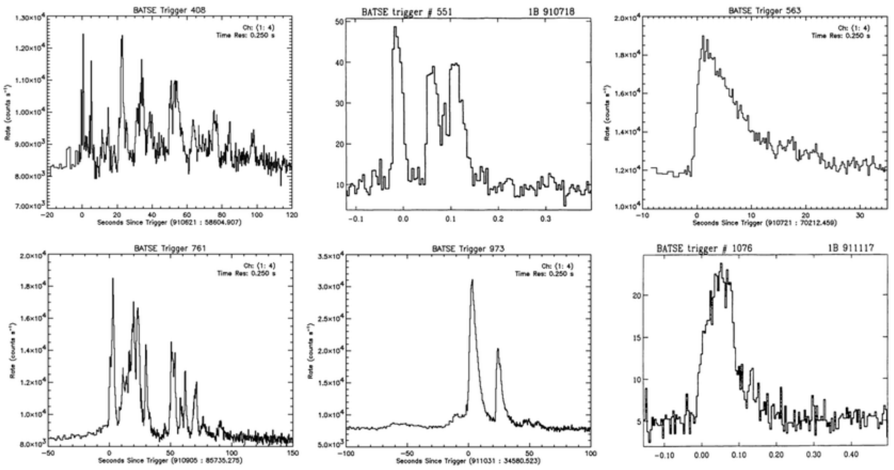

Figure 1.3: GRB light-curves of the prompt emission of some of the bursts detected during the BATSE mission: it is clear how each burst has its own peculiar time evolution, showing a clear heterogeneity of features (Fishman et al., 1994).

concentrated in such a compact region would imply photon energies so large to make it opaque to radiation due to electron positron pair creation: this would mean that the fireball would expand and cool up to the point at which the photon energy goes below the pair production limit, making the outflow optically thin and allowing a soft thermal spectrum to emerge. As the spectrum we observe from GRBs is non thermal and typically quite hard spectrally, this discrepancy is what has become known as the "GRB compactness problem".

To solve the compactness problem, we must take into account relativistic effects (Piran, 1999). Let us consider a source with fluence S at a distance D: the energy output we expect from this source will be given by:

$$E = 4\pi D^2 S = 10^{50}\mathrm{ergs}\left(\frac{D}{3000\,\mathrm{Mpc}}\right)^2\left(\frac{S}{10^{-7}\,\mathrm{ergs\,cm^{-2}}}\right), \tag{1.1}$$

where cosmological effects can be neglected in first approximation. From observations we know that the observed spectrum contains a large number of high energy γ-ray photons. Suppose a high energy photon (with energy E_1) interacts with a lower energy photon (with energy E_2): if $\sqrt{E_1 E_2} > m_e c^2$ they will produce electron positron pair via the pair production process $\gamma\gamma \rightarrow e^+e^-$. If we call f_p the fraction of photons matching this condition, we can express the average optical depth of this process as:

$$\tau_{\gamma\gamma} = \frac{f_p \sigma_T S D^2}{R_i^2 m_e c^2}. \tag{1.2}$$

where σ_T is the Thomson cross-section while $R_i < c\delta T$ is the approximate size of the source derived from causality arguments, starting from its temporal variability δT. And here is exactly were the problem arises: this optical depth is extremely large, so we should expect that photons are not able to escape up to a certain point at which they will give origin to a thermal spectrum, while what we observe is instead a non-thermal spectrum that suggests us that the source must be optically thin to such high energy photons.

This apparent contradiction can be solved if we suppose that the source of radiation (the fireball) is moving towards us with a relativistic velocity v, so that the Lorentz factor $\gamma = \sqrt{1 - v^2/c^2} \gg 1$. This would imply that the photons we observe are blue shifted and their energy at the source is $h\nu_{\text{obs}}/\gamma \ll h\nu_{\text{obs}} = E_{\text{obs}}$ (h is the Planck constant): this means that fewer photons will be able to undergo pair production, in particular the fraction of photons that could produce pairs at the source will be $f_p \gamma^{-2\alpha}$ where α is the high-energy photon spectral index (see Eq. 1.4). At the same time, the scale of the emitting region will be larger by a factor γ^2 with respect to the original estimate R_i, because of relativistic effects[4]. The new expression for the optical depth will be then given by:

$$\tau_{\gamma\gamma} = \frac{f_p}{\gamma^{(2\alpha+4)}} \frac{\sigma_T S D^2}{R_i^2 m_e c^2} \simeq \frac{10^{13}}{\gamma^{(2\alpha+4)}} f_p \left(\frac{S}{10^{-7}\,\text{ergs}\,\text{cm}^{-2}} \right) \left(\frac{D}{3000\text{Mpc}} \right)^2 \left(\frac{\delta T}{10\text{ms}} \right)^{-2}. \quad (1.3)$$

One can then show that the compactness problem can be solved if the fireball is moving towards us with a Lorentz factor $\gamma > 10^{13}/\gamma^{(2\alpha+4)} \simeq 10^2$.

The solution to the compactness problem imposes the requirement that the emitting region should have relativistic motion. However, in order to observe gamma-rays, the huge kinetic energy of this outflow must be somehow converted to radiation, and this can be achieved in two ways. If the relativistic outflow contains baryonic material (*baryon loading*), internal shocks within the outflow itself are expected to dissipate part of the kinetic energy of the baryons transferring it to the electrons, which will then irradiate it efficiently through fundamental mechanisms (synchrotron, Inverse Compton (IC) scattering). The alternative is that this conversion happens via magnetic reconnection events, which however require an electromagnetically dominated outflow to take place, and so a relatively low baryon loading contribute (Usov, 1992). As already stated above, a pure pair-photon bubble would produce a nearly thermal spectrum and would not let high-energy photons to escape.

---

[4] If relativistic matter is beamed (see Section 1.3.3) we can define the jet angle $\theta_j = 1/\gamma$ and the upper limit on the radius will also have to take into account the beaming correction, so that $R_i' < c\delta t(1 - \cos\theta_j) \sim c\delta t\,\theta_j^2/2 = c\delta t/(2\gamma^2)$.

Even though a conclusive interpretation of the mechanisms responsible for GRBs prompt emission is still eluding us, Band et al. (1993) were able to derive, analyzing a large number of BATSE GRBs, an empirical function that faithfully describes the spectrum of the prompt, the so called *Band function* (or *GRB function*). It consists of a smoothly-joined broken power-law with an exponential cut-off at low energies. The photon spectrum is expressed as:

$$N_E(E) = \begin{cases} A\left(\frac{E}{100\mathrm{keV}}\right)^{\alpha} \exp(-\frac{E}{E_0}), & E < (\alpha-\beta)E_0, \\ (A\left(\frac{(\alpha-\beta)E_0}{100\mathrm{keV}}\right)^{\alpha-\beta} \exp(\beta-\alpha)\left(\frac{E}{100\mathrm{keV}}\right)^{\beta}, & E > (\alpha-\beta)E_0, \end{cases} \tag{1.4}$$

where A is a normalization constant, α and β are both negative and represent the low-energy and high-energy photon spectral indices respectively[5], while E_0 is the break energy which separates the two power-law slopes.

Despite the apparent universality of the Band function, the two spectral indices α, β and the break energy E_0 do show a relatively wide dispersion within the GRB population. In the bright BATSE GRBs (which consist of a total of 156 bursts with 5500 spectra) the two spectral indices are distributed around the values $\alpha \sim -1 \pm 1$ and $\beta \sim -2^{+1}_{-2}$ (Preece et al., 2000), while the peak energy $E_p = (2+\alpha)E_0$ is primarily concentrated in the 200−300 keV range (Preece et al., 2000; Goldstein, Preece, et al., 2013). These values were roughly confirmed in more recent works: Tsvetkova, Frederiks, Golenetskii, et al. (2017), analyzing the Konus-Wind catalog, found distributions of the indices peaking around the values $\alpha \sim -1$ and $\beta \sim -2.5$, while the distributions derived by Poolakkil et al. (2021) studying the bursts detected by the Fermi Gamma-Ray Burst Monitor (GBM) peaked around the values $\alpha \sim -1.1$ and $\beta \sim -2.1$.

The *Band function* is still the best analytical model to date capable of reproducing accurately the spectral shape of the prompt emission, although a satisfactory theoretical interpretation is still lacking.

1.3.2 Afterglow emission

Even though before the launch of *BeppoSAX* in 1997 no instrument had ever observed GRBs emission outside the gamma-rays, theoretical work already predicted the existence of emission at lower energies: Mészáros and Rees (1997) assumed an extragalactic origin of GRBs and discussed how relativistic *internal shocks* would be originated within the relativistic outflow

---

[5] These should not be confused with the indices used in Section 1.3.2 for the temporal evolution of the flux density of the afterglow, $F_\nu(t,\nu) \propto t^{-\alpha}\nu^{-\beta}$, where α is the temporal decay index while β is the flux density spectral index. Despite the ambiguity of this notation, we keep the conventions widely adopted in the literature.

by the time variation of the Lorentz factor of the ejecta and would dissipate a fraction of the bulk kinetic energy. Moreover, this relativistically expanding material would eventually hit the surrounding medium, often defined circumburst medium (CBM), and this belated interaction would drive an *external shock* in the CBM, leading to particle acceleration and local magnetic field amplification. This would create the perfect conditions for the release of the (external) shock kinetic energy via synchrotron emission, over a longer timescale and over a wide range of lower energies, from X-rays to the optical, infrared and radio band: this is commonly referred to as the GRB *afterglow*. This prediction was soon after confirmed on February 28, 1997 when *BeppoSax* observed the X-ray afterglow associated to GRB 970228 (Costa et al., 1997).

Prior to the launch of the Neil Gehrels *Swift* observatory in 2004 (see Section 2.1), the study of X-ray afterglows proved to be extremely difficult because of the elapsed time between the detection of the prompt gamma-rays and the pointing of an X-ray telescope in the same direction. Thanks to the rapid slewing capability of the X-ray telescope (XRT) onboard *Swift*, revolutionary results were achieved: indeed, more than 95% of *Swift* GRBs turned out to have an X-ray afterglow, with a very peculiar light-curve evolution starting at early times. Just six months after *Swift* started its activity, an observational canonical X-ray afterglow light-curve was proposed by B. Zhang, Fan, et al. (2006), identifying five different characteristic phases of the afterglow (see Fig. 1.4).

In the following years, several systematic studies were carried out to disentangle the physical origin of each phase and, from these preliminary studies, the hypothesis that the prompt emission and the afterglow are originated by two different physical phenomena was confirmed by strong evidence coming from the early-time afterglow data. This led to the association of the prompt emission with internal shocks occurring within the jet, as result of the collisions between relativistic shells with different Lorentz factors Γ, while afterglow emission was instead connected to external shocks originated by the interaction between the jet and the external medium.

The theory behind acceleration mechanisms in relativistic shocks and the origin of afterglow emission is presented in the following sections.

Acceleration mechanism

When the outflowing material interacts with the CBM, relativistic shocks take place. Free electrons get accelerated to relativistic energies at these shocks, thus producing the synchrotron emission which gives rise to the afterglow. The so-called diffusive shock acceleration (DSA) model (Blandford &

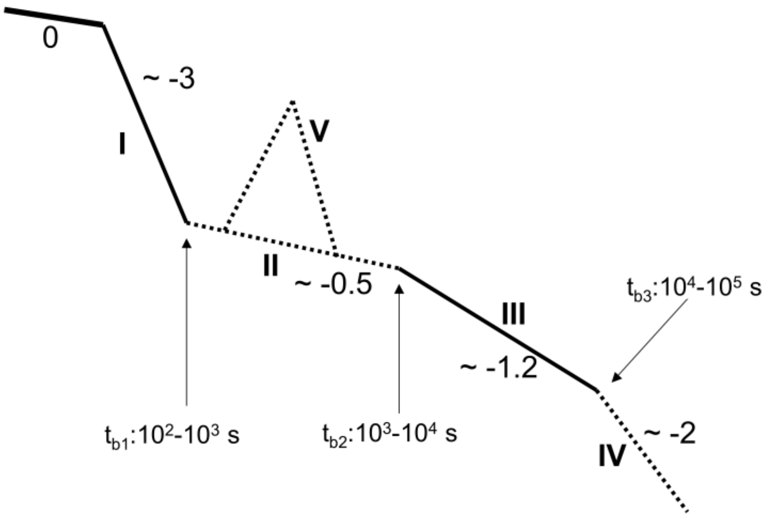

Figure 1.4: The five component X-ray afterglow light-curve as proposed in B. Zhang, Fan, et al. (2006). Segment 0 represents the tail of the prompt emission. Segments I (steep decay) and III (normal decay) are the most common, and so they are represented by solid lines, while segments II (shallow decay), IV (jet break) and V (flares) are present only in a fraction of bursts, and so they are marked by dashed lines. Expected values for the time decay indices are reported too.

Ostriker, 1978) provides the standard picture for describing this complicated process: it assumes that particles are confined in a narrow region straddling the shock because of magnetic irregularities (Alfvén waves) and then accelerated, as a result of repeated crossings of the shock surface. This represents a particular realisation of a generic type-II Fermi process: at each shock crossing cycle (i.e., from upstream to downstream and back, or vice-versa), an electron gains some energy ΔE and has a probability $\mathcal{P}_{esc}$ of escaping (leaking off) the shock, which increases with the particle's energy. As a result of the interplay between these two factors, electrons will acquire a power-law distribution in energy, in the form:

$$N(E)dE \propto E^{-p}dE. \tag{1.5}$$

The DSA model cannot formally be applied in GRBs because the diffusion approximation for spatial transport does not apply strictly for relativistic shocks, i.e. when the shock Lorentz factor $\Gamma_s \gg 1$. However, Achterberg et al. (2001) first demonstrated that, under particular conditions (i.e., strong magnetic fluctuations in the upstream and downstream media), it is explained that the energy spectrum of particles accelerated in ultra-relativistic shock would still follow a power-law as in Eq. 1.5, where the power-law slope p is:

$$p = 1 + \frac{\ln(1/\mathcal{P}_{ret})}{\ln\langle E_f/E_i\rangle}, \tag{1.6}$$

with $\mathcal{P}_{ret} = 1 - \mathcal{P}_{esc}$ the average probability per cycle that a particle crosses again the shock returning upstream and $E_f/E_i = 1 + \Delta E/E_i$ is the final vs initial energy ration per cycle. Angular brackets indicate that values represent an average over the population. Through numerical simulations and analytic calculations, several studies were able to compute a "universal" value for the power-law slope $p \sim 2.2 - 2.3$, although the value of this spectral index is still an open problem, given that the microphysical mechanisms involved in the particle acceleration via relativistic shocks are still far from being completely understood. In the following we will use the results obtained by Achterberg et al. (2001) as a standard reference.

Standard spectra and light-curves of GRB afterglows

In order to calculate the afterglow spectra and light-curve evolution from synchrotron emission of shock-accelerated electrons, we present here the results obtained by Sari, Piran, and Narayan (1998). We start by rewriting the energy distribution of Eq. 1.5 in terms of the Lorentz factor of the electrons γ_e:

$$N(\gamma_e)\, d\gamma_e \propto \gamma_e^{-p}\, d\gamma_e, \tag{1.7}$$

where $\gamma_e \geq \gamma_m$ and γ_m is the Lorentz factor corresponding to the minimum electron energy: notice that we adopted lower-case γ for the particles Lorentz factor to differentiate it from upper-case Γ_s, the Lorentz factor of the shocked material.

The relativistic forward shock propagates into a cold surrounding medium with constant number density n. At the beginning, the shock undergoes a free expansion into the ambient medium sweeping a volume of radius $r = ct$. At some time t_d the shock has swept up enough mass to equal the initial energy of the shock ($M_{swept} = \Gamma_s^2\, M_{0,\mathrm{ej}}$) and the expansion starts decelerating, triggering the conversion of the shock kinetic energy into internal energy, and then to radiation, giving rise to the afterglow. The corresponding *deceleration radius* is defined as $r_d = ct_d$. Due to relativistic effects, and to the factor 4 increase of density downstream of the shock, we can define the total shock energy as $e = 4\,\Gamma_s^2\, n\, m_p\, c^2$. By making the simple assumption that a constant fraction ϵ_e of the shock energy is transferred to the accelerated electrons, then γ_m is directly related to ϵ_e through:

$$\gamma_m = \epsilon_e \left(\frac{p-2}{p-1}\right) \frac{m_p}{m_e}\, \Gamma_s \simeq 610\, \epsilon_e\, \Gamma_s, \tag{1.8}$$

where the second result is taken considering the standard choice $p = 2.5$ (Sari, Narayan, et al., 1996), which is close to the theoretically expected value of $2.2 - 2.3$ (see above) and, when integrating in time the synchrotron emission, returns exactly the high energy index $\beta = 2.25$ of the radiative power-law spectrum derived by Band et al. (1993). An additional assumption is that another constant fraction ϵ_B of the shock energy goes in the energy of the magnetic field in the downstream medium,

$$\frac{B^2}{8\pi} = \epsilon_B e = \epsilon_B (4\,\Gamma_s^2\, n\, m_p\, c^2), \tag{1.9}$$

from which it is possible to derive the B-field strength as a function of ϵ_B, n and Γ_s. With these assumptions, it is possible to calculate the synchrotron luminosity and spectrum emitted by a population of electrons.

We recall that a single relativistic electron in the presence of a magnetic field would emit with a radiation power that in the observer frame will take the form:

$$P(\gamma_e) = \frac{4}{3}\sigma_T c \gamma_e^2 \frac{B^2}{8\pi}\,\Gamma_s^2, \tag{1.10}$$

where σ_T is the Thomson cross section while the factor Γ_s^2 is introduced to convert from the comoving to the observer frame. Moreover, synchrotron characteristic frequency for the single electron in the observer frame is given by:

$$\nu(\gamma_e) = \gamma_e^2 \frac{q_e B}{2\pi m_e c}\Gamma_s. \tag{1.11}$$

The behaviour of the spectral power P_ν (power per unit frequency, erg s^{-1} Hz^{-1}) is the standard synchrotron one, showing a maximum at $\nu(\gamma_e)$, a power-law behaviour $\propto \nu^{1/3}$ at low frequencies and an exponential cut-off at high frequencies. It is then important to define γ_c as the critical energy above which radiation losses of the electron become important. It can be defined with the condition $\gamma_c m_e c^2 \Gamma_s^2 = P(\gamma_c) t$, where t is the time in the observer frame. For energies of the electron $\gamma_e > \gamma_c$, cooling by synchrotron are not negligible and the spectral power is modified.

To obtain the total spectrum from the whole electron population, distributed following a power-law, we need to integrate over all the values of γ_e. It is important to distinguish two different cases:

- *fast cooling* ($\gamma_m > \gamma_c$): the minimum energy of the electron population is larger than the critical energy, implying that all the electrons are allowed to cool down to γ_c;
- *slow cooling* ($\gamma_m < \gamma_c$): the minimum energy of the electron population is lower than the critical energy, implying that only the electrons above

the critical value will cool down and radiate energy within a timescale comparable with the dynamical timescale, while the majority will take much longer time.

Fast cooling is expected to happen in the first phase of the GRBs, because in this phase relativistic shocks should emit their energy efficiently; slow cooling instead is expected to take place during the early afterglow/ late-prompt emission, in the initial stages of the forward shock. This is why in the following we will only focus on the slow cooling case.

The flux density in the observer frame in the slow cooling case will be given by:

$$F_\nu = \begin{cases} (\nu/\nu_m)^{1/3} F_{\nu,\mathrm{obs}}, & \nu < \nu_m, \\ (\nu/\nu_m)^{-(p-1)/2} F_{\nu,\mathrm{obs}}, & \nu_m < \nu < \nu_c, \\ (\nu_c/\nu_m)^{-(p-1)/2} (\nu/\nu_c)^{-p/2} F_{\nu,\mathrm{obs}}, & \nu > \nu_c. \end{cases} \tag{1.12}$$

where $\nu_m \equiv \nu(\gamma_m)$, $\nu_c \equiv \nu(\gamma_c)$ and $F_{\nu,\mathrm{obs}}$ is the value of the flux density at the peak. In addition, at lower frequencies ($\nu < \nu_a$, with ν_a self absorption frequency), synchrotron self-absorption causes a steep cut-off, showing a behaviour either as ν^2 or $\nu^{5/2}$ (Katz, 1994), but this does not affect X-ray radiation. The corresponding spectrum is portrayed in Fig. 1.5.

The spectrum derived above is an instantaneous spectrum, it does not include any time evolution. To build a light-curve, instead, it is important to understand how the different quantities evolve in time. The following discussion is done considering a simplified case: we assume a spherical relativistic shell with radius $R(t)$ which expands into a surrounding medium with constant number density n, so that the total number of swept up electrons is $N_e = 4/3\,\pi R(t)^3 n$. Moreover, we distinguish two limit cases:

- *fully radiative*: the whole energy created in the shock is radiated away. This happens if both these two condition are fulfilled:
  1) the fraction of shock energy going into electrons is large, $\epsilon_e \rightarrow 1$;
  2) we are in fast cooling regime, $\gamma_m > \gamma_c$.
  If one of these two condition is not matched, we are in the fully adiabatic case;

- *fully adiabatic*: the energy of the spherical shock remains constant in time.

Since in this work we mainly focus in the slow cooling regime, that means $\gamma_m < \gamma_c$, we limit the following discussion to the adiabatic case. It can be shown that it is possible to write the time dependencies of both $R(t)$ and

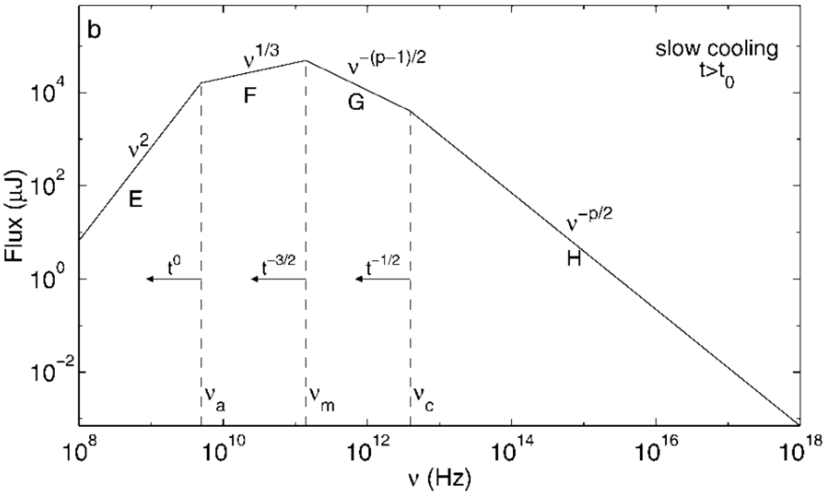

Figure 1.5: Synchrotron spectrum produced by a relativistic shock with a power-law distribution of electrons in the slow cooling regime case, that is when the minimum energy of the electron population is lower than the synchrotron critical energy, $\gamma_m < \gamma_c$, and only electrons at higher energies are able to cool efficiently: this is expected to happen at late times. The spectrum consists of 4 segments: F, G and H correspond to the 3 behaviours described in Eq. 1.12, while segment E is linked to synchrotron self-absorption. Arrows show the temporal behaviour of each characteristic frequency (Sari, Piran, and Narayan, 1998).

$\Gamma_s(t)$, that can be then used to derive the time evolution of the following quantities:

$$\begin{aligned} \nu_c &\propto t^{-1/2} \\ \nu_m &\propto t^{-3/2} \\ F_{\nu,\mathrm{obs}} &= \mathrm{const.} \end{aligned} \tag{1.13}$$

It is clear that ν_m decreases in time faster than ν_c (this can be proven also in the radiative case): so, if we start with $\gamma_m > \gamma_c$ (fast cooling), at a certain point we will reach an instant t_0 such that $\nu_0 \equiv \nu_c(t_0) = \nu_m(t_0)$, that will define the transition from the fast cooling to the slow cooling regime (that is when $t > t_0$ and $\nu_m < \nu_c < \nu_0$).

If we now consider a fixed observing frequency ν, since ν_c and ν_m decrease with time, there will be two instants, called t_c and t_m respectively, in which the characteristic frequencies ν_c and ν_m coincide with the observing frequency. In the case in which the observing frequency is smaller than the transition frequency, $\nu < \nu_0$ (low frequency case), the three critical times t_0, t_c and t_m, computed according to Eq. 1.13, will be ordered as $t_0 < t_m < t_c$. For each time range, the corresponding segment of the slow cooling spectrum in Fig. 1.5 is taken into account in order to extract the temporal evolution of the emission in that specific time range: this is how the afterglow light-curve in Fig. 1.6 is built.

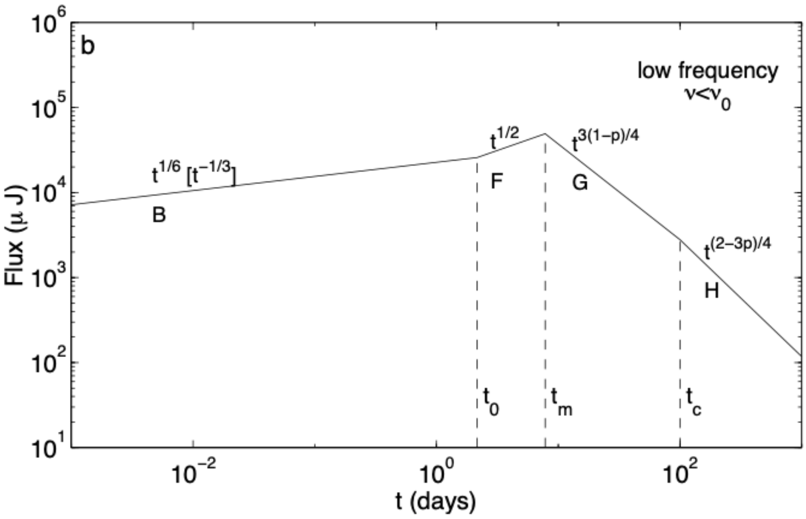

Figure 1.6: Light-curve showing how the observed flux originated by the synchrotron emission of a relativistic shock evolves in time, in the low frequency case ($\nu < \nu_0$). It is composed by four segments, labeled with letters corresponding to the associated spectral segment in Fig. 1.5. We focus only on the adiabatic case so we don't consider what happens before t_0 (segment B,Sari, Piran, and Narayan, 1998).

The time interval in which we are most interested is when $t > t_0$, that is after the transition to slow cooling regime takes place. Given that X-ray afterglow emission is always observed to decrease in time (apart from the case of GRB 170817, for the reasons explained in Section 1.4), it is clear that the two leading time dependencies we expect for the flux density $F_\nu \sim t^{-\alpha}$ in case of afterglows are characterized either by $\alpha = 3(p-1)/4$ or by $\alpha = (3p-2)/4$. These two values give the time behaviour we expect to observe in afterglow light-curves if synchrotron emission is the only mechanism at work. The majority of afterglows, at late times (> 12 h, typical of *BeppoSAX*) satisfies these predictions; however this is not true during the early afterglow evolution: the divergences from this model are carefully described in Section 1.3.4.

1.3.3 Jet evolution

The previous calculations were based on the assumption of spherical symmetry, but the temporal dependence of the break frequency and of the normalization are strongly dependent on the hydrodynamical evolution of the blast wave. This means that the light-curve produced by a spherical shock may

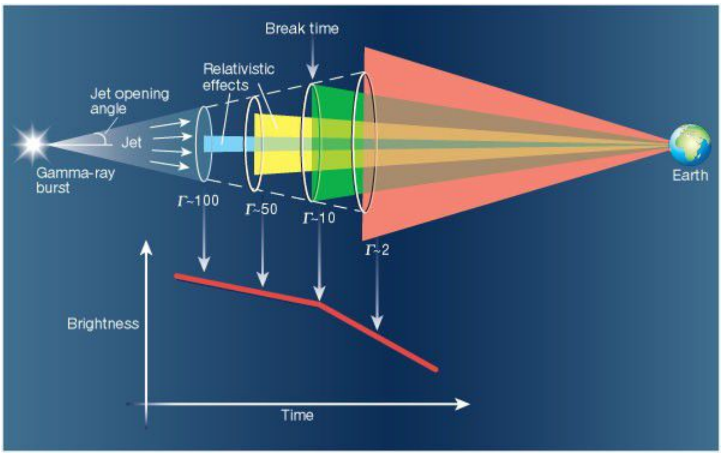

Figure 1.7: The burst launches a jet of relativistic material with a certain opening angle θ_j. The material moves almost at the speed of light, its Lorentz factor Γ_s being ~ 200: because of special relativity effects, observer can initially see only a portion of the jet (in blue) and this makes it impossible to distinguish if emission comes either from a jet or from a sphere. As the jet encounters the surrounding material, it slows down and a larger fraction of the jet becomes visible (in yellow) up to when $\Gamma_s \sim \theta_j^{-1}$ and the whole jet becomes visible (in green, in this case corresponds to $\Gamma_s \sim 10$. From this moment on, no new matter will become visible and the brightness of the afterglow will start to decline more rapidly: this is the so called brake time $t_{\rm jet}$. At later times, jet is slow enough ($\Gamma_s \sim 2$, in orange) to allow to observe matter from a much larger area (S. Woosley, 2001).

differ significantly from that produced by other structures, like an expanding jet-like shell. Several works (Sari, Piran, and Halpern, 1999; Rhoads, 1999; Frail et al., 2001 suggested that a jet geometry provides a more accurate description of the dynamics of the blast wave with respect to a spherical one.

Typically, in the literature, two main types of jets are defined:

- uniform jets: in this case the jet is modeled as a cone with a sharp edge and a uniform distribution of energies and Lorentz factor Γ_s;
- structured jets: this model assumes an angular distribution of Lorentz factor Γ_s and energies.

Even though the recent observations of GRB 170817 and its atypical light-curve evolution have given strong support to the structured jet hypothesis (see Sec. 1.4), in this work we report just some of the results related to the simplest case. The relativistic jet can be described by its half opening angle θ_j and by its Lorentz factor $\Gamma_s(\theta)$ too. Due to relativistic beaming effects, only the emission coming from within a solid angle $\sim 1/\Gamma_s$ cone is observable. In Sari, Piran, and Halpern (1999) it was shown that, in the early phase and as long as the condition $\Gamma_s > \theta_j^{-1}$ is satisfied, the jet material does not have enough time to expand laterally in its own rest frame and hence the jet hydrodynamics will not be different from the spherical case. Things change substantially when, on account of the jet deceleration, $\Gamma_s \simeq \theta_j^{-1}$ is reached: at this stage the side expansion will not be negligible anymore and two-dimensional simulations are needed to properly model the evolution of the jet in this phase.

The existence of a jet-like structure is suggested by the occurrence in some bursts of a steepening at very late times (typically beyond 10^5 s or even later) of the decay index of the afterglow light-curve: this is called "jet-break" (see also segment IV in Fig. 1.4) and it can generally be originated by two different effects: the side way expansion and the edge effect. The former arises when $\Gamma_s \sim \theta_j^{-1}$ and the jet starts to decelerate exponentially (Rhoads, 1999); the latter is instead generated by the lack of emission due to the fact that, when $\Gamma_s < \theta_j$, it is not possible to observe flux coming from angles larger than θ_j with respect to an observer in the line-of-sight of the jet (Granot, 2006). Both these effects are due only to relativistic and hydrodynamic mechanisms, and so they will affect equally all the frequencies, resulting in an achromatic steepening (break) in the light-curve (see Fig. 1.7). Starting from the observed jet break time $t_{\rm jet}$, it is possible to compute the half opening angle θ_j in the case of an Interstellar Medium (ISM)-like CBM (which implies a constant density and is opposed to a stellar wind medium, Frail et al., 2001):

$$\theta_{j,{\rm ISM}} = \left(\frac{t_{\rm jet}}{1\,{\rm d}}\right)^{3/8} \left(\frac{1+z}{2}\right)^{-3/8} \left(\frac{E_{\gamma,{\rm iso}}}{10^{52}\,{\rm erg}}\right)^{-1/8} \left(\frac{\eta_\gamma}{0.2}\right)^{1/8} \left(\frac{n}{0.1\,{\rm cm}^{-3}}\right)^{1/8} \tag{1.14}$$

where z is the GRB redshift, n is the mean density of the CBM, $E_{\gamma,{\rm iso}}$ is the isotropic-equivalent prompt energy release and η_γ is the efficiency of the fireball in converting the energy of ejecta into gamma-rays. In the case of long GRBs, opening angles are found in the range between 3 and 10 degrees (Harrison et al., 1999), while for short GRBs it is more challenging to measure them, particularly because the afterglows are fainter (Kann, 2013).

The presence of a jet would also "relax" some of the energetic requirements needed to explain bursts: indeed, the typically observed isotropic-equivalent luminosity $L_{\gamma,iso} \sim 10^{52}$ erg s^{-1} is several orders of magnitude higher than the Eddington luminosity of a $\sim 10\,{\rm M}_\odot$ black hole, but these extremely high values become much easier to explain if collimation processes take place. For example, a beaming of $\theta_j \sim 0.1$ would diminish the energetic requirement by a factor of 200 (Sari, Piran, and Halpern, 1999).

1.3.4 Plateau incidence

From the day it was launched, the *Swift* satellite revolutionized our understanding of GRB afterglows thanks to its unique rapid slewing capability: this allowed the X-ray telescope on board (XRT, Gehrels, Chincarini, et al., 2004) to identify the never observed early afterglow evolution (from $\sim 10^2$ to $\sim 10^4$ seconds after the burst trigger) bringing to light features that could not be seen with previous late time observation. This soon allowed to distinguish different phases of the afterglow light-curves at early times, each of them characterized by a particular time dependence. In their works, B. Zhang, Fan, et al. (2006) and Nousek et al. (2006) proposed a "canonical behaviour" for the X-ray afterglow light-curves, according to which the flux density F_ν evolves like a multi-segment power-law going as:

$$F_\nu(t,\nu) \propto t^{-\alpha}\nu^{-\beta} \tag{1.15}$$

where α is the temporal decay index and $\beta = \Gamma - 1$ is the spectral index, whereas Γ is the photon index. In a large fraction of the analyzed cases, three main phases were identified (Fig. 1.8): an initial steep decay slope ($3 \lesssim \alpha_1 \lesssim 5$), followed by a so called shallow decay ($0.5 \lesssim \alpha_2 \lesssim 1$) that eventually transitions to a later decay phase ($1 \lesssim \alpha_3 \lesssim 1.5$), steeper than the second phase but shallower than the first.

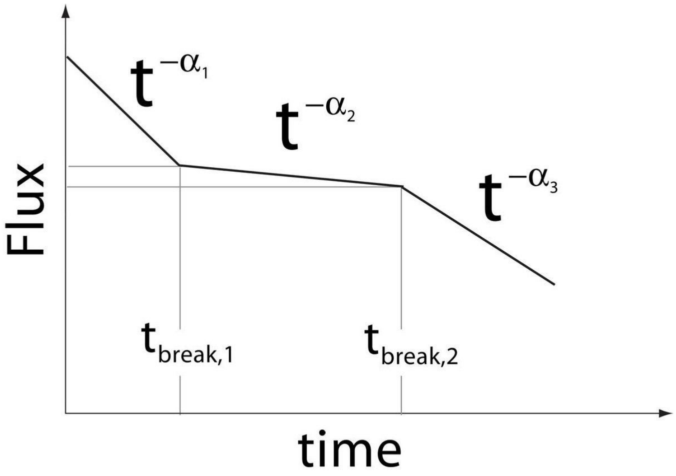

Figure 1.8: Schematic representation of an early X-ray afterglow light-curve showing a "canonical behaviour" as proposed in Nousek et al. (2006) after having analyzed *Swift* GRBs. The flux evolves with time and frequency as $F_\nu(t,\nu) \propto t^{-\alpha}\nu^{-\beta}$ and the light-curve is composed by three power-law segments, separated by two break times $t_{break,1}$ and $t_{break,2}$: (1) an initial steep decay ($3 \lesssim \alpha_1 \lesssim 5$), (2) a very shallow decay phase ($0.5 \lesssim \alpha_2 \lesssim 1$) and (3) a later decay, steeper than the second one ($1 \lesssim \alpha_3 \lesssim 1.5$).

In particular, analyzing the huge amount of GRBs detected by *Swift* in the years following these preliminary works, it has been shown that a significant fraction of GRBs show evidence of the shallower decay phase, that started to be defined as "*plateau*". In the majority of LGRBs, a plateau is observed; when considering short GRBs, instead, their brief duration and the fact that they are much fainter than long GRBs (Kann, 2013) makes it harder to understand if a plateau is present or not, but in general the fraction appears to be much lower than in the case of long ones. Anyway, giving a physical interpretation to this plateau phase resulted in being a very complex challenge. This was not true for the initial steep decay phase, which has been interpreted as the low energy tail of the prompt emission, where the first break time $t_{break,1}$ marks the transition happening when the afterglow emission, which is characterized by a slower decay with respect to the rapid decaying prompt emission, starts to be dominant (see B.-B. Zhang et al. (2007) for a detailed discussion). For what concerns the plateau phase instead, some aspects seemed to be in contrast with the predictions made by the standard afterglow models based on synchrotron emission proposed by Sari, Piran, and Narayan (1998). The main inconsistencies were the following:

- A) The observed values α_2, the time decay index of the shallow phase, were often too small to be adequately explained by the adiabatic expansion of a forward shock with constant energy like in the model of Sari, Piran, and Narayan (1998): indeed, as previously shown in Section 1.3.2, the shallowest decay index we would expect in this case would be $\alpha_2 = 3(p-1)/4$ (or $\alpha_2 = (3p-2)/4$ in the radiative case, which is even steeper), recalling that p is the slope of the power-law describing the accelerated electrons distribution. Remembering the assumption $p > 2$, it is easy to calculate that in the adiabatic case, we would obtain values of the decay index $\alpha_2 > 0.75$. In many cases, instead, the observed values of α_2 are much flatter than 0.75, with $\alpha_2 \in [0, \sim 0.7]$ (Ronchini et al., 2023) .

- B) The spectral index, in the standard afterglow model, is expected to change at t_{break_2}, when we transition from shallow to normal decay phase, because breaks are interpreted as characteristic frequencies of the synchrotron spectrum crossing the observing frequency band, causing a change of decay rate in the light-curve. Instead, when observing plateaus, the X-ray spectral slope remains constant before and after the break $t_{break,2}$.

One of the possible interpretations that can be given to the shallow decay phase and does not involve spectral variation, is the presence of a gradual and long-lasting energy injection into the external shock that originates the afterglow, attributable to a long-lived central engine. Several hypothesis were proposed to explain the nature of a central engine able to provide a continuous energy injection. One of them is the formation of a black hole in the center, surrounded by a torus made of ejected material: matter falling back into the black hole would provide the extra energy. These models were deeply explored in several works (Narayan et al., 1992; S. E. Woosley, 1993) but are not taken into account for the scope of this Thesis work. An alternative central engine is instead a rapidly spinning neutron star (Usov, 1992), characterized by an extremely intense magnetic field ($B > 10^{14} - 10^{15}$ G, Usov, 1992; Duncan and C. Thompson, 1992; Blackman and I. Yi, 1998; Dall'Osso et al., 2011). The energy release would be powered by the magnetic-dipole spin down through which the newly formed neutron star would lose its huge initial spin energy (see Section 1.3.5 for a deeper description).

A totally different interpretation, instead, tries to explain the plateau phase relying on geometric arguments. This is the so called high latitude emission (HLE) from a structured jet model. even though this model was already theorized in the past, for years energy and velocity distribution in GRB jets were approximated as constant within the solid angle of the jet. This changed when the off-axis observation of the emission of GRB 170817 (see Section 1.4 for more details), highlighted the complex structure of GRB jets, showing a decreasing distribution of energies and velocities going towards the edges. GRB jets' structured nature can be used to interpret the extra-emission we observe a late times (Oganesyan et al., 2020; Beniamini, Gill, et al., 2022).

Since the discovery of the shallow phase in X-ray light-curves of GRBs, several works have been carried out with the purpose of giving an interpretation to this distinctive time behaviour, both in the case of short and long GRBs. For what concerns the short cases, the ones we focus on in this Thesis work, multiple efforts were done in the process of finding a physical explanation to plateaus. To cite one of the most comprehensive works, Rowlinson et al. (2013) took a sample including all the short GRBs observed by the *Swift* satellite until 2012 May (for a total of 43 cases) and proceeded in the search of plateau features in their afterglow light-curves, finding that about half of them showed evidence of plateau. Despite showing several analogies with the analysis carried out in this Thesis work, there are some fundamental discrepancies with respect to the procedure described in Chapter 3:

- the sample they analysed is for obvious reasons much smaller than the one used for this Thesis, making it less representative of the nature of the phenomenon;

– they looked for plateaus considering together both BAT and XRT data, but this can be problematic because, as explained in Chapter 2, these two instruments onboard *Swift* work in two different energy band and extrapolating data in a band different than the native one can introduce errors. In addition, considering also BAT data means to include in the analysis also the prompt emission, while plateau are expected to happen in the afterglow phase. Moreover, they did not exclude extended emission phase whilst fitting the light-curves.

In this work instead we perform the analysis on a larger sample of SGRBs, increasing the statistics, we fit only the XRT data, which are the ones describing the afterglow, using BAT data only as a reference, and we treat separately the cases that we are able to classify as pure extended emission since they do not provide any information about the afterglow. The details regarding this procedure are outlined in Chapter 3.

1.3.5 Magnetar model

As mentioned in Section 1.3.4, one of the possible explanation of the extra energy required to give birth to the X-ray "plateau" in GRB afterglows is a long-lasting energy injection produced by the central engine. Among several hypotheses on the nature of the central engine, the formation of a rapidly rotating neutron star with strong surface magnetic field, called millisecond magnetar is one of the most promising.

Magnetars as central engines of GRBs were first proposed by Usov (1992) and further elaborated by Dai and Lu (1998), B. Zhang and Mészáros (2001), Bucciantini et al. (2006), and B. D. Metzger, Giannios, et al. (2011). Dall'Osso et al. (2011) developed the first model self-consistent calculation of the afterglow light-curve with energy injection from a millisecond spinning magnetar, and subsequent applications of the magnetar model to real data gave encouraging results (Rowlinson et al., 2013; Stratta et al., 2018). In the following, we summarize the afterglow model as presented in Dall'Osso et al. (2011) and Stratta et al. (2018).

If the GRB central engine is a magnetar, the afterglow emission will be modified because the spin-down of the magnetar will inject extra energy in the environment and in particular in the external shock. Due to magnetic dipole radiation, the NS will lose its rotational energy, presumably in the form of a strongly magnetised particle wind, with a luminosity that is given, in the ideal magnetohydrodynamics (MHD) approximation, by (Spitkovsky, 2006):

$$L_{\rm sd} = \frac{\mu^2}{c^3}\,\Omega^4(1+\sin^2\theta), \tag{1.16}$$

where $\mu = BR^3/2$ is the magnetic dipole moment, B the (dipole) magnetic field strength at the NS pole, R the NS radius, $\Omega = 2\pi\nu$ is the NS spin rate and θ the angle between the rotation and magnetic axes. Because the spin-down luminosity can be expressed as $L_{\rm sd} = I\Omega\dot{\Omega}$, where I is the moment of inertia of the NS, an usual way to describe a generic NS spin-down is through the relation:

$$\dot{\Omega} \propto \Omega^n, \tag{1.17}$$

where n is called the "braking index": $n = 3$ for the ideal MHD case above, while non-ideal effects generally imply $n \leqslant 3$[6]. The general problem of NS spin-down with non-ideal MHD effects is not well understood yet, however Contopoulos and Spitkovsky (2006) have proposed a particular parameterized relation:

$$L_{\rm sd}^{\rm N-I} = L_{\rm sd}\left(\frac{\Omega}{\Omega_i}\right)^{-2\alpha}, \tag{1.18}$$

where "$\rm N-I$" labels the non ideal case, $0 < \alpha < 1$ is directly linked to the braking index $n = 3 - 2\alpha$ and the subscript i indicates the initial time.

Because of the relativistic motion of the emitting region (internal shocks for the prompt emission, external shock in the case of the afterglow), in calculating the temporal evolution of GRB light-curves it is crucial to define the relation between the time t, measured in the central engine rest frame (the NS), and the time T measured by the observer. The infinitesimal time variations dt and dT can be connected through:

$$dT = (1-\beta(t))dt \simeq \frac{dt}{2\Gamma_s^2(t)}, \tag{1.19}$$

where $\Gamma_s(t) = \sqrt{1-\beta^2(t)}$ is the Lorentz factor of the blast wave as a function of time.

In order to derive the expected temporal evolution for the light-curve, we write the energy balance of the relativistic shock wave including radiative losses and the rate of energy injection by the spinning-down magnetar. In the NS rest frame it can be written as:

$$\frac{dE}{dt} = (1-\beta(t))L_{\rm sd}\left[t - \frac{r(t)}{c}\right] - k\frac{E}{t}. \tag{1.20}$$

---

[6] Different spin-down mechanisms may even correspond to larger braking indexes. For example, gravitational-wave driven spin-down corresponds to $n = 5$.

Here, the first term represents the energy injected in the shock at time t and also accounts for the time that this energy, in the form of relativistic wind with velocity $\beta(t)$, took to reach the shock at $r(t)$, while the second term represents the radiation losses, with $k = 4\epsilon_e$ and ϵ_e the fraction of the total energy transferred to electrons. Using Eq. 1.19, we can rewrite Eq. 1.20 relative to the observer's time T:

$$\frac{dE}{dT} = L_{\rm sd}(T) - k\frac{E}{T}\left(\frac{d\ln t}{d\ln T}\right). \tag{1.21}$$

The first term in Eq. 1.21 can be directly obtained from Eq. 1.18:

$$L_{\rm sd}(T) = \frac{L_{{\rm sd},i}}{\left[1+(1-\alpha)\,\dfrac{T}{\tau_i}\right]^{\frac{2-\alpha}{1-\alpha}}} = \frac{E_{{\rm spin},i}}{\tau_i\left[1+(1-\alpha)\,\dfrac{T}{\tau_i}\right]^{\frac{2-\alpha}{1-\alpha}}}\,, \tag{1.22}$$

where $E_{\rm spin} = (1/2)I\Omega^2$ is the NS spin energy, $\tau = \Omega/2\dot{\Omega}$ is the spin-down timescale and the subscript i refers to the initial time. The second term in Eq. 1.21 depends on $(d\ln t/d\ln T)$, which encloses the hydrodynamical evolution of the shock. However, one can show that $(4+k)^{-1} < (d\ln t/d\ln T) < 1/2$ thus, in a first-order approximation, we can consider the quantity $k' = k(d\ln t/d\ln T) \simeq$ const: this free parameter contains all our ignorance about the density profile of the ambient medium and about the microphysics.

With all the assumptions described above, Eq 1.21 has the solution:

$$E(T) = \frac{L_i}{T^{k'}}\int_{T_0}^{T}\frac{T^{k'}}{(1+aT^2)}\,dT + E_0\left(\frac{T_0}{T}\right)^{k'}\,, \tag{1.23}$$

where T_0 is any time chosen as initial condition, $a = 2K\Omega_i^2$ and $K = 4\mu^2/(6Ic^3)$. The integral in Eq. 1.23 can be rewritten in terms of the hypergeometric function ${}_2F_1(a,b;c;z)$, where $z = (1+aT)^{-1}$. In this way, we obtain the expression for $E(T)$ and we can use it to calculate the total (bolometric) luminosity of the shock-wave, that corresponds to the radiative term in Eq. 1.21, i.e. $L(T) = k'E(T)/T$.

It is well known that core-collapse supernovae (CCSNe) mostly give birth to NS and presumably a fraction $\lesssim 10\%$ of these NS are magnetars (Gaensler et al., 2005; Beniamini, Hotokezaka, et al., 2019). Indeed, from observation it is possible to estimate that in our Galaxy the observed rate of CCSNe is approximately $\dot{N}_{\rm CC} \sim (10^2~{\rm yr})^{-1}$, while the minimum magnetar birth rate is expected to be $\dot{N}_{\rm mag} \sim (10^3~{\rm yr})^{-1} \approx 0.1\,\dot{N}_{\rm CC}$.

Moreover, as previously said in Section 1.3.3, GRB emission is expected to be beamed: this means we only observe GRBs when the angle between their beam and our line of sight is relatively small, namely $\lesssim 10$ degrees: computing the probability to observe inside this beam compared to observing isotropic emission, one finds that we are able to observe only $\sim 1\%$ of the GRBs happening in the Universe. Taking this into account, the fact that the rate of observed GRBs for a low-redshift Milky Way-like galaxy is expected to be $\dot{N}_{\rm GRB,obs} \sim (10^6\ {\rm yr})^{-1}$ (B. Zhang & Mészáros, 2001) translates in a real GRB rate of $\dot{N}_{\rm GRB,real} \sim (10^4\ {\rm yr})^{-1}$. Comparing this rate with the observed rate of CCSNe, one can roughly derive $\dot{N}_{\rm GRB,real} \approx 0.01\, \dot{N}_{\rm CC}$.

The population of magnetar associated to CCSNe appears to be compatible with the rate of LGRBs, if anything slightly larger. This links with the hypothesis that sees magnetars as potential central engines of LGRBs, but it is important to pay attention: this does not lead to any strong association between magnetars and LGRBs, but just entails that the magnetar hypothesis cannot be excluded.

On the other hand, linking the magnetar hypothesis to SGRBs is more complicated: in the case of BNS mergers, the fate of the merger remnant is indeed strongly dependent on the NS equation of state (EOS), which is still very far from being completely understood (Lattimer, 2021, see Chapter 5) While for cold and non-rotating NS the Tolman–Oppenheimer–Volkoff mass limit (or $M_{\rm TOV}$) stands, the maximum stable mass can change if millisecond rotation is present. Assuming an EOS, depending on its mass the remnant originated by the merger can be either stable or unstable: in the latter case, it will directly collapse into a BH (Margalit & B. D. Metzger, 2017). This suggests that only a small fraction of BNS mergers gives birth to a stable NS able to emit radiation for relatively long times. Nevertheless, the standard BH-disk accretion scenario was proven to struggle to explain the long nature of X-ray afterglows in the case of SGRBs, since the relatively small amount of ejected material produced by the merger results in a short accretion timescale of the debris disk onto the BH ($\sim$ seconds, Ciolfi et al., 2017). Instead, the formation of a stable, long-lived magnetar can naturally account for high energy emission on longer timescales.

For these reasons, the magnetar model outlined above is the model used in Chapter 4 to fit the light-curves of the SGRBs which resulted in showing clear evidence of plateau and to derive physical parameters of the magnetar central engine.

1.4 The case of GRB 170817

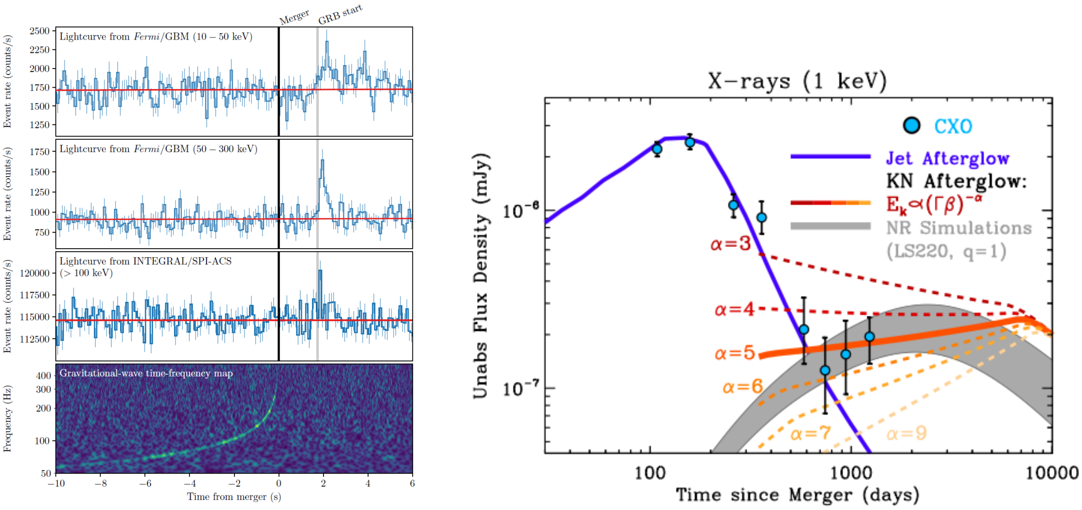

(a) **(b)**

Figure 1.9: **(a)** Joint multi.messenger detection of GRB 170817 and GW 170817. Top two panels are Fermi/GBM light-curves, respectively in the 10-50 keV and in the 50-300 keV energy range, while third panel is INTEGRAL/SPI-ACS light-curve in the 100 keV - 80 Mev range. Bottom panel is the time-frequency map of GW 170817 obtained by LIGO (Abbott et al., 2017). **(b)** Results of the multi-wavelength follow-up campaign of the EM counterpart of GW 170817, up to 1273 days after the merger. The X-ray evolution . The peculiar X-ray afterglow evolution (in blue) detected by *Chandra* X-ray observatory (CXO, azure circles) shows a peculiar behaviour (gradually increasing during the first ∼ 150 days, reaching a peak emission and decreasing at later times): this is well explained by the off-axis jet afterglow model (blue line). At very late times (> 900 days), where the X-ray emission excess can be interpreted as the emerging synchrotron radiation coming from the kilonova afterglow (grey region is the kilonova afterglow calculated through numerical relativity simulations, while dashed lines represent semi-analytical model, Hajela et al., 2022).

On August 17, 2017 the gravitational wave detectors *Advanced LIGO* and *Virgo* detected the gravitational wave event GW 170817. Only 1.74 seconds later, independent observations by the *Fermi* Gamma-ray Burst Monitor (GBM) and by the SPectrometer on board *INTEGRAL* Anti-Coincidence Shield (SPI-ACS) detected the short GRB 170817 event ($T_{90} = (2.0 \pm 0.5)$ s starting at $T_0^{\text{GBM}} - 0.192$ s, where T_0^{GBM} is defined as the time of GBM trigger, Goldstein, Veres, et al., 2017). These two detections led to the confirmation that binary neutron stars mergers are progenitors of short GRBs: the chance probability of two almost simultaneous and spatially-coincident observations was indeed estimated to be $\sim 10^{-8}$, implying that the two events should be associated (see Fig. 1.9a, Abbott et al., 2017).

GRB 170817 is an extremely peculiar case in the sample of known GRBs. After the first short-lived emission detected in the gamma-ray band, X-ray telescopes were pointed in the same sky region looking for the afterglow emission, but nothing was detected. Only 11 hours after the trigger, follow-up optical/infrared observations of the sky location indicated by GW detectors revealed the optical emission in the galaxy NGC 4993, 130 millions light years from Earth: the thermal nature of this emission led to classifying this transient as the macronova/kilonova event AT2017gfo (Coulter et al., 2017). A kilonova (KN) is a transient event associated with compact binary mergers: it consists of a bright electromagnetic thermal emission originated by the radioactive decay of the heavy elements which are formed via rapid neutron-capture process es (r-processes) within the high-density neutron-rich material that was ejected prior to, during and immediately after the merger (Rosswog, 2015). The KN detection, whose spectral color was observed to turn from blue to red as the source expanded and cooled, allowed a much better localization of the source. Several other instruments then started observing that region and on August 26, nine days after the GW 170817/GRB 170817 detection, NASA's *Chandra* X-ray Observatory (CXO) first detected the X-ray emission, i.e. the GRB afterglow (unrelated to the KN), from the same position of the optical-IR source. But this emission showed an unexpected time evolution, as the X-ray flux was observed to increase for several months, reaching a peak after 150 days and showing a gradual but constant decrease after the peak (see Fig. 1.9b). In the first $\simeq 900$ days following the merger, the spectrum in the X-ray and radio bands was dominated by the synchrotron non-thermal emission produced by an ultra-relativistic structured jet, that is a wide structure with an angular gradient in energy and expansion velocity, which was pointing at an angle $\sim 15 - 25$ degrees relative to our line of sight (S. E. Woosley, 1993; Hotokezaka, Nakar, et al., 2019).

Indeed, if the GRB produced a structured jet, an observer not directly looking on-axis would miss the initial brighter part of the emission, which would be relativistically beamed away, and would start to observe a signal only when the material moving along its line of sight at a lower Γ-factor, starts decelerating in the ISM (a lower Γ implies a later deceleration time). From that point on, more and more flux is received as the decreasing Γ reduces the degree of relativistic beaming, and the observer sees progressively closer to the core of the jet. Eventually, a peak is reached when the jet core is observed, that is when $\Gamma \sim \theta_{\rm obs}^{-1}$, and from that point on the flux starts decreasing because of the normal late decay afterglow emission (Fig. 1.10a and 1.10b).

The fact that GRB 170817 is the only case observed with the unique features described above is directly linked to the fact that it happened really close to us, so we could detect its emission even if it was very weak, being observed significantly off-axis. In general, as explained in Section 1.3.5, the only GRBs we are able to observe are the ones directed within $\sim$ 10 deg of our line-of-sight, i.e. roughly 1% of the population, while those seen at a larger angle are completely missed. Luckily, GRB 170817 was very close to Earth, so we were still able to receive its signal even if we were significantly misaligned with its jet: in doing so, we could discover its odd temporal behaviour, a telltale of the jet structure.

Because the afterglow of GRB 170817 is not a "canonical afterglow" as portrayed in Section 1.3.2, we have excluded it from our sample: indeed, since plateaus are observed in the first hours following the trigger, the non-detection of X-ray data for the first nine days in the case of GRB 170817 makes it impossible to state whether this burst had a plateau or not.

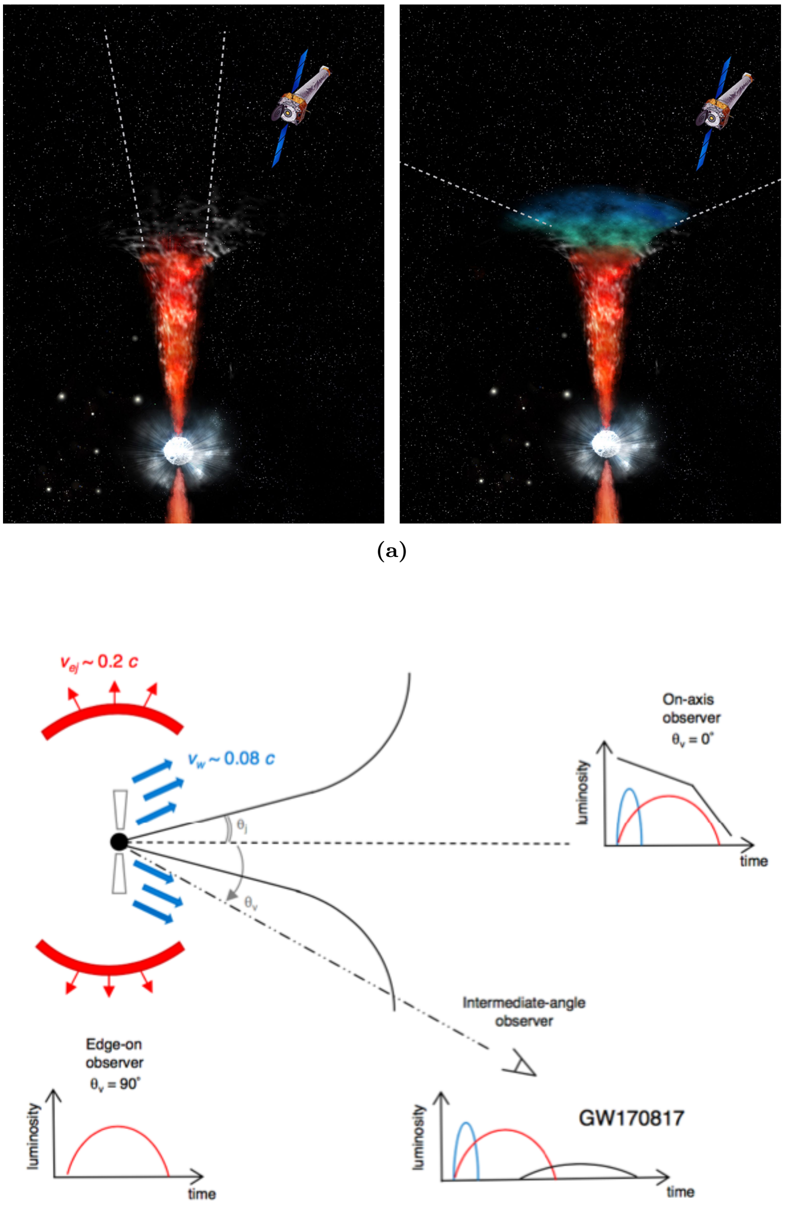

(a)

(b)

Figure 1.10: **(a)** Artistic illustration (credit: NASA/CXC/K.DiVona) showing the time evolution of the jet of GRB 170817: the jet was initially narrow and since Chandra was observing it off-axis, it was not able to observe X-ray emission, while as time passed, the jet propagating into the surrounding material slowed down and widened, allowing Chandra to observe it for the first time only after some days. The Chandra data were fundamental to estimate the angle between the jet and our line of sight. **(b)** Observed electromagnetic emission following a binary neutron star merger and how it varies depending on the angle of our line of sigh. The three main emission are: the isotropic kilonova produced by neutron rich ejecta, peaking in the infrared (in red); neutron-free wind producing the kilonova emission in the optical (in blue); a relativistic collimated jet which emits in X-ray, optical and radio wavelengths (in black). For on-axis observers, the jet will outshine the other two components, while for edge-on observers the jet will be completely lost in favour of the kilonova emission. However, for an off-axis observer the jet will appear as a low-luminosity, delayed emission appearing after several days (Troja et al., 2017).

1.5 Aim of the Thesis

While more than half of LGRBs displays clear evidence of plateau, for SGRBs this feature is more challenging to reveal due to the intrinsic faintness of SGRB afterglows. Despite the uncertainties, so far the fraction of SGRBs with plateau appears to be much lower with respect to LGRBs, but no solid value has been derived yet.

The main aim of this work is to conduct a comprehensive analysis on one of the most updated and complete samples of SGRBs available today (obtained considering all the SGRBs detected by *Swift* from May, 2005 to December, 2021 for which the redshift is known) in order to provide a solid value for the fraction of SGRBs showing a plateau phase in their X-ray afterglow light-curve. At first, a completely "agnostic" approach is adopted to determine how many SGRBs show a shallow phase in their X-ray light-curve, and in how many of these cases the shallow phase matches the necessary requirements to be considered a plateau (see Section 1.3.4). It is important to emphasise that, since the plateau phase cannot be explained with the standard afterglow model, the theoretical model that is adopted to describe this peculiar feature must also be able justify the fraction of SGRBs in which the plateau is not present.

Accordingly, the magnetar model (introduced in Section 1.3.5), which has already been studied in numerous works (Dall'Osso et al., 2011; Rowlinson et al., 2013; Stratta et al., 2018) giving promising results, is further tested: this is done deriving the best-fit magnetar parameters, the magnetic field strength B and the magnetar spin period P, in all the cases which resulted in showing evidence of plateau in their light-curve, in order to understand how many of them turn out to be good magnetar candidates.

Provided that, since the association of short GRB 170817 with the gravitational wave event GW 170817, compact binary mergers have been reputed the best candidates to be SGRBs progenitors, it is important to point out that the coalescence of two NS can lead to the formation of either a more massive post-merger NS or a BH: the final outcome strongly depends on the equation of state (EOS) of NS matter at supra-nuclear densities which is still an open issue in fundamental physics. Following the hypothesis that plateaus are produced by the spin-down radiation of magnetars, and further assuming that all SGRBs are produced by BNS mergers, at last the derived fraction of good magnetar candidates is linked with the fraction of BNS mergers that give birth to a stable remnant instead of collapsing to a BH: this is exploited to ultimately constrain the maximum stable mass expected for the remnant of a BNS merger, in order to infer values which are expected to be consistent with independent estimates obtained in the literature (e.g. Margalit and

B. D. Metzger, 2017; Bauswein, Just, et al., 2017; Rezzolla et al., 2018) and that may be tested by the upcoming and future science runs of the gravitational wave detectors *Advanced LIGO* and *Virgo* and, even more so, by the advent of the *Einstein Telescope*.

This Thesis is structured in the following way. A description of the *Swift* GRB mission, of the *Swift*-XRT GRB Repository and of the techniques behind the creation of XRT light-curves are provided in Chapter 2. A detailed overview of the analyzed data sample is given in Chapter 3, where all the steps of the analysis are thoroughly outlined too, while Chapter 4 is entirely dedicated to the magnetar model testing and the subsequent derivation of the magnetar parameters B and P. At last, in Chapter 5, the procedure to derive some observational constraints on the maximum stable mass of NS starting from the derived fraction of good magnetar candidates is reported and in Chapter 6 conclusion and future perspectives are described.

Chapter 2

Swift Mission and *Swift*-XRT repository

In this Thesis work, we analyzed a sample of SGRBs at known redshift detected by the Neil Gehrels Swift Observatory. In this chapter we briefly introduce this mission providing a description of two of the instruments on board and we also specify the main concepts behind the *Swift*-XRT GRB Repository. In Section 2.3, the necessary steps to pass from raw data to the products available on the repository are explained in detail.

2.1 The *Swift* GRB Mission

The Neil Gehrels Swift Observatory (from here on out, *Swift*) is a NASA satellite which was launched in November 20, 2004 with the aim of discovering a large number of GRBs during its lifetime, with a particular focus on the possibility of detecting not only the main prompt emission and its time evolution for each event, but also the multi-wavelength nature of the afterglow following the burst phase. To do this, *Swift* is equipped with three co-aligned instruments, working in different bands (Fig. 2.1): the Burst Alert Telescope (BAT), the X-Ray Telescope (XRT), and the Ultraviolet/Optical Telescope (UVOT). *Swift* is essentially a multi-wavelength observatory that can "swiftly" find bursts of gamma rays in random directions and point all its three instruments on target within less than 10 seconds (Tang et al., 2019). The spacecraft works on a 600 km, circular Low Earth Orbit (LEO) and, even though the original minimum scheduled life was of two years, its orbit is expected to remain stable until at least 2025 (Troja, 2020).

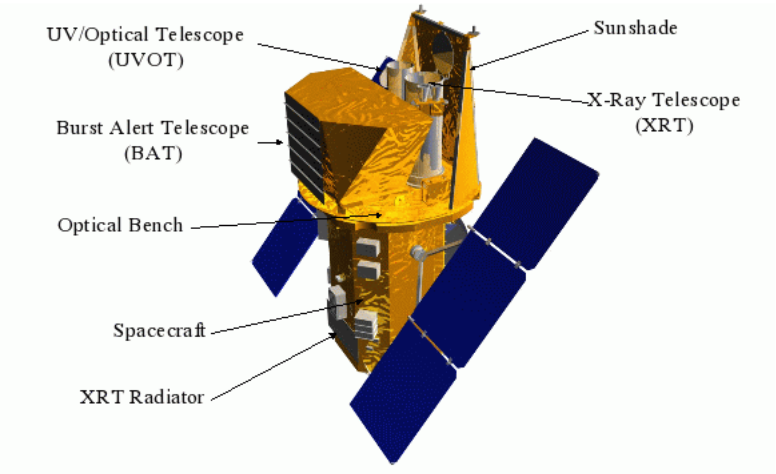

Figure 2.1: Schematic representation of the *Swift* satellite, showing all the three instruments present on board: the Burst Alert Telescope (BAT), the X-Ray Telescope (XRT), and the Ultraviolet/Optical Telescope (UVOT). These three instruments are coaligned and the *Swift* can autonomously point all the three instruments to the same location in the sky within few seconds after that the BAT detects a likely candidate GRB (Credit: NASA).

2.1.1 Instruments

The BAT is the largest instrument on-board *Swift*. It is a coded-mask instrument with a 1.4 steradian field-of-view working for imaging in the $15 - 150$ keV energy range. The BAT has a sensitivity $\sim 2 \times 10^{-8}$ erg cm^{-2} s^{-1} in 1 s of exposure that, together with its large field-of-view, enables it to detect a large number of bursts: indeed, it is able to spot almost 100 burst per year and to compute their position with a 4-arcmin accuracy directly on board. The initial position is calculated within the first ∼10 s from the burst detection and it is later used to decide if the burst is worth a spacecraft slew: if this is the case, it sends the position to the spacecraft.While looking for GRBs, BAT also performs an all-sky hard X-ray survey, simultaneously monitoring for hard X-ray transients. A list of the specifics of the BAT instrument is provided in Tab. 2.1.

The XRT is a X-ray CCD imaging spectrometer with a resolution of 18 arcsec (half-power diameter), a field-of-view of 23.6 x 23.6 arcmin and an effective area of 110 cm^2. It works in the $0.3-10$ keV energy range and focuses X-ray photons onto a CCD using a grazing incidence Wolter 1 telescope. Using the information received from the BAT, the XRT is able to locate GRBs up to a 5 arcseconds accuracy within ∼10 s of its target acquisitionand, starting from $20 - 70$ s after the burst discovery, it continuously studies the burst X-ray counterparts for days or even weeks.The great breakthrough

Burst Alert Telescope (BAT)	
Aperture	Coded Mask
Energy range	$\sim 15 - 150$ keV (imaging)
Energy resolution	~ 5 keV at 60 keV
Effective area	~ 1400 cm^2[a]
Detection Area	5240 cm^2
Field of view	1.4 sr (half coded)
Telescope PSF	22 arcmin FWHM
Location accuracy	$1 - 3$ arcminutes radius

Table 2.1: Characteristic of the BAT.

---

[a] This value is the maximum on-axis effective area, which corresponds to when all 32 768 detectors are enabled.

introduced by *Swift* is its fast slewing capability. For example, the *BeppoSAX* satellite was able to observe a typical afterglow in X-ray only after several hours from the trigger, when the intensity had already dropped by 4−5 orders of magnitude. Instead, soon after the BAT detects and locates a GRB, the *Swift* spacecraft autonomously slews in order to focus both the XRT an the UVOT at the GRB location.

It is fundamental to highlight that the low Earth orbit of *Swift* do not allow the spacecraft to observe a target continuously because of Earth occultation and pointing constraints. This is why *Swift* observations are broken in short *snapshots* with durations between 5 and 45 minutes: a set of snapshots makes up an *observation segment* (see Fig. 2.2). While the first observation segment consists of an automated set of snapshots, the following observation segments are sent from ground-centers to the spacecraft, after a careful planning. All three telescopes observe the source up to when the automated sequence ends, another source is detected or a new observation sequence is uploaded from the ground (Troja, 2020).

As previously said, the XRT is able to refine the initial position derived by the BAT up to arcseconds accuracy in the first 10 s of seconds following the trigger, starting to gather early spectra and light-curves data over an extremely wide dynamic range of seven orders of magnitude in flux. To properly cover this range and the rapid variability of GRB afterglows, the XRT supports three readout modes. The choice of which mode is more appropriate is autonomously made by the instrument itself. Imaging Mode is the one used for the initial emission of all GRBs, for source fluxes up to 7

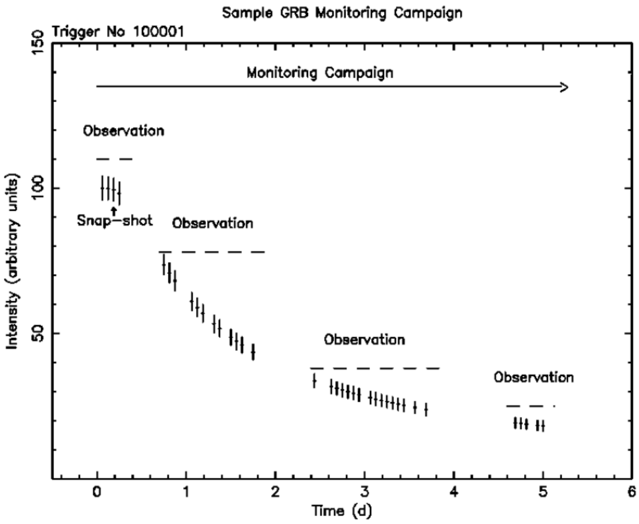

Figure 2.2: Example of a five-day observation of a GRB made by the *Swift* satellite. Each vertical segment indicates a *snapshot* with duration of ∼ 30 min due to Earth occultation. A series of snapshots builds an observation segment. Since *Swift* may have to follow-up multiple sources, observation segments for different bursts can be interlocked (Troja, 2020).

$\times 10^{-7}$ erg cm^{-2} s^{-1} (37 Crab) and produces an integrated image measuring the total energy per pixel, but does not permit spectroscopy. Windowed Timing (WT) Mode is used for sources with fluxes below 10^{-7} erg cm^{-2} s^{-1} (5 Crab) and achieves an high time resolution (2.2 ms) and a bright source spectroscopy, even though sacrificing information about position. Photon-counting (PC) Mode is used for sources with fluxes below 3×10^{-11} erg cm^{-2} s^{-1} (1 mCrab) down to 8×10^{-14} erg cm^{-2} s^{-1}, and allows full spatial and spectral information. The XRT is capable of switching autonomously between the two different working modes (WT or PC), depending on the count rate of the burst: for typical GRBs, earliest data are taken in WT mode and then the instrument switches to PC mode, but in general the XRT is able to toggle between this two modes, in particular when a rapid change in the count rate in the central window of the CCD is observed. A list of the specifics of the XRT instrument is given in Tab. 2.2.

In the following of this work our focus will be mainly on the events observed by the XRT since the launch of *Swift*, but we will as well use the BAT data, mostly as a reference to inspect the time behaviour of the prompt emission preceding the afterglow.

X-Ray Telescope (XRT)	
Telescope	Wolter 1
Detector	XMM EPIC CCD
Energy range	0.2 – 10 keV
Detecting Area	5200 cm^2
Effective Area	120 cm^2 at 1.5 keV
Field of view	23.6×23.6 arcminutes
Telescope PSF	18 arcsec HPD[a] at 1.5 keV
Location accuracy	3 – 5 arcseconds
Sensitivity	8×10^{-14} erg cm^2 s^{-1} in 10^4 s
Pixel scale	2.357 arcsec/pixel

Table 2.2: Characteristic of the XRT

---

[a] Half Power Diameter

2.2 The *Swift*-XRT GRB Repository

The dataset analysed in this Thesis work is taken from the *Swift-XRT GRB Repository* that stores all the GRBs detected with *Swift*-XRT since the launch of *Swift* in 2004. This is the official repository of the *Swift* mission and it works based upon a sophisticated and complex data-analysis algorithm entirely developed by the *Swift* team. This algorithm and the description of light-curve building and spectral extraction processes were originally published in Evans, Beardmore, Page, Tyler, et al. (2007) and Evans, Beardmore, Page, Osborne, et al. (2009) and are available on the UK Swift Science Data Center (UKSSDC) website[1]

The advanced algorithm is capable of building GRB light-curves and spectra starting from the raw event files obtained from the telescope, carefully taking into account and correcting for all the effects which contaminate the data (see Section 2.3 for a detailed description). The automatization of all these steps allows to analyse large samples of events in a very short time, being confident at once of the reliability of the results: indeed, it is important to highlight that all the products of the repository are extensively verified by the *Swift*-XRT team.

An emblematic example of the level of accuracy of the algorithm is the procedure behind the choice of the source extraction region selection: indeed, this region is not static (fixed in size) but dynamic, meaning that its

---

[1] `https://www.swift.ac.uk/index.php`

dimension is optimized on the basis of the source photon flux. Dynamic source extraction regions are of fundamental importance in the case of variable sources, such as GRBs.

Moreover, the algorithm also takes into account the different data reduction process required for each data acquisition mode (WT or PC) automatically.

In addition to the XRT light-curves, the repository web page provides a number of tools that allow to further analyse *Swift* data. The one which was used the most for this work is the *Swift* Burst Analayser (Evans, Willingale, et al., 2010), presenting BAT and XRT light-curves in flux and flux densities, corrected for the absorption (see Section 2.2.2). For our purpose, we always selected the $0.3-10$ keV integrated flux dataset for XRT, and the $15-150$ keV dataset for BAT, since these are respectively the native band-passes in which each of the two instruments works.

As explained in Section 2.3, what can be directly derived from the telescope data after a preliminary analysis are the count rate light-curves, i.e. at which rate the photons are detected over the band-pass of the instrument as a function of time. But physical models predict energy fluxes and for this reason it is fundamental to convert the observed count rate light-curves into flux light-curves. In the following sections, the ideal procedure to apply the count-to-flux conversion is outlined at first, before explaining how the same result is achieved by the XRT repository algorithm.

2.2.1 Standard count-to-flux conversion

Computing the Energy Conversion Factor (ECF) is the fundamental step required to convert count rate light-curves into observed flux-light-curves: the ideal procedure to derive it is described in the following.

We recall that the photon counts (C) within defined channels of a spectrometer (I) are linked to the real spectrum of the source $f(E)$ as (Arnaud et al., 2023):

$$C(I) = \int f(E)R(I,E)dE, \tag{2.1}$$

where $R(I,E)$ is the instrumental response which provides to the probability for a photon with energy E to be detected by the channel I of the instrument. Inverting Eq. 2.1 is in general not possible because this inversion is very sensitive to small changes in $C(I)$ (Kahn & Blissett, 1979). The alternative to this procedure is to choose a model spectrum that is function of a few parameters (i.e., $f(E,p_1,p_2)$). For each set of parameter, a predicted count spectrum $C_p(I)$ is derived and compared with the observed count spectrum

$C(I)$. To understand how well the model reproduces the observed data, a χ^2 fit statistic is used, defined as follows:

$$\chi^2 = \sum \frac{(C(I) - C_p(I))^2}{(\sigma(I))^2}, \tag{2.2}$$

where $\sigma(I)$ is the error for the channel I (if $C(I)$ are counts following a poissonian distribution, then $\sigma(I)$ is expressed as $\sqrt{C(I)}$). It is then possible to vary the model parameters in order to find the values for which the model spectrum returns the best fit statistic, i.e. the one which gives the minimum χ^2 or $\chi^2/\nu \sim 1$, where ν is the number of degrees of freedom.

After having derived a best fit model spectrum for a given temporal bin, one can integrate the model in the $(0.3 - 10)$ keV energy range obtaining a value of the integrated flux expected from that particular spectral model. Computing the ratio between this integrated flux and the count rate flux integrated in the same energy range, one obtains the value of the ECF in that bin. Once the value of the ECF in a certain bin is known, it is sufficient to multiply it by the count rate flux in that bin to derive the value of the observed integrated flux in that specific bin. So repeating this procedure for each count rate light-curve bin, one can build the corresponding observed flux light-curve.

It is important to point out that a best fit model is often not unique: indeed, changing the model spectrum, one can obtain similar values of the χ^2: in this case the choice of the best model must undergo a deeper scientific analysis.

2.2.2 XRT repository count-to-flux conversion

Given the spectral variability of GRB afterglows, the ideal procedure to derive the ECF would be to perform a spectral fitting in each temporal bin, as described above, but performing spectral fitting requires a large number of counts in each single bin (≥ 20 to apply χ^2 statistic) and this is not the case in GRBs, and in particular in SGRBs, if the adopted temporal resolution is of the order of the spectral variability timescale. To obviate to this problem, the algorithm proposed in Evans, Willingale, et al. (2010) assumes a power-law spectra for the X-ray emission of the GRB and, for each temporal bin, it computes the photon index Γ which better reproduces the hardness ration (HR) in that bin. For the XRT, the HR is defined as ratio between the number of counts in the hard band over the number of counts in the soft band, namely $(1.5 - 10\,\mathrm{keV})/(0.3 - 1.5\,\mathrm{keV})$. After having defined a best fit value for Γ in a given bin, it is possible to proceed as in Section 2.2.1 and derive the value of ECF in that bin. Usually the temporal resolution used for HR bins is lower than the desired one, given that it is important to have enough statistics when deriving hardness ratios: for this reason, once a time series of ECF is derived, the best way to obtain the ECF value in a specific light-curve bin is by interpolating the ECF time series.

Note that the best-fit value of Γ is found by taking into account galactic and local absorption components too. Galactic absorption is taken from the values of Galactic column density N_H reported in Kalberla et al. (2005). We recall that N_H is the equivalent hydrogen column density and indicates the number of H atoms required to reproduce the observed photoelectric absorption, given a chemical abundance (generally the solar system's one). Since the neutral hydrogen distribution in the Milky Way has been mapped in detail, the value of the galactic N_H is just a function of the position of a certain object in the sky. Once galactic absorption is included in the spectral model, all the residual absorption effects are ascribed to local absorption, that is the absorption due to material in the host galaxy (indeed, the extremely low densities of the intergalactic medium allow to assume it as void in first approximation) and can be easily derived knowing the GRB redshift. This absorption component is derived from the late time spectrum of the GRB ($T > 4000$ s), since at late times we expect low spectral variability. If late time data are too few to construct a spectrum, the absorption components are derived from the XRT spectrum on the spectra repository[2]. The absorption values adopted and details on how they were derived can be retrieved on the Burst Analyser page for each GRB.

2.3 XRT data reduction and light-curve extraction

As already stated in the previous section, all the observed flux light-curves analysed in this Thesis work are retrieved directly from the *Swift*-XRT GRB Repository, since the reliability of these data is guaranteed by the fact that all the products found on the repository are constantly tested by the *Swift* team itself. The algorithm introduced by Evans, Beardmore, Page, Tyler, et al. (2007) takes into account all the fundamental steps of the data reduction and, starting from the Level 0 Telemetry data received from the spacecraft, it builds light-curves and spectra (Level 3 files, see Fig. 2.3) for each event and it is optimized to obtain the highest signal-to-noise ratio. The advantage of using the repository is that it allows the study of large samples of bursts

---

[2] `https://www.swift.ac.uk/xrt_spectra/index.php`

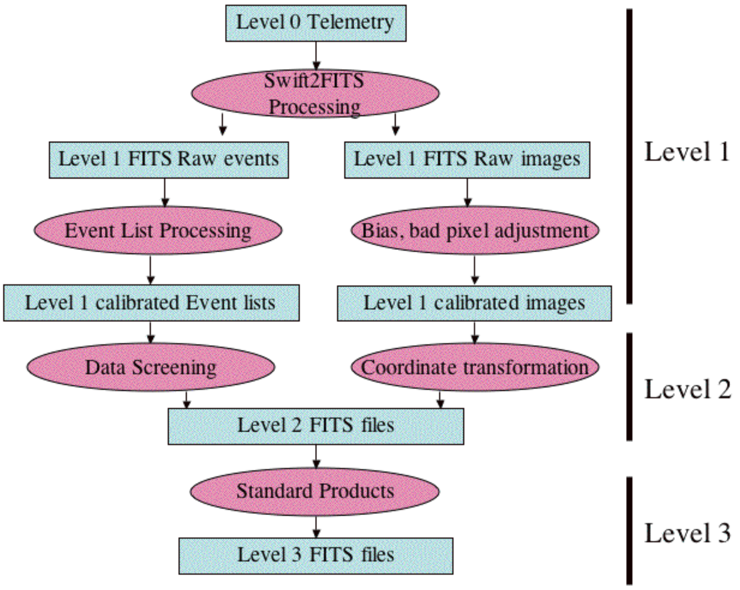

Figure 2.3: Flow diagram indicating the different levels in which the processing of *Swift* data consists. The raw telemetry is transformed in Level 1 FITS file which, after data screening and coordinate transformation, will be converted in Level 2 FITS files. Eventually, the latter products will go trough the script for each instrument, leading to the spectra and light-curves (Level 3 files).

without having to perform by hand the data reduction in each single case. However, for illustrative purposes, in the following we report the fundamental steps of the data reduction.

2.3.1 XRT pipeline

The Level 0 Telemetry data coming from the spacecraft arrive at the Swift Data Center (SDC) at Goddard Space Flight Center (GSFC) from the Malindi ground station and are used to create raw (Level 1) FITS files containing event data for each instrument without any kind of filtering (bad pixels, spurious events...). The XRT files include, in addition to XRT (both event and housekeeping) data, auxil data (containing attitude information) and TDRSS data (containing telemetry information, which can be useful when the value of the trigger time is needed). Starting from Level 1 files, its is possible to run the XRT pipeline, a series of several procedures that will gradually clean and filter the files, leading to the creation of processed (Level 2) FITS files. To run the pipeline, some input parameters are needed: the source right ascention (RA) position and the source declination (DEC) position, the stem of the observation (an alphanumeric code composed by the letters "*sw*" followed by the Observation ID and other numbers related to the trigger), the input and the output directory. Many files are created by the pipeline, but the most important ones are the cleaned event files (Level 2), in which all the bad data linked to flawed CCD pixels or columns[3], cosmic rays contamination, unstable pointings, high CCD temperatures are carefully taken into account and either corrected or excluded. For example, exposure maps are created and used to correct for the loss of flux due to the fact that, after the XRT CCD being hit by a micrometeoroid in May 2005, some of the CCD pixels were damaged and could not be used to collect data anymore.

2.3.2 Count rate light-curve extraction

The Level 2 output event files produced by the pipeline are not ready to be used to produce a light-curve. Indeed, the cleaned event files are obtained by performing a background subtraction considering a mean background computed over the whole region of observation. But in the case in which other field sources are present in the field of view of the instrument, this averaged value is contaminated and this could lead to erratic results. Indeed, even if the GRB is dominating the emission at the beginning, as it starts to fade at late times a wrong value of the background could significantly change the source count rate estimate. To prevent this, it is important to select a background extraction region avoiding eventual field sources: this can be done manually using the SAOimage DS9 software, but it is important to recall that the XRT repository algorithm automatizes this whole process.

Another problem that can affect the Level 2 files and must be corrected before building the light-curves is the pile-up. Pile-up occurs when multiple photons detected within a given CCD frame have overlapping charge distributions and this will result in a total charge spatial distribution that will either be the sum of the overlapping events (e.g., two soft X-ray photons registered as a single hard X-ray photon) or a flux loss if the total charge becomes too high to be classified as an X-ray event by the XRT. In PC mode, pile-up is expected at intensities of about ~ 0.3 count s^{-1}, while in WT mode data are not expected to be affected by pile-up below intensities of about ~ 100 count s^{-1}. Using the XSELECT command line interface it is possible to select the time interval in which we expect to have pile-up in our data: from these data, one can create a FITS image and using, the XIMAGE program for X-ray image display and analysis, select from it a region from which a point spread function (PSF) of the source will be extracted. Fitting

---

[3] These pixels/columns are defined either as "bad" or "hot": the former are the ones with a lower or null response, while the latter are the ones which have a much higher dark current with respect to the neighbours and appear very luminous.

this PSF with the PSF model provided by the UKSSDC team, it is possible to individuate the region in which the pile-up becomes important: indeed, pile-up affects the center of the PSF in such a way that fewer counts will be seen with respect to the model PSF, while in the outer wings the fit with the model function will be accurate. It is then fundamental to fit the model in the outer wings and extrapolate it to the inner region, in order to compare it with the data points and to understand at which distance from the center the model no longer fits the data (remember: 1 pixel = 2.357 arcsec). This allows to select an annulus region not affected by pile-up that will be used for the source extraction.

Once the annulus is defined, it is possible to proceed with the actual light-curve extraction. Through the use of the command line interface XSELECT, it is possible to extract both a source light-curve from the annulus region selecting a given time range and bin size[4] and, using the same settings, a background light-curve from the previously selected background region. Afterwards, light-curve exposure correction has to be applied to both light-curves, and this is accomplished thanks to the *Swift* tool *xrtlccorr*, which computes a correction factor for every snapshot to correct both the loss of counts due to bad pixels and hot columns and, in the case in which pile-up is present, also the loss due to the annular shape of the extraction region. The final step consists in considering the exposure corrected source light-curve and subtracting from it the background light-curve multiplied by a scale factor given by the ratio between the source extraction region and the background extraction region (in order to renormalize the background counts): eventually, one obtains the final count rate light-curve that can be found on the repository (Level 3 file, see Fig. 2.4).

Data products are placed on the Quick-Look data area from where they will be available to the GRB community few hours after the observation occurs, as soon as they have been processed by SDC at GSFC. After one week, the data are moved to the main archive and removed from the Quick-Look area.

---

[4] The minimum bin size which can be used depends on the XRT mode and corresponds to the frame time of the mode, e.g. 1.8 ms for WT mode and 2.51 s for PC mode.

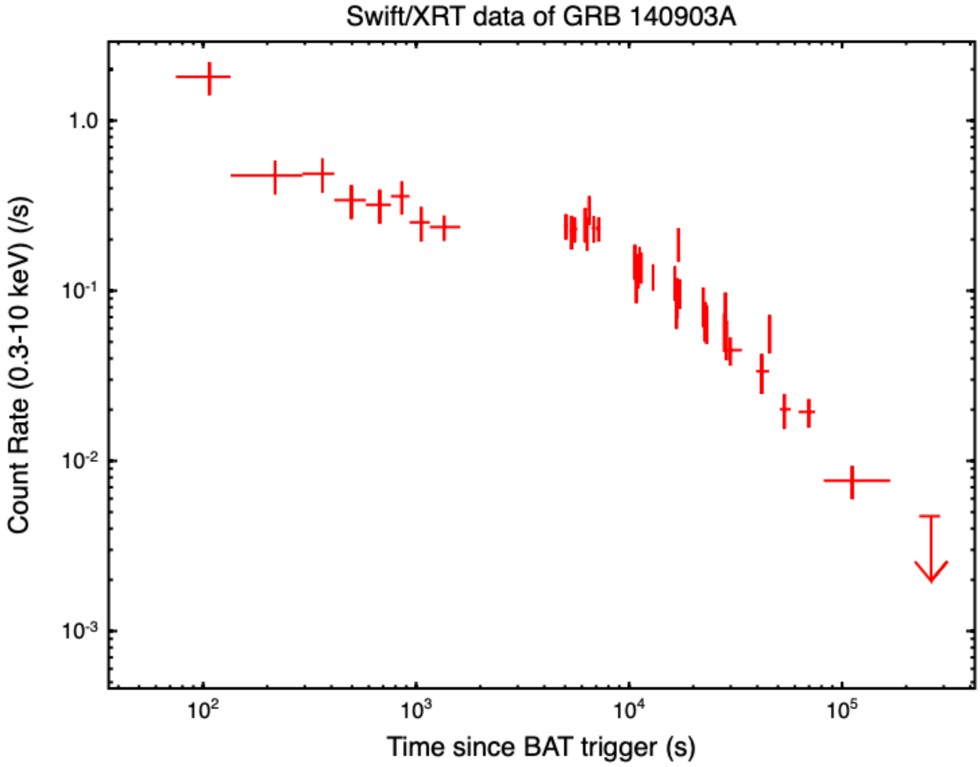

Figure 2.4: Example of a count rate light-curve available on the *Swift*-XRT GRB repository for GRB 140903A. Red points represent data taken in the PC mode and the time axis is in logarithmic scale.

Chapter 3

Data analysis

In this chapter we thoroughly describe all the steps of the analysis we carried out. At first, a detailed description of the sample selected for the purpose of this work is given in Section 3.1. A preliminary selection of the "uninformative" cases is described in Section 3.2, while the actual light-curve fitting is performed in Section 3.3 and leads to the definition of the "BPL" subsample. A further characterization of this latter is given is Section 3.4, where the final "plateau" subsample is identified. A discussion of the results and the derived "plateau" fractions are given in Section 3.5.

3.1 The SGRB sample

The sample analysed in this Thesis work is composed by 85 SGRBs and includes all the SGRBs at known redshift detected by *Swift* from May, 2005 to the end of December, 2021 ($\simeq 60\%$ of the total *Swift* short GRB population, W.-f. Fong et al., 2022). SGRBs without an associated redshift were excluded from our analysis, in order to have the chance to compare the results with theoretical models: indeed, to test model predictions regarding the X-ray light-curve intrinsic luminosities is possible only if the redshift of the source is known (see Chapter 4 for more details). This sample was singled out by PhD student Paramvir Singh under the supervision of Dr. Giulia Stratta and Dr. Andrea Rossi, building on the works of Rossi et al. (2020), W.-f. Fong et al. (2022), and O'Connor et al. (2022) and it represents the most updated and complete sample of short GRBs at known redshift observed by *Swift* available to date.

In Fig. 3.1, the redshift distribution of the 85 bursts included in our sample is shown. The redshift values range from a minimum of $z = 0.0763$ to a maximum of $z = 2.609$. The median redshift is $\langle z \rangle = 0.60$, while the average redshift is $\overline{z} = 0.79$.

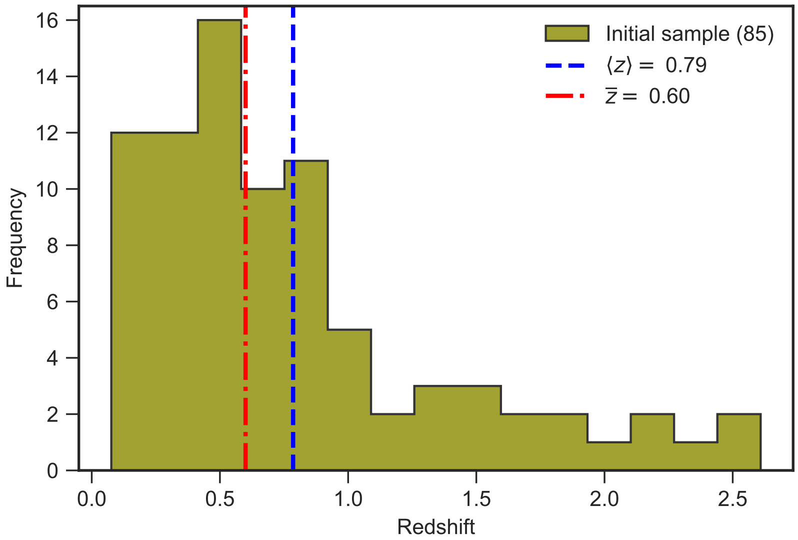

Figure 3.1: Redshift distribution of our sample of 85 SGRBs, ranging from a minimum of $z = 0.0763$ to a maximum of $z = 2.609$. The median redshift is $\langle z \rangle = 0.60$ while the average redshift is $\overline{z} = 0.79$.

For each SGRB in the sample, the XRT $0.3 - 10$ keV (unabsorbed flux) X-ray afterglow light-curve was retrieved from the Burst Analyser page on the UK *Swift* Science Data Center website (see Section 2.2). These are the light-curves on which we based our study. However, even though our analysis is devoted to the study of the afterglow, XRT data frequently include late prompt emission data too, identifiable on account of their different spectral and temporal behaviour. In order to individuate more accurately the onset of the afterglow, we decided to represent on the same plot also the BAT $15 - 150$ keV unabsorbed flux light-curves data, so that we could simultaneously have a look both at the prompt emission and the afterglow emission. It is important to underline that BAT data were not used in the analysis but just utilized as a reference to interpret in the correct way the XRT light-curves evolution and specifically to correctly individuate the start of the afterglow phase after the prompt phase. Notice that we chose to represent BAT and XRT data in the corresponding detector energy band rather than doing an extrapolation in an energy band that was not the native one, since this was not necessary for our study and would have introduced systematic errors.

An example of a light-curve derived from the data taken from the UKSSDC repository and presented following the guidelines explained above is given in

Fig. 3.2. BAT data are reported in black, while XRT data are in red. We decided also to report the photon index evolution in the subplot, because the study of its time behaviour is a key point of our analysis (see Section 3.4).

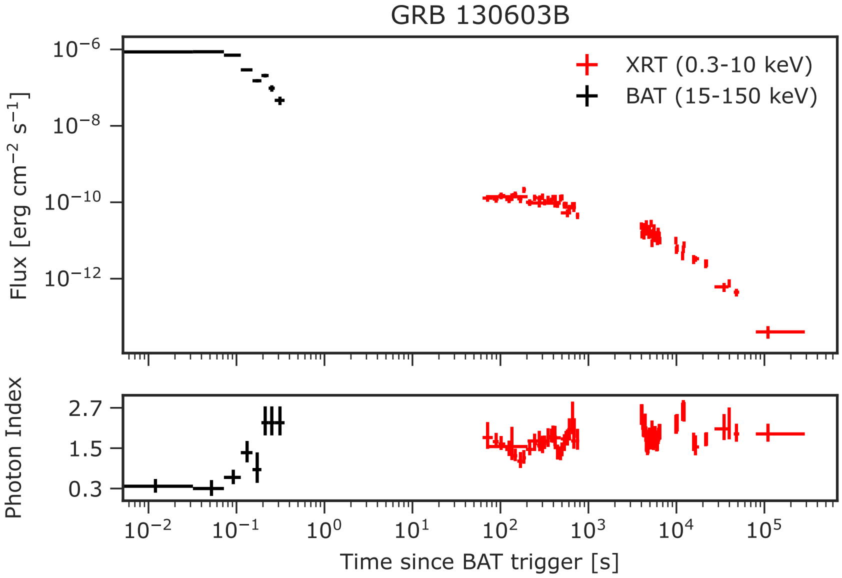

Figure 3.2: Example of one of the light-curves studied in our analysis, showing the time evolution of the emission of GRB 130603B, corrected for galactic and local absorption: black data represent BAT integrated flux in the energy range $15-150$ keV, while red data represent XRT integrated flux in the range $0.3-10$ keV. In the subplot, the time evolution of the photon index Γ relative to both BAT and XRT data is reported too. Both axes are in logarithmic scale.

For the sake of clarity, we divided the analysis in three main phases: each of them is described in detail in the following sections.

3.2 Classification of "uninformative" events

For the purpose of deriving a fraction of SGRBs showing a "plateau" phase, it is fundamental to individuate those bursts for which, for different reasons, it was not possible to properly study the afterglow time evolution. This led to the delineation of three subsamples (described in the following sections), comprehensively referred to as "uninformative" events, which were found to be not suitable to be submitted to the light-curve fitting procedure.

3.2.1 SNR-rejected events

As previously said, SGRBs are characterized by faint afterglows, and this makes it very challenging to obtain well sampled and time-resolved light-curves. This indeed was true for a large number of the SGRBs in our sample for which the limited statistics made almost impossible to draw conclusions about the afterglow morphology. Two examples of poorly-sampled light-curves are shown in Fig. 3.3.

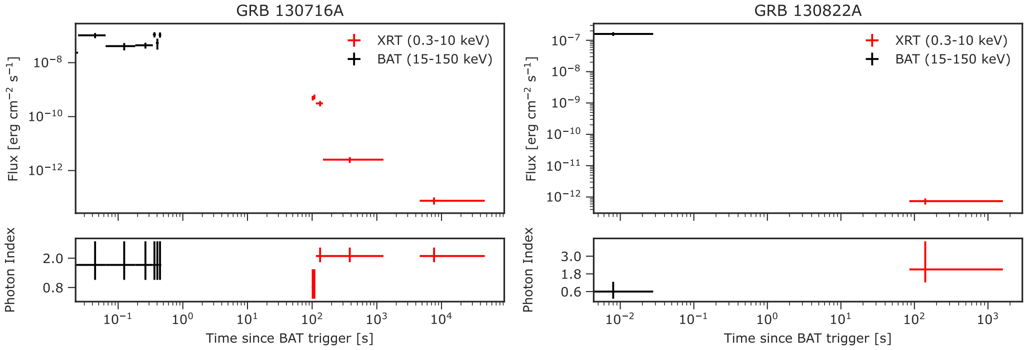

(a) **(b)**

Figure 3.3: Two light-curves representative of the bursts excluded because their sampling was too poor. As it is evident by inspecting the two plots, **(a)** GRB 130716A and **(b)** GRB 130822A, only few XRT are present: in both cases, it was not possible to do any kind of analysis of the afterglow morphology and this is the reason why they were excluded using the SNR criterion explained in the following.

The criterion we adopted to understand if a certain burst did not have enough data to be considered for a deeper analysis was based on the number of total counts detected by the XRT for each GRB, and in particular on the signal to noise ratio (SNR). Specifically, the cases which were rejected in this part of the analysis were the ones for which the total $\mathrm{SNR}_{\mathrm{tot}}$ of the XRT observation did not overcome the threshold:

$$\mathrm{SNR}_{\mathrm{tot}} \geq 10. \tag{3.1}$$

Indeed, assuming a poissonian statistic (that is what we deal with when considering high energy photon detections), the SNR is proportional to the square root of the counts, and the threshold given in Eq. 3.1 translates in a number of counts $\gtrsim 100$. This value guarantees the possibility to build a light-curve with at least 5 bins, each of the them with an SNR$\gtrsim 4.5$, which is the minimum requirement to assure to have enough counts to be able to properly model its morphology. Thanks to the light-curve tool on the UKSSDC repository, it was possible to re-bin every light-curve as a single binned light-curve, obtaining the number of total XRT counts and the error on this value. Using these two values, it was possible to calculate the total SNR of XRT data ($\mathrm{SNR}_{\mathrm{tot,\,data}}$) and the cases for which $\mathrm{SNR}_{\mathrm{tot,data}}$ did not overcome the threshold given by Eq. 3.1 were classified as "SNR-rejected" cases: 25 bursts out of 85 were included in this subsample.

3.2.2 Extended emission-only (EE-only) cases

As explained in Section 1.2.1, a fraction of SGRBs shows a soft and prolonged emission subsequent to the prompt, labeled as *extended emission* (EE). EE is typically observed in the first tens of seconds after the burst trigger and in many cases is detected by the XRT as a bright signal at early times. EE is characterized by a very high flux and spectral variability and a sharp flux decay indicating its ending. As anticipated in Section 3.1, XRT data often include the tail of the prompt emission and, as mentioned in Section 1.2.1, EE is interpreted as the low-energy tail of the prompt emission: this leads to the conclusion that its physical origin is not the same as for the afterglow and suggests to treat very cautiously the cases in which EE is observed.

To individuate the SGRBs in the sample showing EE features, the following general criteria were used:

1. the bulk of XRT data lies in the time range roughly between 100 and 500 seconds from the trigger time;
2. a pronounced photon index Γ variability is present, usually showing an increase (*spectral softening*);
3. a rapid flux decay marks the EE phase end, with $F(t) \propto t^{\alpha}$ with typically $\alpha > 2$ (sometimes $\gg 2$);

Taking this into account, we decided to create a subsample of bursts which, despite overcoming the SNR threshold provided for in Section 3.2.1, resulted not suitable for our afterglow analysis, because their light-curve and spectral evolution were consistent with being EE alone, without afterglow emission. In some other cases, even though afterglow data were present after the EE phase, they were too few to draw any conclusion about the afterglow morphology. Eventually, 19 bursts were found to match with these criteria: we then decided to include them in the "EE-only" subsample. The light-curves of two of these cases are portrayed in Fig. 3.4.

It is important to point out that clear signs of EE were found in several other bursts in our sample but these cases were not excluded, because their afterglow light-curves had enough statics to allow a proper light-curve fitting.

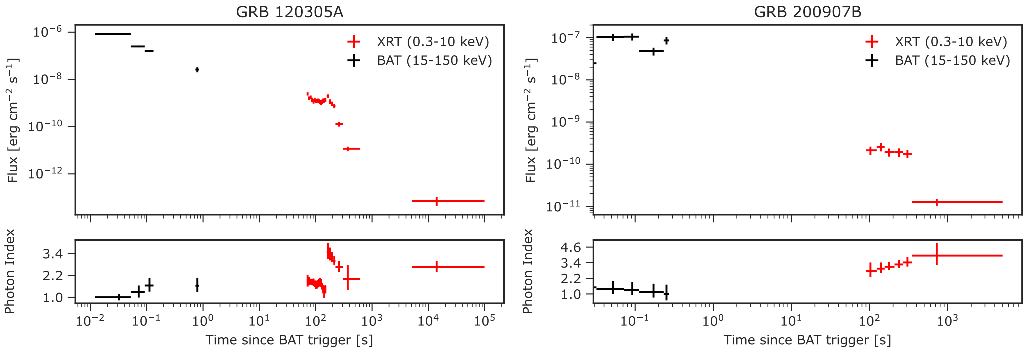

(a) **(b)**

Figure 3.4: Two light-curves representative of the bursts classified as EE-only. In **(a)** we can see an extended emission phase, followed by very few data related to the afterglow, while in **(b)** we observe the EE phase and the subsequent drop, but no detection related to the afterglow phase.

3.2.3 Special case: GRB 150101B

Among the 85 SGRBs included in our initial sample, GRB 150101B was found to exhibit a peculiar behaviour which required a separate discussion. Indeed, XRT observation for this burst started at $\sim 1.42 \times 10^5$ seconds from the burst trigger. This can be justified considering that it was discovered through *Target Of Opportunity* observations: indeed, this GRB was not directly detected by *Swift* but only by *Fermi* Gamma-ray Burst Monitor (GBM) and the source was found in BAT data only after ground analysis (see GCN circular, Cummings, 2015). This is the reason why the XRT observed this source only several hours after the trigger, as a follow-up observation of the burst detected by GBM. In any case, since plateaus are expected to last about a few hours after the burst trigger, this burst turned out to be too late to be useful for our analysis: this is why we decided to exclude it, together with the under sampled cases.

A summary of all the 45 cases excluded in this preliminary analysis is given in Tab. 3.1, while a graphic representation of the sample is portrayed in Fig. 3.5. The remaining 40 cases, which defined the so-called "LC fit" sample, were the ones for which a further analysis was possible, as thoroughly explained in the next section.

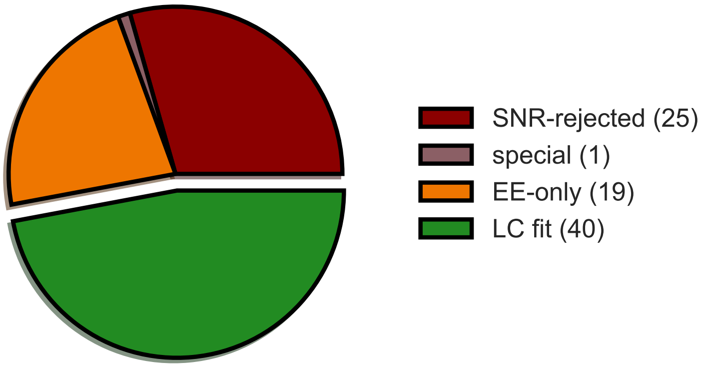

Figure 3.5: Pie chart showing the results of the preliminary classification of the cases which were not suitable for the light-curve fitting, starting from the 85 bursts included in the initial sample. Three subsamples were cast aside since they resulted not suitable for the light-curve fitting analysis: "SNR-rejected" (25, in brown), "EE-only" (19, in orange) and the "special case" of GRB 150101B (in gray). The remaining 40 cases, defined as "LC fit" sample (in green), are the ones for which a further analysis will be carried out in the following section.

Subsample	GRB name	z	GRB name	z	GRB name	z	GRB name	z	Amount
SNR-rejected	050509B	0.2248	070729	0.52	130822A	0.154	170428A	0.453	25
	050813	0.719	100206A	0.407	140622A	0.959	201221D	1.055	
	060502B	0.287	100625A	0.452	141212A	0.596	210919A	0.2415	
	(060505)	0.089	101224A	0.454	150728A	0.461	(230307A)	0.065	
	061210	0.4095	120630A	0.3	160411A	0.82			
	061217	0.827	130515A	0.8	161104A	0.793			
	070429B	0.902	130716A	2.2	170127B	2.28			
EE-only	051210	2.58	080905A	0.1218	150120A	0.4604	191031D	1.93	19
	060801	1.131	090515	0.403	160408A	1.90	200219A	0.48	
	071227	0.381	100117A	0.914	160410A	1.7177	200907B	0.56	
	080123	0.495	101219A	0.7179	160624A	0.4842	(211227A)	0.228	
	080503	0.8245	120305A	0.225	181123B	1.754			
Special	150101B	0.134							1
Total									**45**

Table 3.1: Summary of the 45 cases excluded from the light-curve fitting analysis.

3.3 Light-curve fitting

Neglecting the "SNR-rejected", the "special" and the "EE-only" cases, we were left with a sample of 40 SGRBs for which it was possible to study the afterglow light-curve behaviour: we define this as the "LC fit" sample.

In particular, assuming a power-law like flux evolution (e.g., Eq. 1.15), we tried to understand in how many cases the afterglow showed a "canonical behaviour" as explained in Section 1.3.4. It is important to point out that, since the XRT slews to observe the burst only tens of seconds after BAT trigger, in the cases in which prompt emission is brief (as in SGRBs) we observe a characteristic time gap between BAT data and XRT data. But in some of these cases, the XRT is able to catch the end of the prompt emission in its observation: this is the first phase of the "canonical afterglow", labeled as steep decay phase, and we did not consider it for the fit. We instead focused on investigating the presence of the following two phases, which are the "shallow decay" (or "plateau") phase and the "post-plateau" phase.

A necessary condition for the presence of a plateau is that the afterglow light-curve, which referring to Eq. 1.15 is expected to follow a power-law behaviour, should present a break in the flux time evolution. The first thing we did was then to identify in how many bursts this break was present. To do this, we performed a fit of the XRT light-curves using a simple power-law and a broken power-law model. The reduced χ^2 obtained from the fit performed with these two models were compared using an F-test, to determine if adding a temporal break to the simple power-law model led to a statistically significant improvement or not.

A description of the two models is given in the following.

- The first model is a simple power-law (PL) function, that is what we expect for a GRB that is not showing any evidence of a plateau in its light-curve and can be accounted using the standard synchrotron afterglow model provided for in Section 1.3.2. The simple power-law is written in the form:

$$F_{\mathrm{pl}}(t) = F_{\mathrm{pl,norm}} \left(\frac{t}{t_{\mathrm{norm}}} \right)^{-\alpha} \tag{3.2}$$

  where t_{norm} is an arbitrary normalization time, $F_{\mathrm{pl,norm}}$ is the normalization constant while (namely the value of the flux at t_{norm}) and α is the power-law temporal decay index.

- The second model is the so called "smoothly broken power-law" (BPL) function, as presented in Li et al. (2012) and Tang et al. (2019). This model is a simple way to reproduce what one would expect in the case in which a plateau phase is effectively present in the flux time evolution. The function takes the form:

$$F_{\mathrm{bpl}}(t) = \frac{F_{\mathrm{break}}}{2^{-1/\omega}} \left[\left(\frac{t}{t_{\mathrm{break}}} \right)^{\alpha_1 \omega} + \left(\frac{t}{t_{\mathrm{break}}} \right)^{\alpha_2 \omega} \right]^{-1/\omega} \tag{3.3}$$

where α_1 is the power-law index during the shallow phase (plateau) while α_2 is the power-law index during the following decay phase[1], $t_{\rm break}$ is the so called break time (observed end time of the plateau phase), ω is a smoothness parameter to control the sharpness of the transition between plateau phase and decay phase (an higher value corresponding to a sharper break) and $F_{\rm break}$ is the value of the flux at the end of the plateau.

The BPL model introduces three new free parameters with respect to the PL: α_2, $t_{\rm break}$ and ω. However, since in the cases with lower statistics having too many free parameters would make it hard for the fit to converge, the smoothness was fixed to the value $\omega = 3$, as previously done also in the works of Li et al. (2012), S.-X. Yi et al. (2016), and Tang et al. (2019).

The fit with both PL and BPL models was performed singularly on each of the 40 cases included in the "LC fit" sample. For each burst, an initial time t_0 to start the fit was defined: this was determined on an individual basis, in order to make sure that XRT data relative to late prompt/extended emission phase were not considered in the fit. This was done excluding the early-time XRT data for which the associated flux and photon index exhibited a strong time variability: indeed, for the afterglow phase, the photon index is expected to be on average constant in time. The normalization time of the PL, $t_{\rm norm}$, was arbitrarily chosen to be subsequent to t_0, specifically $t_{\rm norm} = t_0 + 3500$ s.

To understand if the introduction of the break led to a statistically significant improvement of the fit or not, the results obtained for PL and BPL model were compared through an F-test.

3.3.1 The F-test

The F-test is used to evaluate the improvement of a fit due to the assumption of a more detailed model with respect to the original, because of the inclusion of additional parameters. In general, an F-test is used to assess whether the null hypothesis H_O, i.e. the original model, should be rejected or not with respect to the alternative hypothesis H_A, i.e. the more detailed model.

To apply the F-test, after having computed the fit with both the original and the alternative model, it is necessary to calculate the *sum of square errors* (SSE), summing the squared differences between the observed quantity y_{real} and the value $\hat{y}_i$ predicted by the model:

$$SSE_i = \sum (y_{\rm real} - \hat{y}_i)^2, \tag{3.4}$$

---

[1] We alert to pay special attention to the notation applied, since the indices here labeled as α_1 and α_2 for convenience, are the same indices that in Section 1.3.4 were respectively labeled α_2 and α_3 (in line with the convention widely adopted by the community).

where the subscript i refers to the model we are using, namely O for the original model and A for the alternative model. Using this equation, it is possible to compute SSE_O and SSE_A for the original and the alternative model respectively. The F-test uses the F-statistics in order to evaluate which of the two models is more statistically significant, based on the difference in the error between them. This leads to computing the F-value as:

$$F^* = \frac{SSE_O - SSE_A}{\nu_O - \nu_A} \div \frac{SSE_A}{\nu_A}, \tag{3.5}$$

where ν_O and ν_A are the degrees of freedom of the two models (computed as the difference between the number of data points and the number of free parameters in the model).

The application of the F-statistics provides for the rejection of the null hypothesis H_O in the case F^* is large or, alternatively, if the p-value associated to it is small. We recall that the p-value can be calculated as the complement to one of the cumulative distribution function (CDF)[2] of the F variable (following an F-distribution) evaluated at F^*, and represents the probability of obtaining a value of F^* equal to or larger than what actually observed, under the assumption that the null hypothesis H_0 is true: the lower the p-value, the more unlikely to obtain such an extreme outcome under the null hypothesis. The rejection threshold can be chosen arbitrarily and for this analysis it was set to a 4σ level to align with the threshold adopted on the *Swift*-XRT repository to consider the addition of a break significative (Evans, Beardmore, Page, Osborne, et al., 2009): this corresponds to a p-value of 6.2×10^{-5}. In this way, each time the computed p-value is below this threshold, the alternative model (BPL) represents a statistically significant improvement with respect to the original model (PL) in reproducing the data, while for higher p-values the PL model is preferred.

The analysis allowed to single out 15 cases out of 40 for which the break was found to be statistically significant: these defined the "BPL" subsample. Instead, for the other 25 cases, the PL model resulted sufficient to describe the flux time evolution: these bursts were identified as the "PL" subsample.

Light-curves relative to two cases in which the PL model reproduced better the data are shown in Fig. 3.7a and Fig. 3.7b, while light-curves for two cases in which the BPL model resulted in being statistically significant are shown in Fig. 3.8a and Fig. 3.8b. To have a more complete view of all the cases accounted for in the analysis, more light-curves and the relative best-fit models reported in Fig. A.1 for 8 burst included "PL" subsample and in Fig. A.2 for all the 15 cases included in the "BPL" subsample.

---

[2] The cumulative distribution function (CDF) of a variable x, evaluated at x^*, is the probability that x will take a value less than or equal to x^*: $\mathrm{CDF}_x(x^*) = \mathcal{P}(x \leq x^*)$.

In Fig. 3.6, a graphic representation summarizing the subsamples selected up to this stage of the analysis is given.

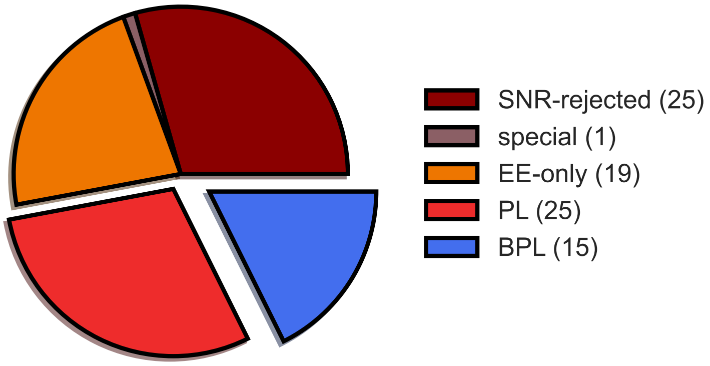

Figure 3.6: Pie chart showing all the subsamples determined up to this stage of the analysis, starting from the 85 bursts included in the initial sample. The subsamples relative to the 45 uninformative cases are the same as in Fig. 3.5, but the 40 cases which were formerly identified as the "LC fit" sample, after the light-curve fitting were divided between the "PL" subsample (25 bursts, in red) and the "BPL" subsample (15 bursts, in blue).

The results of the fit are quoted in Tab. 3.2. For the bursts in which the BPL model was found to be an improvement with respect to the PL model, the break time $t_{\rm break}$, the value of the flux at the break time $F_{\rm break}$ and both time decay indices α_1 and α_2 were reported, together with the p-value that can be used as a reference of the significance of the improvement. For the cases in which the PL was enough to describe the behaviour of the flux time decay, instead, we reported just the time decay index and the normalization constant $F_{\rm pl,norm}$. For every case, the starting time of the fit t_0 is quoted too. The errors on $t_{\rm break}$ were extremely small ($<$1%), thus they are not reported in the table.

Two of the cases included in the "PL" subsample, show anyway a peculiar behaviour: these two bursts are GRB 050724 and GRB 131004A, depicted respectively in Fig. A.1e and Fig. A.1f. Both of them show some flaring activity in their afterglow, making it difficult to properly fit the light-curve with one of our two power-law models. Since flares are thought to be residual prompt emission signals, thus not due to the afterglow component, what was done for these cases was to discard the data in the time-range corresponding to the flare with the purpose of computing the fit only on the data not affected by the flare itself: in both cases, the behaviour of the flux time decay was well represented by a PL.

GRB name	z	t_0 (s)	α_1	α_2	$t_{\rm break}$ ($\times 10^3$ s)	$F_{\rm pl,norm/break}$ ($\times 10^{-12}$ erg cm^{-2} s^{-1})	χ^2	ν	p-value
050724(F)	0.254	370	0.93 ± 0.06	-	-	(1.63 ± 0.19)	23.9	10	1.0
061006	0.461	168	0.78 ± 0.05	-	-	(1.45 ± 0.13)	13.3	9	1.0
070724A	0.457	385	1.16 ± 0.10	-	-	(1.3 ± 0.3)	21.8	4	8.58×10^{-2}
070809	0.2187	126	0.50 ± 0.06	-	-	(1.7 ± 0.2)	43.0	14	1.14×10^{-3}
090426	2.609	120	0.95 ± 0.03	-	-	(2.85 ± 0.19)	40.9	25	7.57×10^{-3}
111117A	2.211	200	1.22 ± 0.07	-	-	$(5.4 \pm 0.6) \times 10^{-1}$	4.8	5	7.99×10^{-1}
120804A	1.05	150	1.08 ± 0.03	-	-	$(1.26 \pm 0.07) \times 10$	55.1	30	1.0
121226A	1.37	146	0.97 ± 0.05	-	-	(5.0 ± 0.5)	21.5	11	1.36×10^{-1}
131004A(F)	0.717	105	1.00 ± 0.06	-	-	(4.9 ± 0.7)	25.5	8	1.60×10^{-1}
140129B	0.43	400	1.29 ± 0.09	-	-	(5.9 ± 0.8)	24.0	15	1.52×10^{-2}
140930B	1.465	214	1.75 ± 0.10	-	-	(1.4 ± 0.2)	61.7	23	1.0
150423A	1.394	100	0.91 ± 0.06	-	-	(1.11 ± 0.13)	4.5	6	6.47×10^{-2}
150831A	1.18	200	1.07 ± 0.08	-	-	(0.71 ± 0.10)	2.2	4	1.0
160303A	1.01	600	0.68 ± 0.10	-	-	(0.76 ± 0.13)	15.2	5	2.90×10^{-1}
160525B	0.64	99	1.35 ± 0.10	-	-	(0.67 ± 0.14)	27.4	11	1.0
160821B	0.1619	300	1.33 ± 0.13	-	-	(2.0 ± 0.6)	16.2	3	7.94×10^{-1}
170728A	1.493	250	0.98 ± 0.07	-	-	(3.6 ± 0.4)	5.9	4	4.76×10^{-1}
180418A	1.56	3170	0.84 ± 0.04	-	-	(2.2 ± 0.15)	17.8	16	1.0
180727A	1.95	100	1.20 ± 0.09	-	-	(0.9 ± 0.2)	6.1	3	1.0
180805B	0.6612	479	1.16 ± 0.11	-	-	(1.3 ± 0.2)	16.3	8	1.0
191019A	0.248	3545	1.13 ± 0.13	-	-	(1.22 ± 0.13)	9.1	6	8.19×10^{-2}
200411A	0.82	400	0.84 ± 0.08	-	-	(2.0 ± 0.2)	18.7	9	1.0
200522A	0.5536	450	0.64 ± 0.08	-	-	(1.3 ± 0.2)	6.6	3	7.40×10^{-1}
210726A	0.37	500	0.56 ± 0.02	-	-	(1.41 ± 0.08)	2.5	7	9.90×10^{-1}
211023B	0.862	750	0.78 ± 0.06	-	-	(1.48 ± 0.15)	8.9	6	1.0
051221A	0.5464	314	0.65 ± 0.03	1.44 ± 0.08	6.16×10	$(5.5 \pm 0.4) \times 10^{-1}$	96.6	60	1.26×10^{-8}
060614	0.125	4000	0.06 ± 0.03	1.81 ± 0.03	4.45×10	(5.8 ± 0.2)	172.9	149	1.11×10^{-16}
061201	0.111	80	0.65 ± 0.06	2.12 ± 0.10	3.00	$(3.9 \pm 0.5) \times 10$	29.3	24	2.50×10^{-9}
070714B	0.923	300	0.65 ± 0.12	2.11 ± 0.10	2.13	$(1.8 \pm 0.2) \times 10$	44.8	25	2.43×10^{-6}
090510	0.903	100	0.66 ± 0.03	2.28 ± 0.06	1.67	$(7.6 \pm 0.4) \times 10$	93.4	99	1.11×10^{-16}
110402A	0.854	593	0.48 ± 0.06	2.25 ± 0.15	8.43	(2.0 ± 0.2)	13.7	15	6.11×10^{-6}
130603B	0.3568	70	0.38 ± 0.03	1.69 ± 0.06	2.90	$(3.3 \pm 0.2) \times 10$	128.8	69	1.11×10^{-16}
140903A	0.3529	200	0.15 ± 0.03	1.25 ± 0.05	9.65	(9.7 ± 0.5)	28.2	34	8.55×10^{-15}
150424A	0.3	453	0.76 ± 0.02	2.4 ± 0.3	2.03×10	$(3.9 \pm 0.3) \times 10^{-1}$	23.3	32	1.24×10^{-6}
151229A	0.63	90	0.26 ± 0.19	0.96 ± 0.04	3.47×10^{-1}	$(2.8 \pm 0.9) \times 10^2$	73.1	70	9.51×10^{-7}
161001A	0.67	207	0.75 ± 0.05	1.37 ± 0.05	3.53	$(4.9 \pm 0.4) \times 10$	57.3	45	1.45×10^{-5}
170728B	1.272	400	0.53 ± 0.03	1.34 ± 0.02	2.53	$(2.1 \pm 0.1) \times 10^2$	213.6	193	1.11×10^{-16}
180618A	0.52	80	0.11 ± 0.40	1.77 ± 0.04	1.27×10^{-1}	(1.8 ± 0.2)	130.4	97	2.98×10^{-11}
210323A	0.733	800	0.50 ± 0.06	3.4 ± 0.3	1.32×10	(4.2 ± 0.4)	10.4	10	1.22×10^{-5}
211211A	0.0763	3400	-0.12 ± 0.18	2.07 ± 0.08	7.97	$(5.5 \pm 0.6) \times 10$	72.9	47	2.39×10^{-10}

(F) In these cases, a flare was excluded to allow a better fit of the afterglow.

Table 3.2: Results of the fit performed with the simple power-law (PL) model and with the broken power-law model (BPL) for all the 40 SGRBS for which it was possible to study the light-curve time evolution ("LC fit" sample). The 15 bursts for which the addition of a break resulted statistically significant (*below*) are the ones for which the F-test returned an associated p-value below the 4-σ threshold (corresponding to 6.2×10^{-5}): these define the "BPL" subsample. The other 25 bursts (*above*) are instead classified as "PL" subsample.

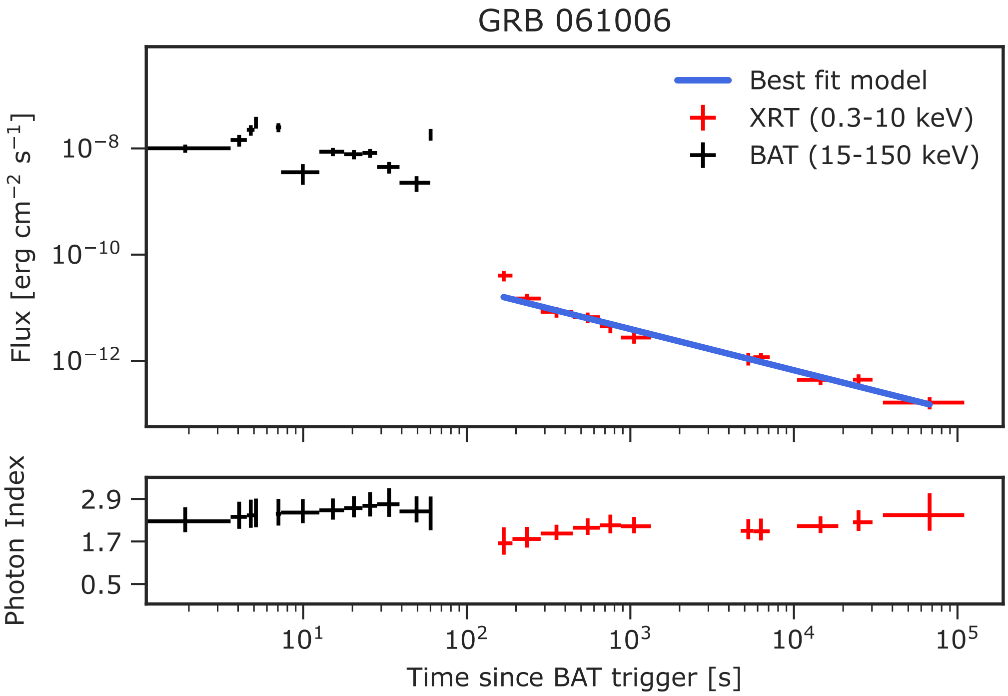

(a)

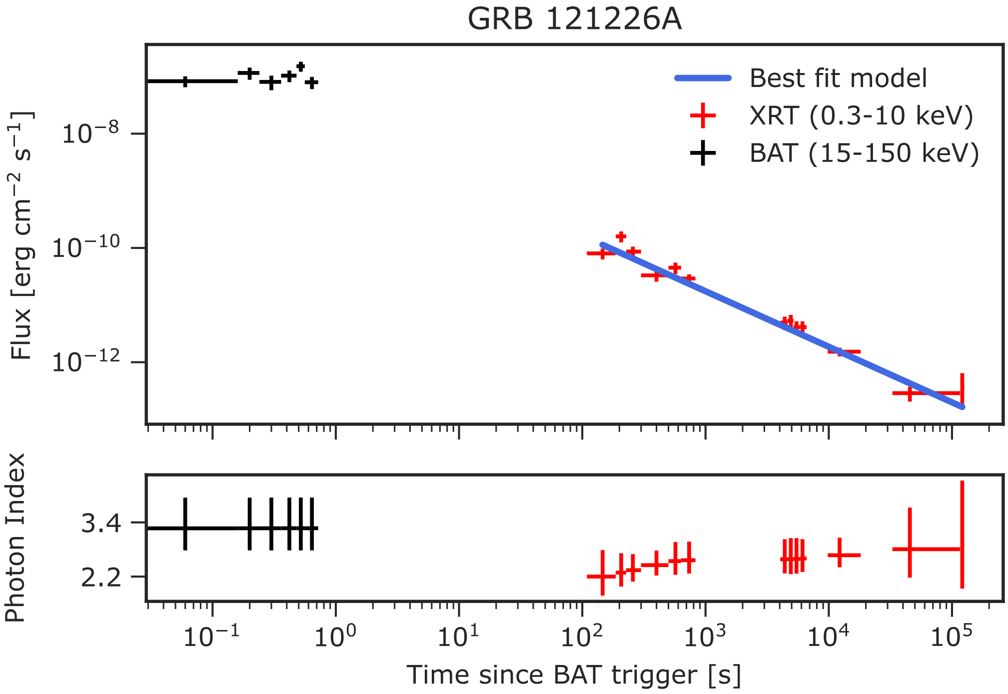

(b)

Figure 3.7: Example of two light-curves for which the XRT data (in red) were accurately reproduced by a simple power-law fit ("PL" subsample). The best fit (PL) model is represented by the blue line. BAT data (in black) are included as a reference.

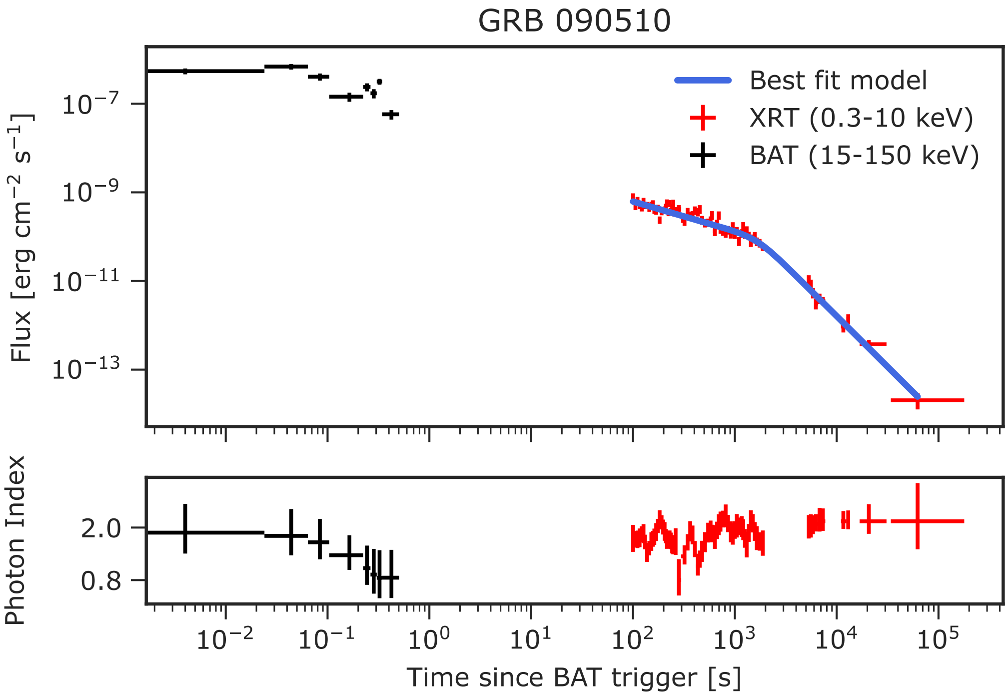

(a)

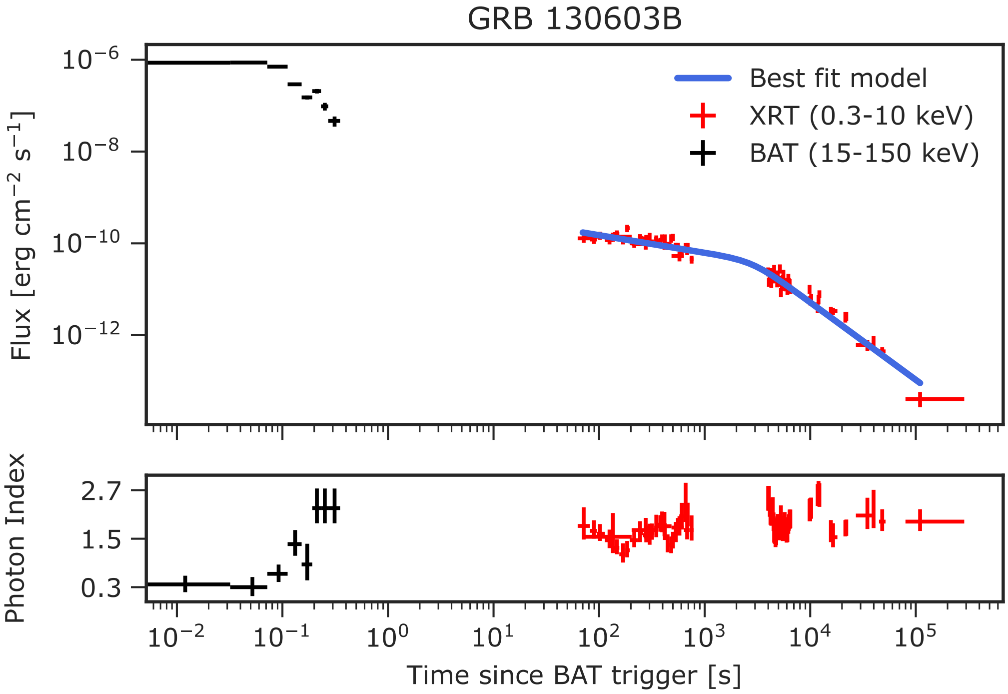

(b)

Figure 3.8: Light-curve for two cases for which the broken power-law model resulted more statistically significant with respect to the simple power-law ("BPL" subsample) in fitting the XRT data (in red). The best fit (BPL) model is represented by the blue line. BAT data (in black) are included as a reference.

In Fig. 3.9 we report the values of the time decay indices α_1 and α_2 derived from the fit for the cases included in the "BPL" subsample. A steepening after the break is clearly observed in all the cases, since $\alpha_2 > \alpha_1$ always. On the graph, the threshold $\alpha_1 = 0.75$, derived in Section 1.3.4 in the context of the standard synchrotron model for the afterglow, is represented as a green vertical line: this number is important because, if α_1 is lower than this value, alternative models are needed to explain the shallow phase. This is were the plateau interpretation comes into play, as explained in next section.

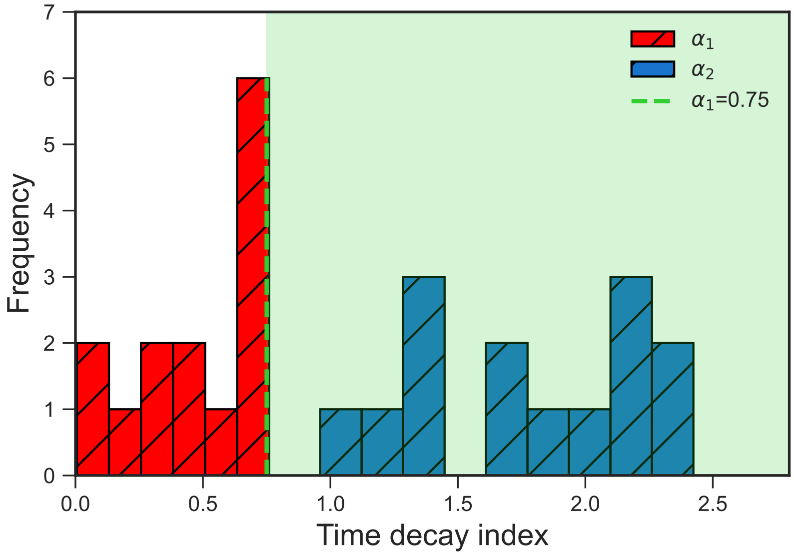

Figure 3.9: Histogram showing the time decay indices before (α_1, in red) and after the break (α_2, in blue) for all the 15 bursts for which the fit with the BPL model resulted in being statistically significant. The green line indicates the threshold $\alpha_1 = 0.75$, derived in Section 3.4, above which the standard afterglow model interpretation of the shallow phase works (green shaded region): it is clear that all the values found for α_1 cannot be explained with this model, suggesting the need for an alternative interpretation.

3.4 Plateau identification

The 15 cases which were included in the "BPL" subsample in the previous step of the analysis cannot be defined yet as SGRBs in which a plateau is present: indeed, the broken power-law behaviour is a condition that is necessary, but not sufficient, to define a plateau. As previously explained in Section 1.3.4, the two main properties to be verified when looking for the presence of a plateau are: **A)** time decay index α_1 that is flat enough to make the standard fireball model interpretation not feasible; **B)** negligible spectral evolution between the plateau and post-plateau phase. While the verification of the value of α_1 obtained by the fit was straightforward, to check the absence of spectral variability was a more complex task. The procedure followed to verify both these condition for all the bursts composing the "BPL" subsample is outlined in the following.

A) Checking the value of the shallow phase index

The value of α_1, the time decay index during the shallow phase, is fundamental to understand if the shallow phase of the afterglow can be interpreted or not using the standard synchrotron model (provided for in Section 1.3.2). For this reasons, the value of α_1 was checked for all the 15 cases for which the break was found to be statistically significant: as it is evident from Fig. 3.9, all these values (reported in Tab. 3.2), resulted in being either below or at most straddling the threshold $\alpha_1 < 0.75$ (see Section 1.3.4 for derivation), rendering them all good candidates for the presence of a plateau.

B) Verifying the spectral variability

Another important condition to be verified for a power-law break to be classified as a good plateau candidate is the absence of strong spectral variability before and after the break itself. Considering the 15 cases composing the "BPL" subsample, we checked the presence of any spectral evolution across the break: this is indeed the behaviour we would expect in the case the brake was produced by synchrotron mechanisms, like the crossing of a characteristic frequency (see Sec. 1.3.2), and this is the hypothesis that has to be ruled out in order to consider the "plateau" interpretation. Even though all the photon index sub-plots reported in Fig. A.2 make evident that the photon index Γ varies significantly with time in most of the cases, it is important to recall that the values of Γ obtained from the Burst Analyser tool are not measured directly from the integrate spectra, but derived by the algorithm through the procedure described in Section 2.2: this means that they have to be considered carefully since they may be affected by strong uncertainties.

To obviate to this problem, one solution is to extract two spectra, the first during the full duration of the shallow phase and the second during the post-break phase: by assuming a simple power-law spectral model, this allows to derive the two best fit photon indices. To do this, the spectra repository on the UKSSDC website was largely employed (see Section 2.2) and in particular exploiting the *Swift*-XRT data analysis algorithm dedicated to spectral extraction. The advantage of this tool lies in the possibility of building times sliced spectra, which are spectra integrated over time intervals larger than typical temporal bins, following the procedure outlined in Arnaud et al. (2023): this allows to obtain a robust photon index measure both before and after the break.

By defining two time ranges for each burst, Δt_A (covering the shallow phase and lasting right before t_{break}) and Δt_B (covering the post-break phase and starting right after t_{break}), it was possible to provide the algorithm with the "time-slices" in which the spectral extraction had to be computed. In this way, it was possible to extract the X-ray spectrum in both time ranges Δt_A and Δt_B, obtaining two values of the photon index, Γ_A and Γ_B respectively. These two values were then compared in order to understand if they were compatible inside the confidence regions defined by their errors. Results for each case are reported in Tab. 3.3, in which both the time ranges Δt_A and Δt_B over which the spectral extraction was performed and the corresponding photon indices Γ_A and Γ_B are listed, together with the break time t_{break}. Inspecting Fig. 3.10, it is evident how in all the 15 cases, the values of Γ_A and Γ_B are consistent within the confidence regions defined by their errors apart from the case of GRB 061201, which is anyway compatible within 2σ. We can then confidently conclude that there is no clear evidence of spectral variability: thus, all the 15 bursts composing the "BPL" subsample were included in the so-called "plateau" subsample.

GRB name	t_{break} (s)	Δt_A(s)	Γ_A	Δt_B	Γ_B
211211A	7970	$3000 \div 5000$	$1.54^{+0.13}_{-0.11}$	$15000 \div 23000$	$1.53^{+0.13}_{-0.11}$
210323A*	13187	$800 \div 12000$	$1.36^{+0.27}_{-0.23}$	$14000 \div 55000$	$2.9^{+1.9}_{-1.5}$
170728B	2536	$400 \div 2400$	$1.76^{+0.12}_{-0.11}$	$2600 \div 21000$	$1.84^{+0.09}_{-0.09}$
161001A	2678	$207 \div 2500$	$1.85^{+0.22}_{-0.21}$	$2800 \div 12000$	$2.10^{+0.40}_{-0.30}$
15129A	347	$166 \div 317$	$1.60^{+0.30}_{-0.30}$	$377 \div 743$	$1.90^{+0.30}_{-0.30}$
140903A	9653	$250 \div 9400$	$1.65^{+0.20}_{-0.20}$	$9700 \div 20000$	$1.40^{+0.24}_{-0.20}$
090510	1673	$90 \div 1600$	$1.58^{+0.13}_{-0.09}$	$1700 \div 70000$	$1.93^{+0.26}_{-0.25}$
070714B	2125	$400 \div 2050$	$1.90^{+0.17}_{-0.16}$	$2200 \div 32000$	$1.78^{+0.39}_{-0.17}$
061201*	2985	$80 \div 2900$	$1.29^{+0.18}_{-0.16}$	$3050 \div 11000$	$1.8^{+0.4}_{-0.3}$
060614	44547	$3000 \div 44500$	$1.72^{+0.11}_{-0.05}$	$44650 \div 150000$	$1.84^{+0.13}_{-0.12}$
051221A	57870	$16000 \div 57600$	$1.99^{+0.25}_{-0.24}$	$58000 \div 150000$	$2.20^{+0.40}_{-0.30}$
130603B	2902	$50 \div 2800$	$2.50^{+0.60}_{-0.40}$	$3000 \div 7000$	$1.98^{+0.18}_{-0.17}$
110402A	6810	$1000 \div 6700$	$2.03^{+0.31}_{-0.28}$	$6900 \div 14000$	$2.15^{+0.61}_{-0.29}$
150424A*	210105	$10000 \div 135000$	$1.73^{+0.21}_{-0.16}$	$218000 \div 443000$	$1.7^{+0.9}_{-0.7}$
180618A	127	$84 \div 120$	$1.81^{+0.18}_{-0.17}$	$135 \div 235$	$1.98^{+0.14}_{-0.14}$

Table 3.3: Results of the spectral analysis for the 15 cases included in the "BPL" subsample.

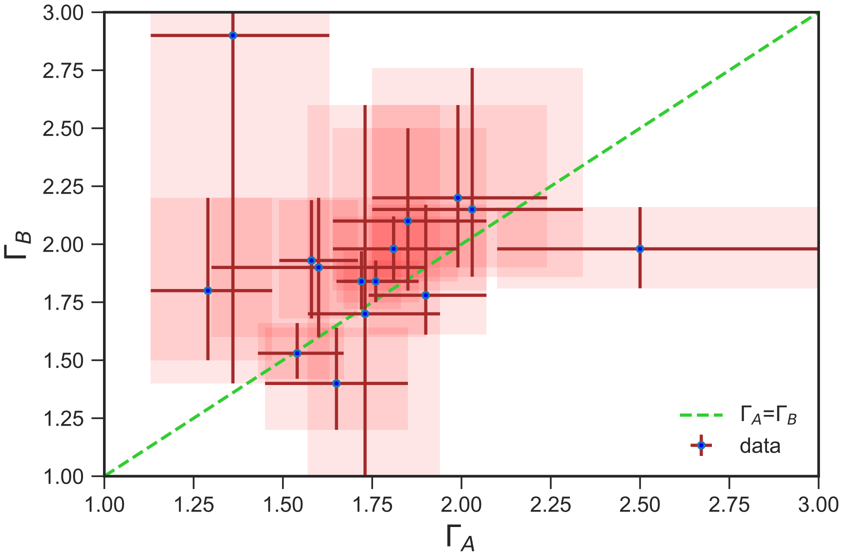

Figure 3.10: Graphic representation of the values of the photon indices Γ_A (x-axis) and Γ_B (y-axis) for the 15 bursts included in the "plateau" subsample (see Tab. 3.3). The green dashed line represents the place of points for which $\Gamma_A = \Gamma_B$. For each pair of Γ values (blue dots), the uncertainties are reported (red lines) and the shaded patches represent the confidence regions of each pair: when the patch intercepts the green line, it means that the two values are consistent within 1σ.

3.5 Discussion and "plateau" fraction

Here we give a summary of the results of the three main steps of the analysis performed on the 85 SGRBs composing the initial sample.

- Inspecting the signal to noise ratios of the light-curves, it was possible to individuate 25 cases which were too poorly sampled to be considered for the light-curve fitting procedure: these cases were classified as "SNR-rejected". Inspecting the redshift distribution Fig. 3.11, one can conclude that no evident link between the quality of the data and the distance of the event applies. 19 cases were found to portray only the EE phase or, at most, the early afterglow phase, but with too few data to draw conclusion about its behaviour: these defined the "EE-only" subsample. One last case, GRB 150101B, was labeled as "special case" since consisted only in late time data, preventing us to gain any information about the early afterglow light-curve in which a plateau could show up. To understand if the low value of the SNR of the cases included in the "SNR-rejected" subsample was connected to the distance at which these events happened, we compared the redshift distribution of both the "SNR-rejected" subsample and the "EE-only" subsample with the one of the initial sample (Fig. 3.11). For what concerns the SNR-rejected, apart from two cases, all the others have values of the redshift smaller than 1: the fact that no clear afterglow data are present suggests that these are intrinsically faint bursts.

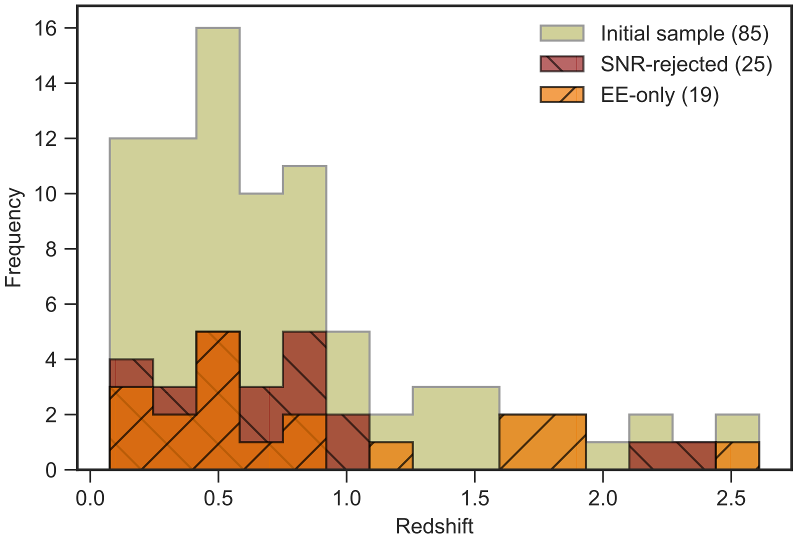

Figure 3.11: Comparison between the redshift distribution of the original sample (85 bursts, in green), of the "EE-only" subsample (19 bursts, in orange and of the "SNR-rejected" subsample (25 bursts, in brown). It is clear that there is no evident connection between the distance from us and the quality of the data detected by *Swift*-XRT.

- The 40 cases which were not cast aside in the first step, were subject of the light-curve fitting analysis ("LC fit" sample): comparing the results of a PL fit and a BPL fit through an F-test, it was possible to define 25 cases for which the simple power-law model reproduced accurately the data ("PL" subsample) and 15 burst for which the introduction of an additional break led to a significative improvement in modeling the afterglow evolution ("BPL" subsample). In Fig. 3.12 redshift distribution of the cases included in the initial sample is compared with those relative to the "PL" and "BPL" subsample. It is in interesting to notice that the "LC fit" sample cases are located in average close to us, at low redshift: this can be be explained since, for the same value of intrinsic luminosity, the further a GRB is located the fainter it will appear, and so the more difficult to study its afterglow morphology.

The same can be said for the "plateau" subsample cases, but is is also evident how they do not show a peculiar distribution with respect to the overall "LC fit" sample, suggesting the presence of a break is not correlated to the distance of the event.

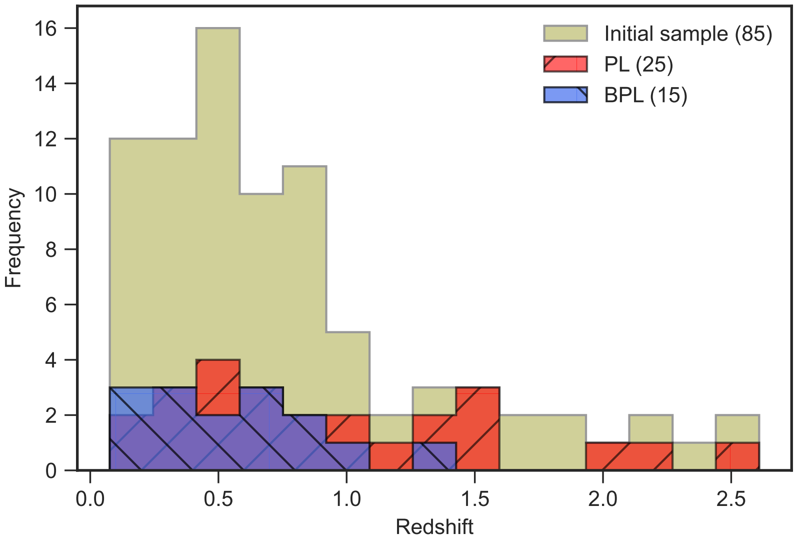

Figure 3.12: Histogram showing the redshift distribution of the initial sample (85 bursts, in green), the "PL" sample (15 burst, in red) and the "BPL" subsample (15 bursts, in azure).

- Eventually, the 15 cases included in the "BPL" subsample were further inspected in order to understand if they fulfilled the requirements to be considered as good "plateau" candidates, namely the value of the first time decay index α_1 and the absence of sharp spectral variability across the break. All the 15 bursts resulted in satisfying these conditions and were then labeled as the "plateau" subsample.

To further characterize the 15 cases selected as good plateau candidates, in Fig. 3.13 the distribution of $t_{\rm break}$ is reported. It is evident how the majority of the burst appears to show a break in the time range between 10^3 and 10^5 seconds (meaning the first hours following the burst trigger) but three cases catch the eye since they are the outliers of the distribution: as one can inspect looking at Tab. 3.2 GRB 151229A and GRB 180618A show a value of $t_{\rm break}$ at least one order of magnitude lower than all the others, while GRB 151204A exhibits a break at very late times ($\gtrsim 10^5$ s). A deeper analysis of these cases is carried out in Chapter 4.

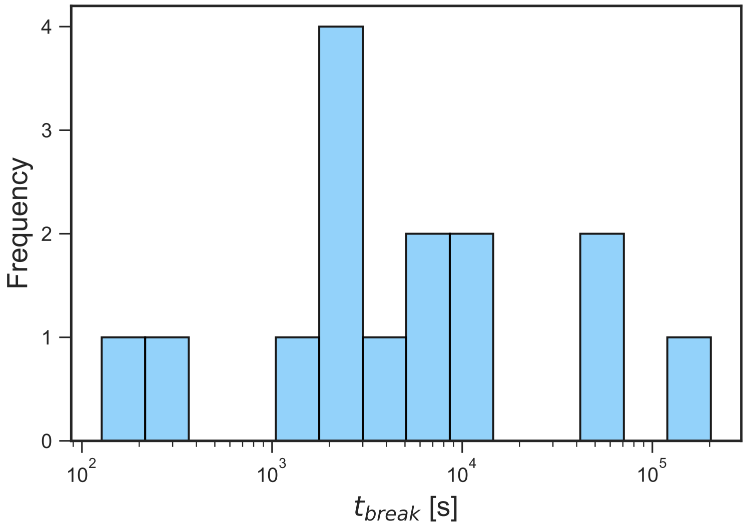

Figure 3.13: Histogram showing the break time (t_{break}) distribution of the 15 cases showing a plateau (logarithmic scale is used for time axis).

Another interesting quantity that is used to characterize GRBs is E_{iso}, which corresponds to the isotropic equivalent total energy emitted by the burst. The emitted energy is conventionally written as $E = E_{\text{iso}}(\Omega/4\pi)$, where Ω represents the solid angle within which the emission takes place: in case the emission is isotropic, then the emitted energy $E = E_{\text{iso}}$. Values of E_{iso} can be extremely high in the case of GRBs ($\gg 10^{52}$ erg), but it is important to recall that, as previously explained in Section 1.3.3, radiation is likely to be strongly beamed and this reduces significantly the energy requirement.

However, the derivation of E_{iso} is not straightforward: indeed, to compute this value one should measure the spectrum over a wide energy range in order to capture the distinctive peak energy of the GRB prompt emission. Usually, the Band spectrum given by Eq. 1.4 is assumed but, as explained in Section 1.3.1, no universal spectral model exists to reproduce GRB prompt emission: unfortunately, depending on the assumed model, the values of E_{iso} can change significantly.

The challenge of covering a large energy band (e.g, the *Swift*-BAT covers "only" the 15-150 keV energy range) is the reason why it was not possible to recover a value of E_{iso} for all the 85 SGRBs included in our sample. In Tab. A.1, we report the values of E_{iso} for the 42 burst for which it was possible to find this information in the literature: the large majority of them is taken from one of the most complete GRB catalogues, the Konus-Wind (KW) catalogue (Tsvetkova, Frederiks, Golenetskii, et al., 2017; Tsvetkova, Frederiks, Svinkin, et al., 2021), since KW covers an extremely large energy band (20 keV– 20 MeV). In Fig. 3.14 the $E_{\rm iso}$ distribution relative to these cases is compared with the distribution for all the 15 cases included in the "plateau" subsample. Values range from a minimum of 4×10^{49} erg to a maximum of 9×10^{52} erg. From these distributions, it can be seen that the cases for which it was possible to prove the presence of a plateau do not group around either high or low values of $E_{\rm iso}$, but instead show an essentially uniform distribution.

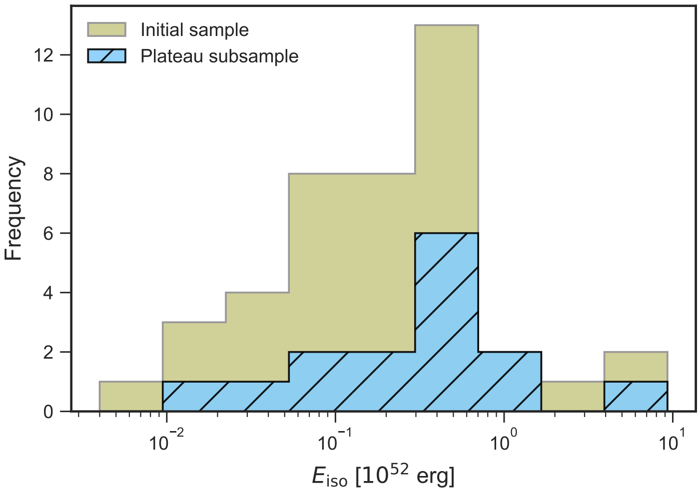

Figure 3.14: $E_{\rm iso}$ distribution of the bursts included in the "plateau" subsample (in blue) compared with the initial sample (in brown). We were able to find the value for $E_{\rm iso}$ only for 42 cases out of 85: these values are quoted in Tab. A.1. $E_{\rm iso}$ axis is in logarithmic scale.

In conclusion, we assumed two possible scenarios to compute the "plateau" fraction $f_{\rm plateau}$. The first scenario consists in computing this fraction taking into account only the 40 cases for which it was possible to perform the fit (the "LC fit" sample): in this way, the 15 bursts included in the "plateau" subsample correspond to a "plateau" fraction $f^{\rm max}_{\rm plateau} = 0.375$ (Fig. 3.15a). The second scenario consists in considering also the 45 cases excluded from the analysis after being classified as "uninformative": indeed, even though for these bursts it was not possible to study the afterglow morphology for the reasons explained in Section 3.2, this does not conclusively exclude the possible presence of a plateau phase in their afterglow. Thus, by assuming the plateau is absent in all these 45 cases, one can derive a minimum, more conservative value for the "plateau" fraction, corresponding to $f^{\rm min}_{\rm plateau} = 0.176$ (Fig. 3.15b). The importance of the defined range for the "plateau" fraction, namely $0.176 < f_{\rm plateau} < 0.375$, will be discussed in Chapter 6.

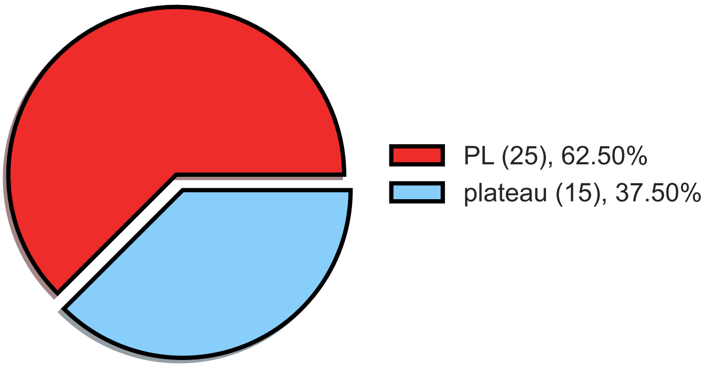

(a)

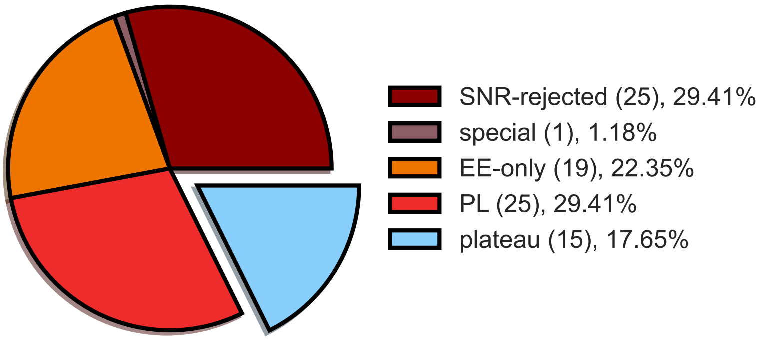

(b)

Figure 3.15: **(a)** Pie chart showing the "plateau" fraction $f_{\text{plateau}}^{\text{max}} = 0.375$ derived considering the 15 cases included in the "plateau" subsample (azure) with respect to the 40 cases for which it was possible to perform the light-curve fitting. **(b)** Same as before, but this time the "plateau" fraction is computed assuming that plateau is absent in all the 40 cases classified as "uninformative": in this way, the "plateau" subsample corresponds to $f_{\text{plateau}}^{\text{min}} = 0.176$. This defines a range for the "plateau" fraction, namely $0.176 < f_{\text{plateau}} < 0.375$.

Chapter 4

Testing the magnetar model

In this chapter, the results obtained from the light-curve analysis are interpreted within the magnetar model framework. However, to compare data with the model, we need to compute the intrinsic luminosity of the event: the procedure to build a rest frame luminosity light-curve starting from an observed flux light-curve is outlined in Section 4.1. In Section 4.2 the magnetar model fit is performed one the luminosity light-curves of the 15 SGRB included in the "plateau" subsample, in order to derive an estimate for the two main parameter characterizing a magnetar. Eventually, in Section 4.3 the 19 bursts included in the "EE-only" subsample are reconsidered under the assumption that the magnetar model is valid: this allows to confidently exclude the presence of a magnetar in some of them, and we use these values to provide a final "magnetar" fraction in Section 4.4. This fraction will be fundamental for the astrophysical implications presented in Chapter 5.

4.1 Building the luminosity light-curves

In order to convert the observed fluxes into luminosities, we must take into account all cosmological effects. Not only the luminosity distance will have to be used, but we must correct fluxes according to the K-correction, which means accounting for the frequency redshift of the received radiation relative to when it was emitted, due to Universe expansion (Bloom et al., 2001; Kovács et al., 2011).

Detectors usually measure fluence, which is an energy per unit area. The bolometric fluence S_{bol} is connected to the bolometric energy E_{bol} through the relation:

$$E_{bol} = \frac{4\pi D_L(z)^2}{1+z} \times S_{bol}, \tag{4.1}$$

where z is the redshift of the source while $D_L(z)$ is the luminosity distance (calculated assuming a standard ΛCDM cosmology with $H_0 = 67.4$ km s^{-1} Mpc^{-1}, $T_{\rm CBM,0} = 2.726$ K and $\Omega_0 = 0.315$, N. Aghanim et al., 2020). However, it is almost impossible to detect S_{bol}, since detectors usually have a finite bandpass between the energies e_1 and e_2. This means that what we obtain from the detector is the so called bandpass fluence:

$$S_{[e_1,e_2]} = \int_{e_1}^{e_2} \Phi(E)dE, \tag{4.2}$$

where $\Phi(E)$ is the best fit spectral model of the source emission.

In general, our aim is to measure the radiated energy in a given comoving bandpass between two arbitrary energies E_1 and E_2. This energy can be expressed as a function of the fluence through the following relation:

$$E_{[E_1,E_2]} = \frac{4\pi D_L(z)^2}{1+z} \times S_{[E_1/(1+z),\, E_2/(1+z)]}, \tag{4.3}$$

where the redshifted comoving energy range $[E_1/(1+z),\, E_2/(1+z)]$ is in general different from the detector bandpass range $[e_1, e_2]$. If we want to rewrite this equation as a function of the detector bandpass fluence, we will have to introduce an additional factor:

$$E_{[E_1,E_2]} = S_{[e_1,e_2]} \times \frac{4\pi D_L(z)^2}{1+z} \times K[e_1,\, e_2,\, E_1,\, E_2,\, z,\, \Phi(E)]. \tag{4.4}$$

This factor $K[e_1,\, e_2,\, E_1,\, E_2,\, z,\, \Phi(E)]$ is the cosmological K-correction and takes into account both the bandpass effects and the cosmological redshift effect. The K-correction can be computed through the following relation:

$$K = K[e_1,\, e_2,\, E_1,\, E_2,\, z,\, \Phi(E)] = \frac{\int_{E_1/(1+z)}^{E_2/(1+z)} \Phi(E)dE}{\int_{e_1}^{e_2} \Phi(E)dE}, \tag{4.5}$$

where $[e_1,\, e_2]$ is the detector bandpass range, $[E_1,\, E_2]$ is the corresponding energy range in the source rest frame, z is the GRB redshift and $\Phi(E)$ is the spectral shape of the emission. Note that K-correction is equal to 1 when the bandpass energy range and the redshifted comoving energy range correspond ($E_1 = e_1(1+z)$ and $E_2 = e_2(1+z)$).

Once the K-correction is computed, it can be used to calculate some comoving quantities which result to be very useful in the description and classification of GRBs, e.g. the isotropic equivalent luminosity $L_{\rm iso}$ (i.e., the luminosity computed assuming the source is emitting isotropically). However, overwhelming observational evidence indicates that GRB outflows are characterized by a conical geometry (see Section 1.3.3): the result found above must thus be corrected for the effects of relativistic beaming (Frail et al., 2001). Indeed, a conical jet with an half opening angle θ_j will not emit isotropically in all directions but, due to the effect of relativistic beaming, only within the solid angle subtended by its surface, i.e. within the fraction of a sphere given by the so-called "beaming fraction":

$$f_b = (1 - \cos\theta_j). \tag{4.6}$$

Notice that when $\theta_j \ll 1$, then $f_b \simeq \theta_j^2/2$. Knowing the value of θ_j, one can properly correct the value of $L_{\rm iso}$ by multiplying it by the beaming fraction:

$$L = L_{\rm iso} \times (1 - \cos\theta_j). \tag{4.7}$$

With all these provisions, the bolometric luminosity of GRB X-ray afterglow can be expresses as:

$$L(t) = 4\pi D_L^2(z) \times F_X(E_1, E_2, t) \times K_{[0.3-30\,\rm keV]} \times (1 - \cos\theta_j), \tag{4.8}$$

where F_X is the observed X-ray flux (in the $0.3 - 10$ keV band) as a function of time. Note that the K-correction for our purposes was computed from Eq. 4.5 using $e_1 = 0.3$ keV and $e_2 = 10$ keV as bandpass energy range, since this is the working bandpass of the XRT, while for the rest frame band the choice was to use $E_1 = 0.3$ keV and $E_2 = 30$ keV, since this is the energetic band in which the bulk of the X-ray afterglow emission is expected to lie. To build the comoving frame luminosity light-curve, it is also necessary to correct the observed time $t_{\rm obs}$ for the cosmological redshift: the rest frame time will be expressed as:

$$t_{\rm rest} = \frac{t_{\rm obs}}{(1+z)}. \tag{4.9}$$

As it is manifest from Eq. 4.8, the conversion to luminosity light-curves requires the knowledge of the jet half opening angle θ_j, but measuring it is a challenging task: indeed, long multi-wavelength afterglow monitoring is required in order to measure the jet break time $t_{\rm jet}$ (see Section 1.3.3). Investigating the literature, we were able to find the values reported in Tab. 4.1. The fact that different works reported different θ_j for the same burst highlights the strong dependence of this parameter on the method and on the model of surrounding medium which are assumed for its computation. In the cases in which no θ_j could be measured, we took the values presented in Zhu et al. (2023): some of them are labeled as "pseudo values" because for those GRBs the $t_{\rm jet}$ was not measured, but a "pseudo $t_{\rm jet}$" was derived from the three parameters $t_{{\rm jet},z} - E_{p,z} - E_{\rm iso}$ correlation (where $t_{{\rm jet},z}$ and $E_{p,z}$ are, respectively, the intrinsic values of jet break time and peak energy).

GRB	θ_j	$\delta\theta_{j+}$	$\delta\theta_{j-}$	Reference
051221A	6	2.1	1.9	Aksulu et al., 2022
060614	12.61	0.11	0.11	Zhu et al., 2023
061201	3.44	0.06	0.06	Zhu et al., 2023
070714B^p	8.59	0.92	0.69	Zhu et al., 2023
090510^p	2.29	0.11	0.11	Zhu et al., 2023
110402A	15.02	1.13	3.68	Zhang et al., 2015
130603B	6.3	1.7	5.1	Aksulu et al., 2022
140903A	4	5	1.6	Aksulu et al., 2022
150424A	4.3	2.1	1.5	Escorial et al., 2022
151229A	-	-	-	-
161001A	-	-	-	-
170728B	3.5	1.1	0.8	Escorial et al., 2022
180618A	-	-	-	-
210323A^p	2.86	0.23	0.23	Zhu et al., 2023
211211A	6.86	0.12	0.12	Zhu et al., 2023

^{p} In these cases, the angles found are pseudo values derived from three parameters $t_{\mathrm{jet},z} - E_{p,z} - E_{\mathrm{iso}}$ correlation.

Table 4.1: Jet opening angles values for the 15 GRBs included in the "plateau" subsample.

4.2 Derivation of magnetar parameters

At this stage of the work, after having taken into account the opening angle values quoted in Tab. 4.1, the observed flux afterglow light-curve for each of the 15 cases included in the "plateau" subsample was converted to rest frame luminosity light-curve using Eq. 4.8. In this way, it was possible to use the magnetar model introduced in Section 1.3.5 to fit these light-curves and derive two important magnetar parameters: the magnetic field strength B and the spin period P. For this purpose, the same model employed in the work of Stratta et al. (2018) and available on Giulia Stratta, Magnetar Model, (2018), GitHub repository[1] was adopted. In this model, the following assumptions regarding the magnetar properties are made:

– the magnetar is assumed to radiate its whole energy isotropically, $\theta_{\mathrm{NS}} = 90$ deg (if the magnetar emission was instead anisotropic, $\theta_{\mathrm{NS}} < 90$ deg,

---

[1] `https://github.com/gistratta/magnetar`

we would expect an increase of the magnetar parameters B and P by a factor $f_b^{-1/2}$);

- the direction of magnetar magnetic field B is perpendicular to the direction of magnetar angular momentum l, $\theta_{B-l} = 90$ deg (if the two axes were perfectly aligned, $\theta_{B-l} = 0$ deg, we would expect a decrease of the magnetar parameters B and P by a factor $\sqrt{2}$);
- the magnetar model coefficient $k' = 4\epsilon_e(d\ln t/d\ln T)$ (see Eq. 1.23) is kept < 1. We recall that ϵ_e is the electron energy fraction while the factor $(d\ln t/d\ln T)$ encloses the hydrodynamical evolution of the shock (Dall'Osso et al., 2011): the condition on k' implies $\epsilon_e < 0.5$;
- the magnetar model is tested for three fixed values of $\alpha = (3-n)/2$ (where n is the braking index introduced in Eq. 1.17), namely $\alpha = 0.1, 0.5, 0.9$ (see Stratta et al., 2018);
- the magnetar bolometric luminosity is approximated with the luminosity computed in the $0.3-30$ keV energy range;
- the total moment of inertia of the magnetar is approximated by (Lattime & Prakash, 2007):

$$I_{\rm NS} \simeq 0.237\, M_{\rm NS}\, R_{\rm NS}^2 (1 + 2.84\, \beta_{\rm NS} + 18.9\, \beta_{\rm NS}^4), \tag{4.10}$$

where $\beta_{\rm NS} = GM_{\rm NS}/(R_{\rm NS}c^2)$ is the NS compactness parameter.

Additionally, we note that we adopted fixed and standard values for the NS mass ($M_{\rm NS} = 1.4\,{\rm M}_\odot$) and radius ($R_{\rm NS} = 12$ km).

The fit was performed for each of the 15 bursts in the "plateau" subsample for all the three values of α. By doing this, it became clear that the results did not show any strong dependence on the α parameter, that was thus set to 0 (corresponding to a braking index $n = 3$). Moreover, since the light-curves of 9 out of 15 cases showed evidence of a steep decay phase preceding the plateau (see Section 1.3.4), for these bursts the fit was performed adding am early power-law component to the original magnetar model: in this way, the plateau was better constrained, which provided better estimates of the B- and P-values.

To start the fit, the starting time t_0 and the ending time $t_{\rm end}$ had to be provided (both values are referred to the burst's rest frame). The starting time t_0 was fixed at the beginning of the steep decay phase in the 9 bursts for which a steep decay was present, while for the other 7 cases it was fixed to coincide with the value of t_0 used for the light-curve fitting (and quoted in Tab. 3.2), corrected for the cosmological redshift (Eq. 4.9). The ending time t_{end} was instead taken as the time corresponding to the last data point, except for 3 cases (GRB 070714B, GRB 090510 and GRB 210323A) in which the luminosity at late times showed a significant decrease. This was done because this effect is likely a signature of the presence of a so called "jet break" (see Section 1.3.3). In the future development of the model, also this feature will be taken into account in order to reproduce the light-curve in the most accurate way.

The 12 bursts for which the fit allowed to derive good estimates of the magnetar parameters B and P were include in the final "magnetar" subsample. The best-fit results for these 12 bursts are reported in Tab. 4.2: together with the parameters B and P, the input parameters needed to define the model are reported too. The cases for which the power-law component was added to the model in order to account for the steep decay phase are labeled with an '$*$'.

GRB name	Input				Output			
	z	θ_j (deg)	$\log t_0$ (s)	$\log t_{\rm end}$ (s)	B (10^{14} G)	P (ms)	χ^2	ν
051221A*	0.5464	6	1.95	5.8	(34 ± 4)	(13.1 ± 0.9)	105.7	73
060614*	0.125	12.61	2	6.3	(46.7 ± 0.4)	(28.3 ± 0.4)	1317.4	488
070714B*	0.923	8.59	1.8	3.8	(175 ± 43)	(8.3 ± 1.0)	122.3	50
090510	0.903	2.29	1.72	3.5	(84 ± 13)	(4.89 ± 0.12)	117.2	63
110402A*	0.854	15.02	2.45	4.25	(126 ± 41)	(15.3 ± 1.9)	31.6	15
130603B	0.3568	6.3	1.712	5	(130 ± 9)	(14.5 ± 0.4)	132.5	70
140903A*	0.3529	4	1.89	5	(32 ± 3)	(12.1 ± 0.4)	52.3	35
150424A*	0.3	4.3	2.656	5.6	(29 ± 11)	(13 ± 4)	38.6	31
161001A*	0.67	5*	1.96	5.1	(99 ± 13)	(2.7 ± 0.9)	74.8	54
170728B	1.272	3.5	2.245	5.7	(24.0 ± 1.4)	(1.33 ± 0.07)	212.3	194
210323A*	0.733	2.86	1.99	4.3	(45.3 ± 0.9)	(9.1 ± 0.2)	43.7	16
211211A*	0.0763	6.86	1.9	5	(152 ± 41)	(31 ± 5)	1242.8	270

Table 4.2: Best-fit values of the magnetar parameters B and P for the 12 cases included in the "plateau" subsample for which the magnetar model fit of the luminosity light-curve resulted successful. The '$*$' labels the bursts for which a steep decay power-law component was added to the original magnetar model. Together with the fit results, for each case the 4 input parameters needed to run the model are listed too.

In Fig. 4.1 the rest frame luminosity light-curves for each of the 12 bursts included in the "magnetar" subsample are shown, together with the best-fit magnetar model. Notice that, in the case of GRB 150424 (Fig. 4.1h), even if the steep decay phase is present, the results reported in the plot and in Tab. 4.2 are the ones obtained with the original magnetar model: indeed, for this burst the addition of the power-law did not lead to a successful fit. This SGRB is characterized by the largest value of breaking time ($t_{\rm break} = 2.03 \times 10^5$ s), suggesting a particularly long plateau phase: a deeper analysis of this case will be carried out in the future development of this work.

For two bursts, it was not possible to constrain the values of B and P: these are GRB 151229A and GRB 180618A. Inspecting the values of $t_{\rm break}$ (Tab. 3.2) and the $t_{\rm break}$ distribution (Fig. 3.13) for these two cases, it is evident that they are the outliers of the distribution, their $t_{\rm break}$ being at least one order of magnitude smaller than all the other break times. This translates in a very short plateau phase, consisting of very few data, and this does not allow to model properly the plateau phase, preventing the derivation of a reliable estimate of B and P parameters.

In the case of GRB 061201, instead, the magnetar parameters resulted in being not in line with the values we would expect in standard magnetars: the magnetic field $B > 780 \times 10^{14}$ G is extremely large for a magnetar, while the long spin period $P > 37$ ms corresponds to an object that is rotating too slowly to be considered a magnetar. For these reasons, also this burst was not considered as a good magnetar candidate.

These three cases were thus cast aside and included in the so-called "failed magnetar" subsample.

One thing that has to be underlined is the fact that, under the assumption that the magnetar emission is isotropic ($\theta_{\rm NS} = 90$ deg), our model becomes independent on the value of θ_j we provide. Indeed, the derived magnetar parameters are related to the isotropic luminosity of the spinning down magnetar, $L_{\rm sd}^{\rm iso}$. However, assuming a jet geometry for the GRB, only a fraction f_b of the magnetar luminosity will be intercepted by the jet and will then contribute to the observed X-ray flux, namely:

$$L_{\rm sd}^{\rm jet} = f_b \, L_{\rm sd}^{\rm iso}. \tag{4.11}$$

On the other hand, as already seen in Section 4.1, in case of a jet structure, the beaming fraction f_b can be used to relate the equivalent isotropic quantities to the corresponding intrinsic value: this is valid also for the luminosity:

$$L = f_b \, L^{\rm iso}, \tag{4.12}$$

where L is the intrinsic, beaming-corrected afterglow luminosity, while $L^{\rm iso}$ is the isotropic equivalent afterglow luminosity derived directly from the observed flux. Under the assumption that all the luminosity observed during the afterglow plateau phase is generated by the fraction of the magnetar spin-down luminosity intercepted by the jet, namely $L = L_{\rm sd}^{\rm jet}$, combining Eq. 4.11 and Eq. 4.12 it is straightforward to derive:

$$L_{\rm sd}^{\rm iso} = L^{\rm iso}, \tag{4.13}$$

meaning that the isotropic equivalent luminosity L^{iso}, which can be easily derived from the observed flux, corresponds to the isotropic luminosity of the magnetar $L^{\mathrm{iso}}_{\mathrm{sd}}$, which is the physical quantity from which it is possible to estimate both the B field strength and the spin period P.

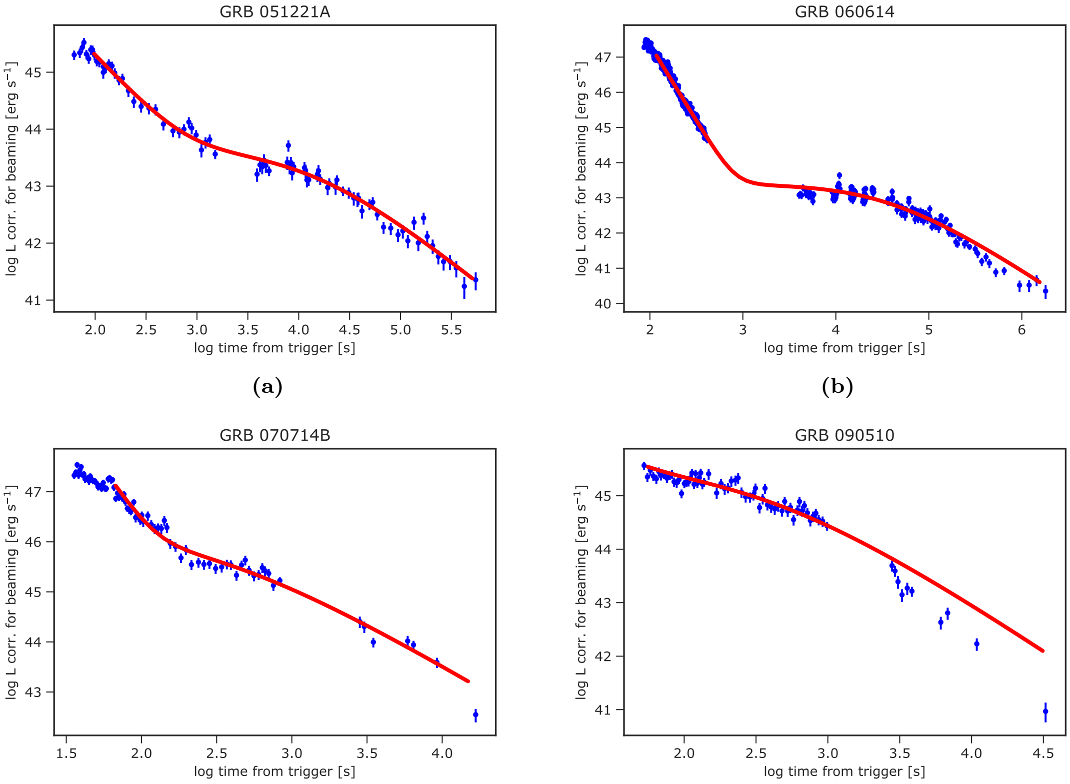

(a) **(b)**

(c) **(d)**

Figure 4.1: Results of the analysis of the rest frame, beaming corrected, luminosity light-curves (blue dots) in the energy range $0.3-30$ keV (rest frame) for the 12 cases included in the "plateau" subsample for which it was possible to derive the best-fit parameter B and P performing the fit with the magnetar model for the afterglow. The red line represents the best-fit magnetar model. Both axes are in logarithmic scale.

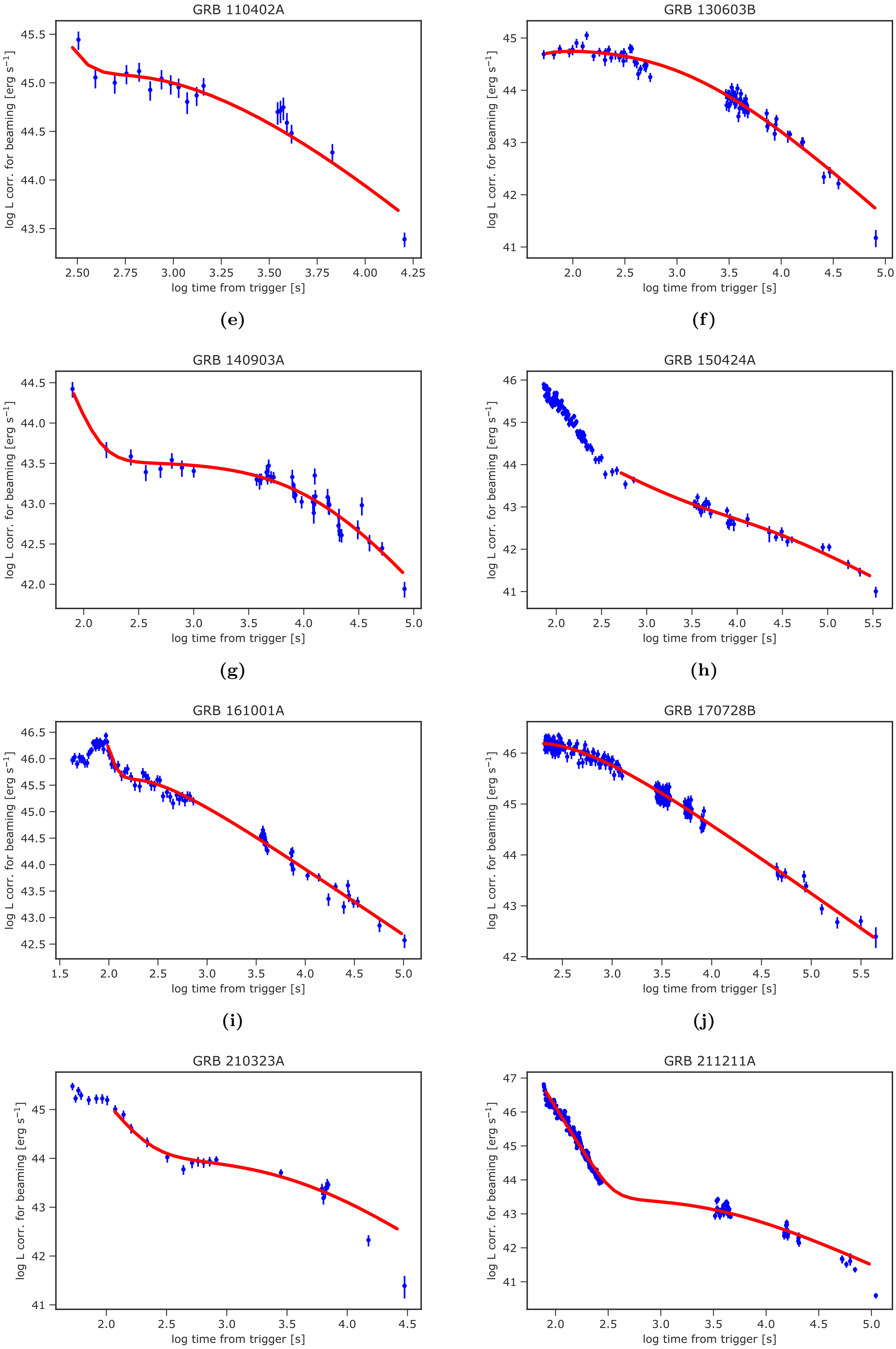

(e) **(f)**

(g) **(h)**

(i) **(j)**

(k) **(l)**

Figure 4.1: *-continued*

4.3 Considerations on the "EE-only" sample

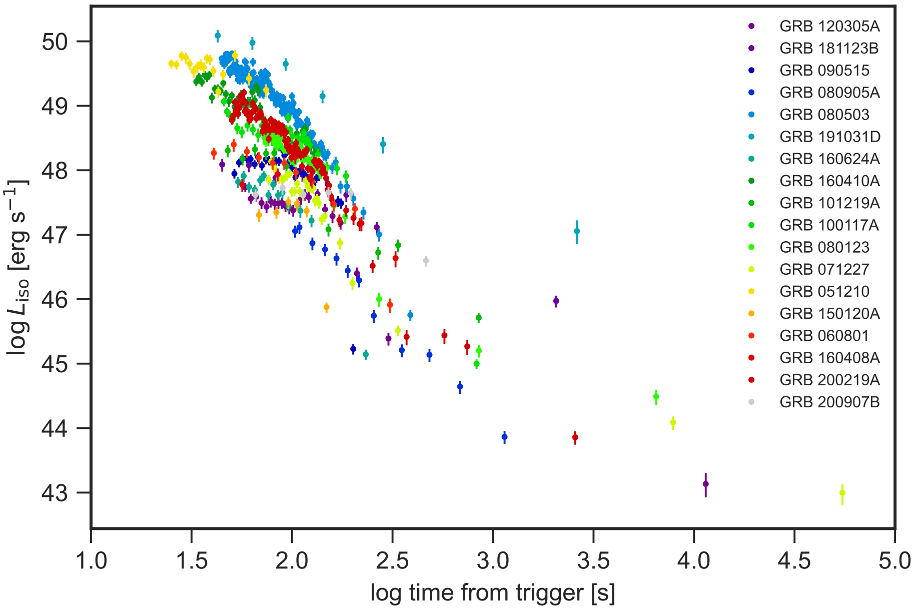

Figure 4.2: Isotropic luminosity light-curves (rest frame) for all the 19 bursts included in the "EE-only" subsample. It is clear how for the majority of these cases, the bulk of the emission is gathered around ~ 100 s and after that we observe a sharp drop (steep decay), as predicted for the EE phase. Both axes are in logarithmic scale.

In Section 3.2.2, 19 bursts were classified in the subsample named "EE-only" (see Tab. 3.1) since the data available in all these cases were either limited to the EE phase alone, or contained too few points of the afterglow emerging after the EE to obtain a significant fit. For these reasons, we excluded these cases from the light-curve fitting analysis, together with the SNR-rejected cases (25) and the "special case" of GRB 150101B. However, while the latter 26 bursts can be referred to as "inconclusive", since it was not possible to derive any information about the afterglow or a possible plateau phase, a further analysis was performed for the "EE-only" sample.

The rest frame, isotropic equivalent luminosity light-curves of the 19 EE-only bursts, derived through the procedure described in Section 4.1 with $\theta_j = 90$ deg, are shown in Fig. 4.2. Despite the lack of afterglow data, we used our prior knowledge of the properties of afterglow plateaus to verify whether the available EE data were consistent with the possible presence of an X-ray plateau, or if the latter could be confidently ruled out. In particular, we relied on two rather general considerations:

- no GRB plateau (neither in long nor in short bursts) was observed to last more than $\sim 10^5$ s, so we took this as a conservative estimate of the maximum plateau duration;
- because we expect millisecond-spinning NS to be formed in BNS mergers, we adopted 10^{50} erg as a conservative lower limit to the spin energy of a stable NS remnant, corresponding to a spin period ≈ 18 ms.

Starting from these two conservative assumptions, one can define two complementary criteria to identify the cases in which the presence of a magnetar can be confidently ruled out: the $L_{p,\mathrm{min}}$- and the κ'-criterion.

4.3.1 $L_{p,\mathrm{min}}$-criterion

Recalling that the spin energy of a NS is proportional to its spin period P_{ms} (expressed in ms) through the relation $E_{\mathrm{spin},i} = 3 \times 10^{52}\, P_{\mathrm{ms}}^{-2}$, one can use the standard approximation (Dall'Osso & Stella, 2022):

$$L_p(t) \sim \epsilon_{\mathrm{sd}} \frac{E_{\mathrm{spin},i}}{T_p} \left(1 + \frac{t}{T_p}\right)^{-2} \propto \frac{E_{\mathrm{spin},i}}{T_p}, \tag{4.14}$$

to link the initial plateau luminosity $L_p(t)$ to the plateau duration T_p and to the initial spin energy $E_{\mathrm{spin},i}$. Considering the above assumptions of a maximum spin period $\simeq 18$ ms (corresponding to a minimum spin energy) and of a maximum plateau duration $\sim 10^5$ s, Eq. 4.14 gives a conservative estimate of the minimum luminosity at which we expect to observe a magnetar plateau only when its luminosity $L_p(t)$ satisfies:

$$L_p(t) \gtrsim L_{p,\mathrm{th}} \sim 10^{45}\, \mathrm{erg\, s^{-1}} \tag{4.15}$$

Inspecting the isotropic luminosity light-curves for all the 19 bursts included in the "EE-only" subsample (represented singularly in Fig. A.3), we derived the luminosity $L_{p,\mathrm{min}}$ corresponding to the last detection: these values are reported in the second column of Tab. 4.3. Since Eq. 4.15 sets a lower threshold on the plateau luminosity, we could confidently exclude the presence of the plateau in the cases for which $L_{p,\mathrm{min}} \lesssim L_{p,\mathrm{th}}$. Indeed, if a plateau is not observed (and this is true by definition for "EE-only" cases) *and* the last detections are below $L_{p,\mathrm{th}}$, then the plateau is not present. On the other hand, the bursts which matched the criterion reported in Eq. 4.15 represent cases for which no conclusion could be drawn, since we lack data at lower luminosities where a plateau may still be present. Following this criterion, the presence of a plateau (and thus of a magnetar) could be excluded in 7 of the bursts in the "EE-only" sub-sample (bold values in third column of Tab. 4.3).

4.3.2 κ'-criterion

To confirm and cross-check the previous selection, we decided to follow the approach proposed in Dall'Osso, Stratta, et al. (2023). In this work, they compare the minimum luminosity of the prompt emission preceding the steep decay ($L_{\gamma,\rm min}$), and the initial NS spin down luminosity ($L_{\rm sd}$), finding they can be related through:

$$\kappa = L_{\gamma,\rm min}/L_{\rm sd} \approx 1.2 \times 10^5\, \epsilon\, P^{5/3} (R_6\, M_{1.4}^{2/3})^{-1}, \tag{4.16}$$

with ϵ the radiative efficiency (typically ~ 0.1) of the prompt emission, P the NS spin period in seconds, $R_6 = R_{\rm NS}/(10^6\,\rm cm)$, $M_{1.4} = M_{\rm NS}/(1.4\,\rm M_\odot)$. Note that, for given NS mass and radius, κ is function of the NS spin period alone. Thus, in the framework of the magnetar model, the assumed lower limit for the spin energy (corresponding to a period $P \approx 18$ ms) allows to derive an upper limit for this ratio, $\kappa \lesssim 10$.

It is important to stress that the value of $L_{\gamma,\rm min}$ refers to the prompt emission, for which beaming must be taken into account: the corresponding isotropic equivalent value can be compute through $L^{\rm iso}_{\gamma,\rm min} = L_{\gamma,\rm min} f_b^{-1}$, where we rescale it by the beaming fraction. Conversely, $L_{\rm sd}$ is an isotropic luminosity since it indicates the magnetar spin-down power. Taking this into account, one can derive from Eq. 4.16 a relation which depends only on isotropic luminosities:

$$\kappa' = \frac{L^{\rm iso}_{\gamma,\rm min}}{L_{\rm sd}} = \frac{L_{\gamma,\rm min}}{L_{\rm sd}} f_b^{-1} = \kappa f_b^{-1} \tag{4.17}$$

Note that all the 19 cases lack information about the jet opening angle θ_j (since no afterglow data are available). However, assuming a common average value for the beaming fraction $f_b = 0.01$ (a reasonable value for SGRBs, corresponding to a $\theta_j \sim 8$ deg), we conclude that the upper limit for κ corresponds to the threshold:

$$\kappa' \lesssim 10^3. \tag{4.18}$$

For each of the 19 "EE-only" light-curves, the ratio κ' was computed considering the value of the luminosity prior to the steep decay as $L^{\rm iso}_{\gamma,\rm min}$, while $L_{\rm sd}$ was approximated with the minimum detected luminosity, since $L_{p,\rm min} \gtrsim L_{\rm sd}$ by definition. These values are quoted in Tab. 4.3.

For 9 bursts, the value of κ' was found to exceed the threshold of Eq. 4.18 (bold values in fourth column of Tab. 4.3): these correspond to the 7 bursts singled out with the $L_{p,\rm min}$-criterion, and two additional cases, GRB 080503 and GRB 191031D.

GRB name	$\log L_{\gamma,\rm min}$	$\log L_{p,\rm min}$	$\log L^{\rm iso}_{\gamma,\rm min}/L_{p,\rm min}$
051210	49.4	48.1	$\sim$ 1.3
060801	48.1	45.9	$\sim$ 2.2
071227	47.8	**43.0**	$\sim$ **4.8**
080123	48.0	**44.5**	$\sim$ **3.5**
080503	49.7	45.8	$\sim$ **3.9**
080905A	47.1	**43.9**	$\sim$ **3.2**
090515	47.5	45.2	$\sim$ 2.3
100117A	48.5	**45.0**	$\sim$ **3.5**
101219A	48.3	45.7	$\sim$ 2.6
120305A	47.6	**43.1**	$\sim$ **4.5**
150120A	47.4	45.9	$\sim$ 1.5
160408A	48.2	46.6	$\sim$ 1.6
1604010A	49.5	48.3	$\sim$ 1.2
160624A	47.8	45.1	$\sim$ 2.7
181123B	47.9	46.0	$\sim$ 1.9
191031D	50.1	47.1	$\sim$ **3**
200219A	49.0	**43.9**	$\sim$ **5.1**
200907B	47.7	46.6	$\sim$ 1.1
211227A	48.7	**43.6**	$\sim$ **5.1**

Table 4.3: Logarithmic values of the minimum luminosity of the prompt emission preceding the rapid decay $L_{\gamma,\rm min}$ and of the luminosity $L_{p,\rm min}$ corresponding to the last detection derived from a qualitative study of the light-curves of the 19 cases included in the "EE-only" subsample. In the third column the logarithmic value of the ratio between these two quantities is reported. The values in bold in third and fourth column are the ones not matching either the $L_{p,\rm min}$- (Section 4.3.1) or the κ'-criterion (Section 4.3.2), respectively.

We conclude with the following remarks:

- the $L_{p,\rm min}$-criterion (Eq. 4.15) sets just a lower limit below which we confidently exclude the eventuality to observe a plateau, but does not give any information when our observations are limited to higher luminosities;

- the κ'-criterion (Eq. 4.18), instead, sets a general relation between the luminosity of the prompt emission and the luminosity of the magnetar-powered afterglow and can be useful also at high luminosities. Indeed, this additional criterion allowed us to rule out two more GRBs, that were not excluded with the $L_{p,\rm min}$ criterion because of the high luminosity at which they went undetected.

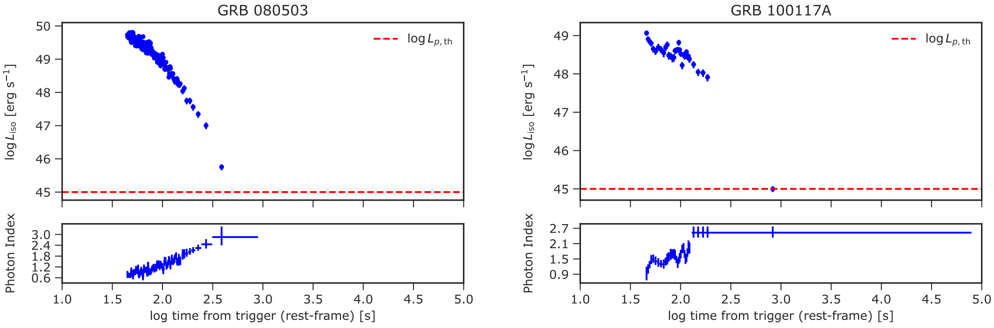

(a) **(b)**

Figure 4.3: Two example of isotropic luminosity light-curves for two cases classified as "EE-only (no magnetar)", i.e. cases which failed to match either one or both $L_{p,\rm min}$- and κ'-criteria and for which we could confidently rule out the presence of a magnetar. Indeed: **(a)** $L_{p,\rm min} > 10^{45}$ erg s^{-1}, but $\kappa' > 10^3$; instead, for **(b)** both $L_{p,\rm min} < 10^{45}$ erg s^{-1} and $\kappa' > 10^3$ are observed. The red dashed line represents luminosity threshold $L_{p,\rm th}$ defined in Eq. 4.15.

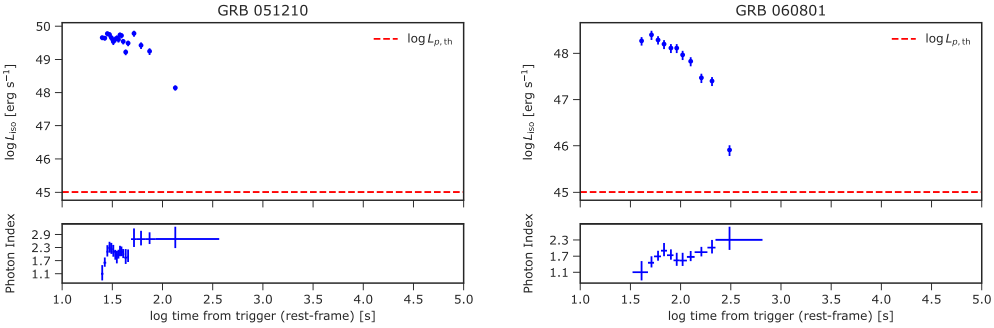

(a) **(b)**

Figure 4.4: Two example of isotropic luminosity light-curves for two cases classified as "EE-only (inconclusive)", i.e. cases for which both $L_{p,\rm min}$- and κ'-criteria were satisfied, and so it was not possible to rule out the presence of a magnetar. Indeed, for both **(a)** and **(b)**, $L_{p,\rm min} > 10^{45}$ erg s^{-1}, $\kappa' < 10^3$. The red dashed line represents luminosity threshold $L_{p,\rm th}$ defined in Eq. 4.15.

To summarize, out of the 19 bursts included in the "EE-only" sample, the 9 cases for which it was possible to confidently rule out the presence of a magnetar were classified as "EE-only (no magnetar)" (two examples are shown in Fig. 4.3). The remaining 10 bursts, i.e. the ones that matched both our criteria, were instead cases in which it was not possible to either confirm or rule out the presence of a magnetar: these were classified as "EE-only (inconclusive)" (two examples are reported in Fig. 4.4). The importance of this additional classification is clarified in the following section.

4.4 "Magnetar" fraction

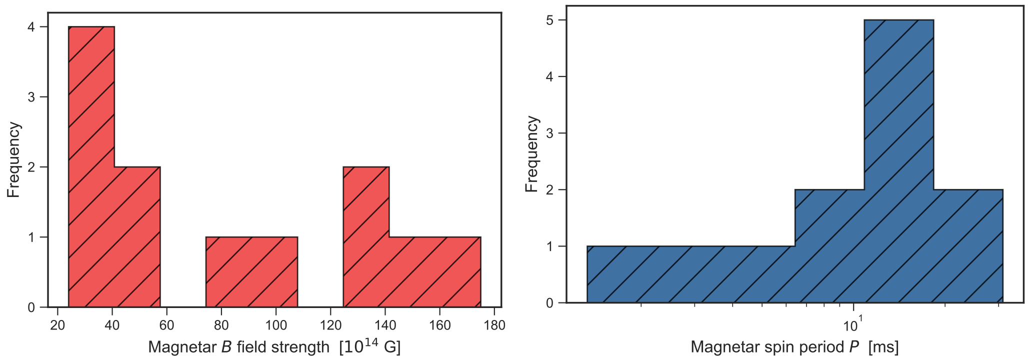

(a) **(b)**

Figure 4.5: Distribution of best-fit values of the magnetar parameters, **(a)** B field strength and **(b)** spin period P (time axis in logarithmic scale), derived for the 12 bursts for which the fitting of the luminosity light-curves with the magnetar model resulted successful. The 3 cases classified as "failed magnetars" are not represented.

Out of the 15 cases included in the "plateau" subsample, only 12 resulted in being good magnetar candidates: these defined the final "magnetar" subsample (Section 4.2). On the other hand, 3 cases were classified as "failed magnetar" since it was not possible to constrain the values of B and P from the fit. The values of the best fit parameters B and P for the "magnetar" subsample are reported in Fig. 4.5a and Fig. 4.5b, respectively. The values of B lie in the range between $\sim 24 \times 10^{14}$ G and $\sim 175 \times 10^{14}$ G, while the values of P are included in the range between 1.33 ms and 31 ms: both these parameters are within the ranges expected for magnetars.

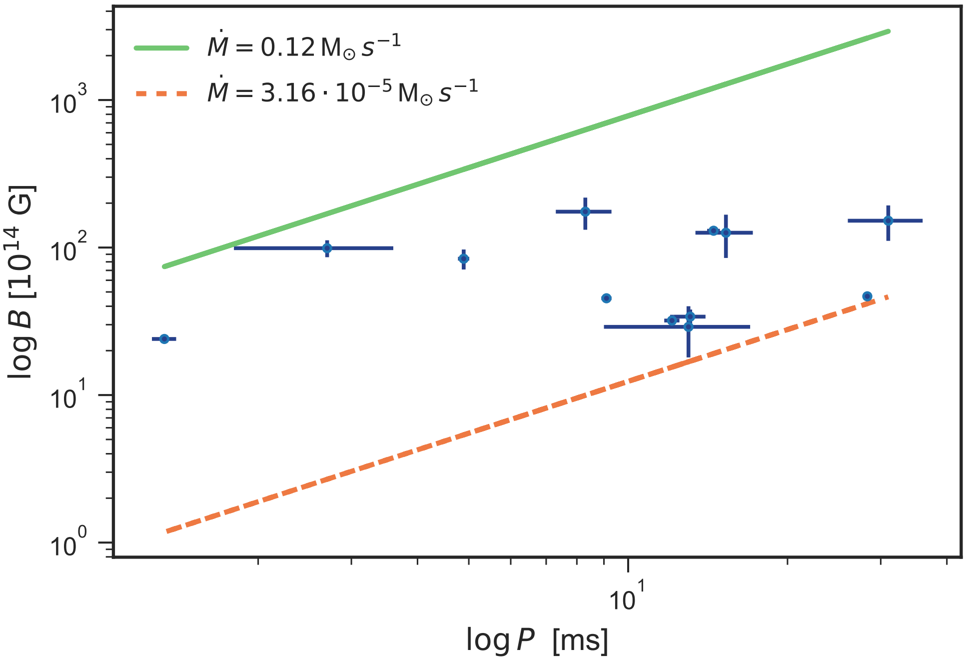

Figure 4.6: Best fit values (with associated errors, in blue) obtained from the magnetar model fit, reported on the $\log B - \log P$ plane. There is evidence of a correlation between B and P, as expected from the physics of the spin-up line for accreting NSs in Galactic binary systems: the orange and green lines represent the expected $B - P$ relations from accreting NSs with mass accretion rates of $3.16 \times 10^{-5}\,M_\odot\ s^{-1}$ and $0.12\,M_\odot\ s^{-1}$, respectively.

In Fig. 4.6 the best fit values of B and P are plotted in the $\log B - \log P$ plane. We compared these values with those expected from accreting NSs: indeed, several studies regarding the physics of the spin-up line for accreting NSs in Galactic binary systems have firmly proven the existence of $B - P$ correlation. In particular, fixing a value of the NS mass accretion rate $\dot{M}$, one can derive the relation (Bhattacharya & van den Heuvel, 1991; Yuanyue et al., 2013):

$$\frac{B}{10^{14}\,\mathrm{G}} \simeq \left(\frac{P_{\mathrm{eq}}}{1\,\mathrm{ms}}\right)^{7/6} \left(\frac{M_{\mathrm{NS}}}{1.4\,\mathrm{M}_\odot}\right)^{5/6} \left(\frac{\dot{M}}{0.01\,\mathrm{M}_\odot\,\mathrm{s}^{-1}}\right)^{1/2} \left(\frac{R_{\mathrm{NS}}}{12\,\mathrm{km}}\right)^{-3}, \quad (4.19)$$

where P_{eq} represents the so-called equilibrium period reached by the NS for that specific value of $\dot{M}$.

Considering the fixed values of NS mass and radius that were used in the magnetar model fit ($M_{\mathrm{NS}} = 1.4\,\mathrm{M}_\odot$ and $R_{\mathrm{NS}} = 12$ km), from Fig. 4.6 it is quite clear that, in the $B - P$ plane, all the derived best fit values are well comprised within the two lines obtained assuming a range of accretion rates

$3.16 \times 10^{-5}\,\mathrm{M}_{\odot}\ \mathrm{s}^{-1} < \dot{M} < 0.12\,\mathrm{M}_{\odot}\ \mathrm{s}^{-1}$: these values are in line with past results (Bernardini, 2015; Stratta et al., 2018), suggesting that the same basic physics of accreting NS is at play also in SGRBs (assuming higher values of $\dot{M}$ compared to Galactic NS).

A graphic summary of the whole analysis process is portrayed in Fig. 4.7.

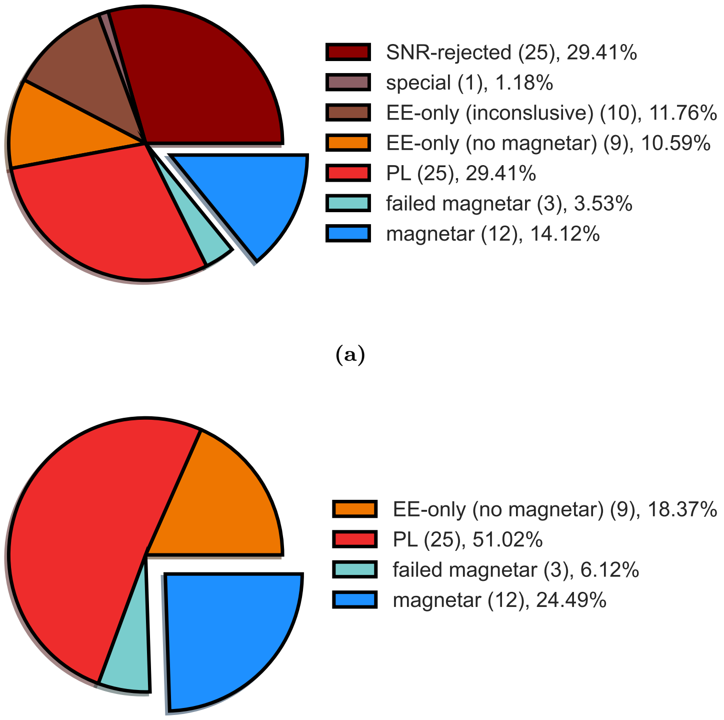

(a)

(b)

Figure 4.7: Pie charts showing how many SGRBs were found to be good magnetar candidates, **(a)** with respect to the whole sample of 85 SGRBs, or **(b)** only with respect to the cases on which we were able to draw conclusions on the presence of a magnetar, either with the light-curve fitting or with the considerations introduced about the "EE-only" sample: corresponding to a "magnetar" fraction $0.141 < f_{\mathrm{mag}} < 0.245$.

This further classification led us to evaluating different strategies to understand the fraction of SGRBs which resulted in being good magnetar candidates: indeed, considering the 12 good "magnetar" candidates with respect to the initial sample of 85 bursts, the associated "magnetar" fraction is $f_{\mathrm{mag}}^{min} = 0.141$ of the total. By contrast, it is reasonable to exclude from the computation of this fraction all the cases for which we were not able to draw any conclusion: this includes the "SNR-rejected" subsample (25), the "special case" of GRB 150101B and, thanks to the considerations on the "EE-only" subsample provided for in Section 4.3, the 10 cases defined as "EE-only (inconclusive)". In this way, the fraction is computed over a total of 49 bursts ("PL", "magnetar", "failed magnetar" and "EE-only (no magnetar) subsamples), leading to a significant increase of the fraction, $f_{\mathrm{mag}}^{max} = 0.245$.

The range derived for the "magnetar" fraction, namely $0.141 < f_{\mathrm{mag}} < 0.245$ will be exploited in Chapter 5 to constrain the value of the maximum stable mass of a BNS merger remnant. A further discussion of these value is reported in Chapter 6.

Chapter 5

Astrophysical implications

In this chapter, the results derived from the previous analysis are exploited to derive constraints regarding the physical properties of BNS mergers. In Section 5.1, we briefly describe the different possible outcomes of a BNS merger, focusing in particular on the role played by the maximum mass of a gravitationally stable NS remnant, $M_{\max}$. The concepts of baryonic and gravitational mass, introduced in Section 5.2 with a particular focus on the semi-universal relation for NS mass (e.g., Lattimer, 2021), are used in Section 5.3 to constrain the value of $M_{\max}$ based on our interpretation of SGRB plateaus. These constraints are reported and discusses in Section 5.4.

5.1 BNS merger remnants

BNS and NS-BH mergers are unique laboratories for studying the physical properties of matter at supra-nuclear densities. Moreover, in contrast to binary BH-BH mergers, which are sources of GW but do not have any bright electromagnetic (EM) counterpart, BNS mergers provide a link between EM and GW signals. SGRBs were the earliest EM counterparts proposed for BNS mergers and in the standard scenario they represent the emission produced by a relativistic jet originated by the accretion of a debris torus onto a newly formed BH, remnant of the merger (Paczynski, 1986; Eichler et al., 1989; Popham et al., 1999): this was later tested via various general-relativistic magneto-hydrodynamic (GRMHD) simulations (Ruiz et al., 2016), but it is still far from becoming the definitive interpretation. Indeed, while the remnant of a NS-BH merger is inevitably a BH, BNS mergers can also lead to the creation of a NS as a remnant: the final outcome of the merger is strongly dependent on the initial mass of the binary system and on the NS equation of state (EOS).

The determination of the NS EOS is still a highly debated topic, particularly at super-nuclear densities because of our limited understanding of nuclear interactions in that regime, which is beyond the reach of terrestrial laboratories. However, given a fixed mass of the binary system, a different EOS will determine whether a stable object can be formed or not (Baiotti et al., 2008; Hotokezaka, Kyutoku, et al., 2011). The great uncertainty about the EOS limits the precision with which crucial properties of the NS like its radius or its maximum stable mass $M_{\max}$ can be derived: this is why only indirect limits exist for $M_{\max}$, which were obtained only under specific assumptions from the observation of SGRBs, or by modeling the NS mass distribution. In any case, $M_{\max}$ is the key parameter deciding the fate of a BNS merger, namely the type of remnant that is formed and the resulting EM signal (Fig. 5.1).

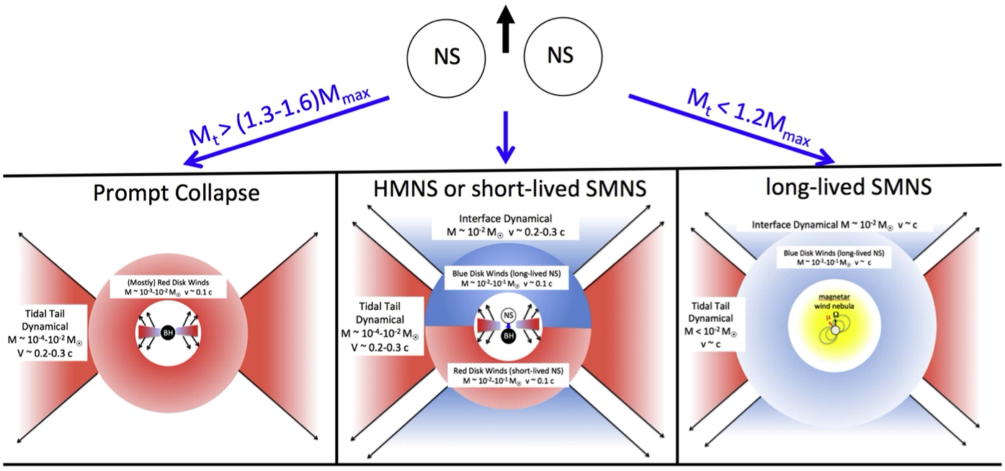

Figure 5.1: Artistic representation of the possible outcomes of a binary neutron star (BNS) merger. The compact remnant that forms immediately after the merger is strongly dependent on the value of total mass of the original binary system $M_{\rm tot}$ and its magnitude with respect to the maximum stable mass for a neutron star, $M_{\max}$. If the BNS is too massive ($M_{\rm tot} > (1.3-1.6)M_{\max}$), the remnant undergoes a prompt collapse into a BH (*on the left*). Conversely, a low mass BNS ($M_{\rm tot} < 1.2M_{\max}$) would generate a long-lived, stable SMNS, injecting its large rotational energy into the ejecta (*on the right*). In the intermediate case ($1.2M_{\max} < M_{\rm tot} < (1.3-1.6)M_{\max}$) either a HMNS or a short-lived SMNS are produced, but both thess objects are thought to eventually collapse into a BH (*in the center*). Shaded-coloured areas indicate the red and blue kilonova signatures (Margalit and B. D. Metzger, 2017).

Inspecting the different outcomes, in the case in which the total mass of the binary system $M_{\rm tot}$ is too high, the merger product will experience a dynamical scale, or "prompt", collapse to a BH. This happens when $M_{\rm tot}$ overcomes the critical threshold $M_{\rm th} \approx kM_{\max}$, where $k \approx 1.3-1.6$ is a factor inversely proportional to the NS compactness parameter $C_{\rm max} = GM_{\rm max}/(R_{1.6}c^2)$, with $R_{1.6}$ is the radius of a $1.6\,{\rm M}_\odot$ neutron star (Bauswein, Goriely, et al., 2013). When instead the binary mass is slightly smaller, $M_{\rm tot} \lesssim M_{\rm th}$ the remnant of the merger will be a hyper-massive neutron star (HMNS) which is a NS sustained against gravitational collapse for a very short time (from $\sim$ ms to $\sim$ 100 ms), by strong differential rotation. For the cases in which $M_{\rm tot} \lesssim 1.2\,M_{\rm max}$, the merger produces a supra-massive NS (SMNS) which will remain stable even when, around $\lesssim 10 - 100$ ms from the merger, differential rotation will be no more present thanks to uniform rotation, but also in this case GWs and magnetic dipole radiation will eventually cause the collapse on of seconds (or few minutes in the most extreme cases).The final case is that of a binary with an extremely low mass, $M_{\rm tot} \lesssim M_{\rm max}$: the remnant will be an indefinitely stable NS (Margalit and B. D. Metzger, 2017). Regardless of these differences, HMNSs, SMNSs or even stable NS are expected to emit a GW signal even in the phases following the merger for several tens of ms or even more: the detection of this post-merger GW emission could give us an insight on the nature of the remnant and also place constrains on the NS EOS (Margalit and B. D. Metzger, 2017).

5.2 NS semi-universal relation

When talking about the mass of self-graviting objects, and in particular of compact objects, it is fundamental to make a clear distinction between the baryonic mass M_b and the gravitational mass M_g.

- The baryonic mass M_b is the sum of the masses of the individual baryons forming the star (valid for any self-gravitating object like normal stars, white-dwarfs and NSs) and is expressed as (Shapiro & Teukolsky, 1983):

$$M_b = 4\pi \int_0^R \left[1 - \frac{2Gm(r)}{rc^2}\right]^{-1/2} \rho r^2 dr, \tag{5.1}$$

  where R is the object radius, $m(r)$ is the enclosed mass at a given radius and ρ is the rest-mass density. The factor inside the square brackets is needed to account for the effect of gravitational redshift.

- The gravitational mass is instead defined as:

$$M_g = 4\pi \int_0^R \frac{e}{c^2} r^2 dr, \tag{5.2}$$

where e is the energy density, accounting not just for the rest-mass but also for the (negative) binding energy, thus reducing the total energy.

Both these equations are derived under the assumption that the object is non rotating, but similar results can be obtained in the case of rotating models.

The key point here is that, in general, $M_b \geq M_g$: indeed, considering the relativistic relation between mass and energy, M_g can be thought as the sum of M_b and the negative contribution $E_{\mathrm{bind}} \sim -GM^2/R < 0$, so that:

$$M_g = \frac{E_{\mathrm{tot}}}{c^2} = \frac{M_b\, c^2 + E_{\mathrm{bind}}}{c^2} = M_b + \frac{E_{\mathrm{bind}}}{c^2} \leq M_b \tag{5.3}$$

For generic self-graviting objects the contribution of E_{bind} is typically negligible, making $M_b \approx M_g$ (this is true to an accuracy of $\sim 10^{-6}$ even in white dwarfs). However, this is not the case in compact objects like NS or BH, as E_{bind}/c^2 becomes comparable to, yet smaller than, M_b.

The relation between the baryonic and gravitational mass of NS, which in principle is dependent on the EOS adopted, can be approximated to an accuracy of a few percent by a semi-universal relation (quasi EOS-independent) of the form (both masses are expressed in solar units, Lattimer, 2021):

$$M_b = M_g + (0.0602 \pm 0.0016) M_g^2 + (0.0180 \pm 0.0065) M_g^3. \tag{5.4}$$

Adopting this approximate relation, it is possible to derive a similar relation also for the remnant that would form from the merger of a BNS system. Indeed, if $M_{b,1}$ and $M_{b,2}$ are the baryonic masses of the two NS forming the binary, they can be expressed as a function of their gravitational masses $M_{g,1}$ and $M_{g,2}$ through Eq. 5.4. By doing so, the baryonic mass of the remnant of the merger between these two objects will be expressed as:

$$M_{b,\mathrm{rem}} = M_{b,1} + M_{b,2} - M_{\mathrm{ej}}, \tag{5.5}$$

where M_{ej} is the mass of the material ejected in the merger (in solar units), while $M_{b,\mathrm{rem}}$ is linked to $M_{g,\mathrm{rem}}$ through Eq. 5.4, as expected for a NS.

5.3 BNS merger simulation

As stated in Section 5.1, a fundamental parameter of a BNS merger is M_{max}, the maximum stable mass of the remnant but, since this value strongly depends on the NS EOS, up to now no definitive observational/theoretical upper limits exist. However, several studies tried to derive indirect limits on this value, through the study of the mass distribution of NSs and of the properties of SGRBs, but all these results were obtained under strong assumptions (Piro et al., 2017).

In this Thesis we will follow a similar approach, and use the results of our analysis in Chapter 3 and the confirmation on the validity of the magnetar model obtained in Chapter 4 to derive some constraints on the value of $M_{\rm max}$. Nonetheless, to obtain our results we are forced to make some strong assumptions:

- we assume that all SGRBs are produced by BNS mergers;
- we assume that $M_{\rm max}$ sets a threshold between two possible outcomes of the merger: the remnant will promptly collapse to a BH in the case $M_{g,{\rm rem}} \gtrsim M_{\rm max}$, while it will form an indefinitely stable NS if $M_{g,{\rm rem}} \lesssim M_{\rm max}$. As explained in Section 5.1, this is a simplification, and we will discuss its implications in Section 5.4;
- we interpret the plateau as the result of the extra energy injection provided by a magnetar central engine.

Moreover, we adopted the semi-universal relation between M_b and M_g of NS proposed by Lattimer, 2021 (Eq. 5.4). Within this framework, it is possible to identify the fraction $f_{\rm mag}$ derived in Section 4.4 (i.e., the fraction of SGRBs which resulted in being good magnetar candidates) with the fraction of BNS merger that create a stable NS remnant.

The code used for the following computation is reported in Appendix A.1 and is available on Luca Guglielmi, SGRB-thesis, (2023), GitHub repository[1].

Our starting point consisted in generating a population of 10^5 BNS, which represented the initial sample needed to start the computation of the mass distribution of the merger remnant. To create the BNS population, the gravitational masses of the two components of the binary, $M_{g,1}$ and $M_{g,2}$, were drawn from a Gaussian distribution with a mean of $\mu = 1.33\,{\rm M}_\odot$ and standard deviation of $\sigma = 0.09\,{\rm M}_\odot$, where these values are the ones derived from the Galactic NS population (as presented in Kiziltan et al. (2013), Antoniadis et al. (2016), and Özel and Freire (2016)):

$$\mathcal{P}(M_g|\mu,\sigma) = \frac{1}{\sqrt{2\pi}\sigma}\exp\left[-\frac{(M_g-\mu)^2}{2\sigma^2}\right]. \tag{5.6}$$

The gravitational mass distributions of the two components obtained in this way, $M_{g,1}$ and $M_{g,2}$, were then translated in baryonic mass distributions

---

[1] `https://github.com/gugliluc/SGRB-thesis`

$M_{b,1}$ and $M_{b,2}$ through the semi-universal relation in Eq. 5.4. By doing so, it was then possible to merge these two populations using Eq. 5.5 in order to obtain the baryonic mass distribution of the remnant, $M_{b,\mathrm{rem}}$. At first, the mass of the ejected material was assumed to be negligible ($M_{\mathrm{ej}} = 0\,\mathrm{M}_{\odot}$), being aware that any value larger than 0 would result in a lower value of M_{max}.

However, since our observable is the gravitational mass, it was necessary to exploit again Eq. 5.4 to transform $M_{b,\mathrm{rem}}$ into the gravitational mass of the remnant $M_{g,\mathrm{rem}}$. This was achieved fixing the two coefficients at their expectation values, and solving for $M_{g,\mathrm{rem}}$ the obtained third degree equation:

$$M_{b,\mathrm{rem}} = M_g + 0.0602 M_{g,\mathrm{rem}}^2 + 0.0180 M_{g,\mathrm{rem}}^3, \ . \tag{5.7}$$

Considering the 10^5 values of $M_{g,\mathrm{rem}}$ obtained in this way, it was possible to derive the mean μ_{rem} and the standard deviation σ_{rem} of this sample, in order to define the associated Gaussian distribution $\mathcal{P}(M_{g,\mathrm{rem}}|\mu_{\mathrm{rem}}, \sigma_{\mathrm{rem}})$, according to Eq. 5.6.

What we obtained at this point is the probability distribution of the gravitational mass of the merger remnant. This distribution provides a way to link the "magnetar" fraction f_{mag} with the fraction of BNS mergers which would produce a stable remnant. Indeed, under the starting assumptions, all the merger remnants with masses $M_{g,\mathrm{rem}} \gtrsim M_{\mathrm{max}}$ will directly collapse into a BH, while the ones with masses $M_{g,\mathrm{rem}} < M_{\mathrm{max}}$ will form indefinitely stable neutron stars. However, since it is reasonable to assume that only a stable object can provide for the prolonged energy injection needed to explain the plateau in the magnetar model framework, it is natural to connect the "magnetar" fraction (fraction of SGRBs which resulted good candidates for the presence of a magnetar as central engine) to the fraction of merger remnants which are expected to be stable, namely:

$$f_{\mathrm{mag}} \equiv \mathcal{P}(M_{g,\mathrm{rem}} < M_{\mathrm{max}}) \tag{5.8}$$

This can be done deriving the value of mass for which the cumulative distribution function (CDF) of the probability distribution of remnant mass returns a value coinciding with that of f_{mag}. This is exactly the definition of quantile function $\mathcal{Q}$, thus one can write:

$$\mathcal{Q}(f_{\mathrm{mag}}) \equiv \mathrm{CDF}^{-1}(\mathcal{P}(M_{g,\mathrm{rem}} < M_{\mathrm{max}})) = M_{\mathrm{max}} \tag{5.9}$$

The value of M_{max} derived with this procedure is exactly the maximum mass for a stable remnant, defining the mass threshold above which we expect the prompt collapse of the remnant into a BH. This whole procedure was carried out both for the minimum and maximum "magnetar" fraction, $f_{\rm mag}^{\rm min} = 0.141$ and $f_{\rm mag}^{\rm max} = 0.245$ respectively, derived in Chapter 4.

In Fig. 5.2 these results are represented graphically. The green histogram is the initial mass distribution of the NS components of the binary system, obtained drawing 10^5 outcomes from the Galactic distribution of BNSs. The Gaussian distribution of the remnant masses $M_{g,\rm rem}$ is instead represented by the red line, $\mathcal{P}(M_{g,\rm rem}|\mu_{\rm rem}, \sigma_{\rm rem})$. The value of $M_{\rm max}$ was derived both for the minimum "plateau" fraction $f_{\rm mag}^{\rm min}$ (Fig. 5.2a, $M_{\rm max} = 2.27\,{\rm M}_\odot$) and for the maximum "plateau" fraction $f_{\rm mag}^{\rm max}$ (Fig. 5.2b, $M_{\rm max} = 2.31\,{\rm M}_\odot$), assuming an initial value of the ejected mass $M_{\rm ej} = 0$. This values clearly separate between the range of masses in which we expect that a stable NS remnant forms (azure region) and the range in which instead the remnant is expected to be unstable and to collapse to a BH (yellow region).

$M_{\rm ej}$	$f_{\rm mag}^{\rm min} = 0.141$	$f_{\rm mag}^{\rm max} = 0.245$
0	2.269	2.308
0.005	2.267	2.304
0.010	2.262	2.301
0.015	2.259	2.298
0.020	2.256	2.295
0.025	2.253	2.292
0.030	2.249	2.288
0.035	2.246	2.285
0.040	2.243	2.282
0.045	2.240	2.279
0.050	2.237	2.275
0.055	2.233	2.272
0.060	2.230	2.269
0.065	2.227	2.266
0.070	2.223	2.263
0.075	2.220	2.259
0.080	2.217	2.256
0.085	2.214	2.253
0.090	2.210	2.250
0.095	2.207	2.246
0.100	2.204	2.243

Table 5.1: Values of the maximum stable mass of the BNS remnant $M_{\rm max}$ computed both for $f_{\rm mag}^{\rm min}$ and $f_{\rm mag}^{\rm max}$, assuming the mass of the ejected material ($M_{\rm ej}$) to vary in the range $[0 - 0.1]\,{\rm M}_\odot$. All the values are in solar units.

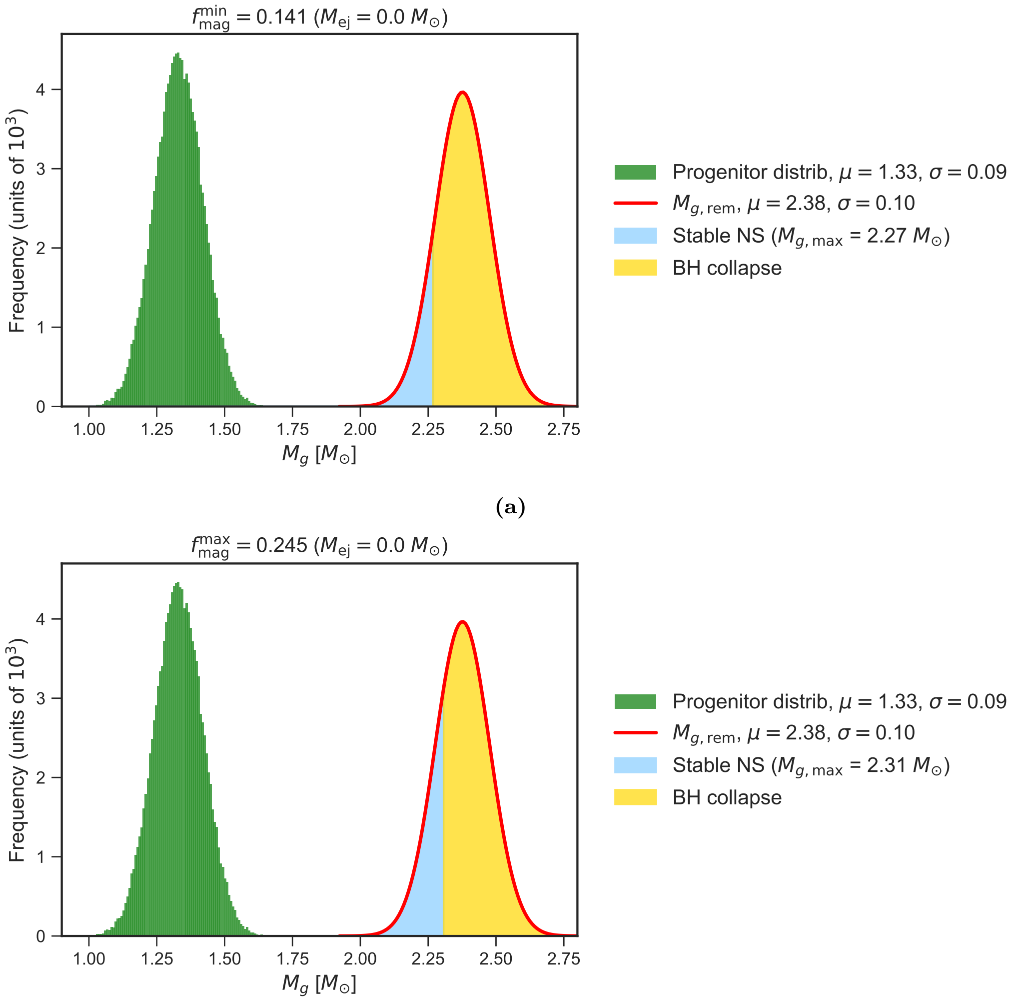

(a)

(b)

Figure 5.2: The green Gaussian represents the initial distribution of gravitational masses of the two NS composing the binary system, obtained drawing 10^5 values from the Galactic distribution of BNS ($\mu = 1.33\,\mathrm{M}_\odot, \sigma = 0.09\,\mathrm{M}_\odot$) for each component. The red line is the Gaussian function which best represents the $M_{g,\mathrm{rem}}$ distribution, $\mathcal{P}(M_{g,\mathrm{rem}}|\mu_{\mathrm{rem}}, \sigma_{\mathrm{rem}})$, obtained combining the two components, assuming a negligible mass of the ejected material ($M_{\mathrm{ej}} = 0$). The azure region represents the range of masses for which the remnant is expected to be stable, namely the masses below the threshold identified by the maximum stable mass $M_{\max}$, while the yellow region represents the range of values for which the remnant is expected to collapse to a BH. In **(a)**, a "magnetar" fraction $f_{\mathrm{mag}}^{\min} = 0.141$ was assumed, leading to a threshold $M_{\max} = 2.27\,\mathrm{M}_\odot$, while in **(b)** $f_{\mathrm{mag}}^{\max} = 0.245$, leading to a threshold $M_{\max} = 2.31\,\mathrm{M}_\odot$.

This whole procedure was repeated for values of M_{ej} spanning in the range $[0 - 0.1]\,\mathrm{M}_\odot$, increasing the value of $0.005\,\mathrm{M}_\odot$ at each iteration and computing $M_{\max}$ both for $f_{\rm mag}^{\rm min}$ and $f_{\rm mag}^{\rm max}$. The upper value of $0.1\,{\rm M}_\odot$ was taken as a secure upper bound since from simulation the mass of the ejecta appears to be always smaller than this threshold (Endrizzi et al., 2016). The obtained results are quoted in Tab. 5.1.

5.4 Maximum stable mass range

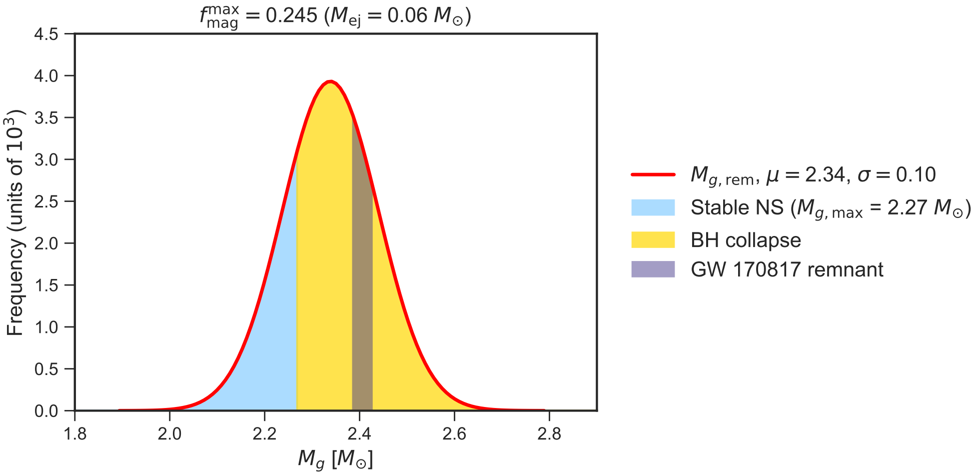

Figure 5.3: $M_{g,\rm rem}$ distribution in the case of $M_{\rm ej} = 0.06\,{\rm M}_\odot$ (red line). The azure region represents the range of masses for which a stable remnant is expected, computed assuming $f_{\rm mag}^{\rm max}$ (corresponding to $M_{\max} = 2.27\,{\rm M}_\odot$), while the yellow region is the range of masses in which the remnant is expected to collapse: interestingly, the range of values between which the remnant of GW 170817 is expected to lie (gray region) falls precisely in the unstable region, accordingly to observations which proved it collapsed to a BH.

An interesting way to validate the results found above is to compare them with the only case of detected BNS merger for which it was possible to derive the mass of the NS components: this is the case of GRB 170817/GW 170817 (Abbott et al., 2017). Indeed, for this merger the component gravitational masses are inferred to lie in the range between 1.16 and $1.60\,{\rm M}_\odot$ (with a total mass $2.73^{+0.04}_{-0.01}\,{\rm M}_\odot$), when the spins are restricted to the range observed in Galactic BNS (Abbott, 2019). Moreover, from the study of the kilonova emission associated to the event, the ejected mass for this merger was estimated to be of the order of $M_{\rm ej} = 0.06\,{\rm M}_\odot$ (Shibata & Hotokezaka, 2019). Assuming two extreme case values for the progenitor masses, i.e. *(i)* $M_{g,1} = 1.60\,{\rm M}_\odot$ and $M_{g,2} = 1.16\,{\rm M}_\odot$ and *(ii)* $M_{g,1} = M_{g,2} = 1.60\,{\rm M}_\odot$, exploiting the same approach outlined in Section 5.2, by solving Eq. 5.7 it was possible to derive a range of gravitational masses of the remnant for

GW 170817, namely $2.39 < M_{g,\mathrm{rem}}/\mathrm{M}_\odot < 2.43$. In Fig. 5.3, this range (gray region) is compared with the threshold on the maximum stable mass derived for the case of $M_\mathrm{ej} = 0.06\,\mathrm{M}_\odot$ and $f_\mathrm{mag}^\mathrm{max} = 0.245$, namely $M_\mathrm{max} = 2.27\,\mathrm{M}_\odot$ (see Tab. 5.1). From this plot, it is evident how the remnant formed in the BNS merger associated with GW 170817 falls precisely within the range of masses for which the remnant is expected to be unstable (yellow region): this is indeed confirmed by observations, which proved that even assuming that a NS remnant was formed, it collapsed to a BH within the first few ms (Margalit & B. D. Metzger, 2017; B. D. Metzger, T. A. Thompson, et al., 2018). This provide additional evidence to the legitimacy of the results obtained in Section 5.3.

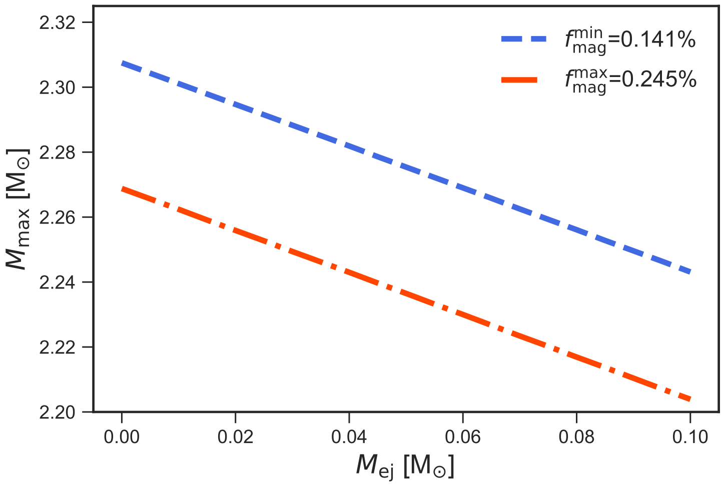

Figure 5.4: Graphic visualization of the results quoted in Tab. 5.1, showing how the value of maximum stable mass M_max depends on the mass of the ejected material M_ej. The two lines correspond to the minimum ($f_\mathrm{mag}^\mathrm{min}$, in blue) and the maximum ($f_\mathrm{mag}^\mathrm{max}$, in red) "magnetar fraction". For a fixed value of M_ej, the actual value of M_max is expected to confidently lie in the range of value defined by these two lines.

The values of M_max quoted in Tab. 5.1, can be better interpreted via a graphic representation (see Fig. 5.4): in fact, plotting the value of M_max with respect to M_ej, one can appreciate how the maximum stable mass is inversely proportional to the mass of the ejected material, since the more mass is ejected during the merger, the less massive will be the remnant. The range $[0 - 0.1]\,\mathrm{M}_\odot$ for M_ej is a conservative range inside which the value of masses of ejected material derived from BNS merger GRMHD simulations are confidently contained (Endrizzi et al., 2016). Moreover, doing the same procedure both for the minimum ($f_\mathrm{mag}^\mathrm{min}$, in blue) and the maximum ($f_\mathrm{mag}^\mathrm{max}$, in red) "magnetar" fractions derived in Chapter 4 allows to define a range of values within which the value of $M_{\rm max}$ is expected to be constrained, namely $2.20 < M_{\rm max}/{\rm M}_\odot < 2.31$.

It is interesting to notice that the value of $M_{\rm max}$ is strongly dependent on the value of $M_{\rm ej}$: during a BNS merger different amounts of ejected material would result in a completely different threshold for the stability of the remnant. The choice to calculate these values both for $f_{\rm mag}^{\rm min}$ and $f_{\rm mag}^{\rm max}$ is justified by the fact that we wanted to provide a conservative range for the values of $M_{\rm max}$ since we considered both the lowest and the highest fraction of magnetars we were able to find in our sample.

However, it is important to take into account how these results would be affected in case of relaxing the adopted working assumptions, namely *(i)* all SGRBs are produced by BNS mergers and *(ii)* the necessary condition to observe a plateau is that it must be produced by an indefinitely stable, which means an object with a mass lower than $M_{\rm max}$.

- *(i)* conceding that a considerable fraction of SGRBs are associated to NS-BH mergers, the sample on which the "magnetar" fraction is computed would be reduced, since it should include only cases in which two NS are present. This would lead to an increase of the values of $M_{\rm max}$ derived above.

- *(ii)* on the other hand, admitting that a significant number of gravitationally unstable remnants may collapse to a BH with a significant delay ($>$ several hundreds of seconds), this would mean that some of the plateaus could be produced by unstable objects too, and neglecting this would lead to overestimating the value of $M_{\rm max}$. If this were the case, taking it into account would result in a reduction of the bounds on $M_{\rm max}$.

Chapter 6

Conclusions and outlook

The launch of *Swift* in 2004 led to an unprecedented level of detail in the study of the early phases of GRB afterglows, with the definition of a canonical behaviour of their X-ray light-curves and, in particular, with the discovery of a shallow decay phase, commonly referred to as plateau, which challenged the standard synchrotron interpretation of afterglow emission. So far no consensus has been reached on the plateau origin. The currently leading interpretation invokes continuous energy injection into the afterglow-producing external shock. The source of energy can be a newly born spinning-down NS with a strong magnetic field, i.e. a magnetar. In this scenario, the incidence of plateaus in SGRBs and LGRBs encodes crucial information on the nature of the GRB engine and on its formation process. However, other possible interpretations are under study, e.g. energy injection in the form of a wide-angle jet structure being revealed over time due to the combined effects of relativistic beaming and time-delay. In general, any viable interpretation must reproduce the incidence of the observed plateaus among LGRBs and SGRBs. While it was previously established that plateaus are present in more than half of LGRBs, a reliable value for the fraction of SGRBs showing a plateau in their X-ray afterglow was still not available.

"Plateau" fraction

The main aim of this Thesis work is to compute the fraction of SGRBs with a plateau feature in their afterglow light-curve and this was achieved through a detailed analysis of one of the most updated and complete samples of SGRBs with known redshift. Out of the 85 SGRBs composing the initial sample, 15 were included in the so-called "plateau" subsample since they were found to satisfy all the criteria which we defined to ascertain the presence of a plateau.

These criteria were the following:

- an afterglow light-curve with total signal-to-noise ratio $\mathrm{SNR}_{\mathrm{tot}} \geq 10$, in order to have enough data to characterize the time behaviour;
- an afterglow for which the smoothly broken power-law (BPL) fit resulted in being statistically more significant with respect to the simple power-law (PL) fit, according to an F-test with rejection threshold at 4-σ (corresponding to a p-value of 6.2×10^{-5});
- the best-fit BPL should have the first time decay index $\alpha_1 \leq 0.75$, since the standard synchrotron afterglow model fails to give an interpretation to values below this threshold and an alternative model is needed;
- a negligible spectral variability across the power-law break, to ensure that the plateau is not caused by any kind of spectral evolution (like, e.g., in the synchrotron model) and therefore demands to be interpreted considering energy injection.

The analysis that led to identifying "plateau" sample, consisted in several steps. Initially, 45 bursts out of 85, referred to as "uninformative" events, were cast aside since they did not allow a detailed study of the afterglow: namely, the "SNR-rejected" subsample (25 bursts), lacking the statistics necessary to carry out a proper analysis; the "EE-only" subsample (19 bursts), showing only data relative to the extended emission phase; the "special case" of GRB 150101B, showing only late-time data. The remaining 40 bursts, defined as "LC-fit" sample, were subject to the light-curve fitting and allowed to define the "PL" subsample (25 bursts), for which the BPL fit was not statistically significant, and the "BPL" subsample (15 bursts), for which instead the BPL fit resulted in being a significative improvement. These latter were further studied to check the values of α_1 and the spectral variability, and eventually they were all promoted in the "plateau" subsample. In turn, this led to the definition of a minimum and maximum "plateau" fraction. Indeed, considering only the 40 bursts in the "LC fit" sample", the "plateau" subsample coincided with a fraction $f_{\mathrm{plateau}}^{\mathrm{max}} = 0.375$. On the opposite extreme, one may assume that all of the 45 bursts classified as "uninformative" are effectively cases lacking a plateau: this corresponds to a minimum fraction $f_{\mathrm{plateau}}^{\mathrm{max}} = 0.176$. Both these values happen to be much lower with respect to the fraction $\geq 50\%$ observed for LGRBs.

It is important to highlight that these results were obtained adopting a completely "agnostic" approach, without assuming any specific model for the plateau phase: this means that our results are general and may prove useful to any future work devoted to studying the origin of plateaus. However, whichever the model adopted to interpret afterglow plateaus, it must be able to explain both the range of values $0.176 < f_{\rm plateau} < 0.375$ *and* why this fraction appears to be much lower than in LGRBs.

In this respect, the "structured jet model", which is one of the two leading models adopted to explain afterglow plateaus, seems to fail in satisfying the second requirement. Indeed, this model interprets the plateau as a geometrical effect due to the combination of the angular energy profile of the jet and the orientation of the observer's line of sight. If this were the case, justifying the lower value of $f_{\rm plateau}$ in SGRBs with respect to LGRBs would require to concede that SGRBs are visible under larger viewing angles compared to LGRBs, also at high z. However, this would go against the evidence: on one hand, the observation of GRB 170817 proved that its jet had an opening angle of ~ 5 deg, quite typical of any GRB ($f_b \sim 100-200$); on the other hand, since SGRBs are on average less luminous than LGRBs, it is reasonable to expect to observe them over a similar range of angles, if anything a little smaller due to their lower luminosity. In order to explain the lower plateau incidence with geometric effects, we would have to impose significantly less beamed jets in SGRBs, visible over a wider range of lines-of-sight, opposite to existing evidence.

On the other hand, the other main theoretical model proposed to interpret the nature of plateaus in X-ray afterglows, the "magnetar model", provides a more natural interpretation of these results. Indeed, while the population of magnetars associated to CCSNe is well consistent with the rate of LGRBs (so that they may represent a large fraction of GRB central engines), it is reasonable to assume that only a fraction of BNS mergers will produce a magnetar remnant, because most remnants are expected to have masses above $M_{\rm max}$ and will thus quickly collapse to BHs, without any possibility of providing an extra energy injection.

"Magnetar" fraction

Building on the above arguments, in this Thesis work the magnetar model has been chosen to further test its validity. Fitting with this model (Dall'Osso et al., 2011; Stratta et al., 2018) the afterglow light-curves of the 15 bursts included in the "plateau" subsample, we identified 12 of them as good magnetar candidates, defining the "magnetar" subsample, while 3 of them were found to be inconsistent with the magnetar model and were classified as "failed magnetars": these latter call for further study in the future. Comparing the "magnetar" subsample to the initial sample, we derived a minimum "magnetar" fraction $f_{\rm mag}^{\rm min} = 0.141$. This is a conservative value obtained assuming that all the 45 bursts classified as "uninformative" do not effectively host a magnetar central engine. However, reconsidering the 19 bursts included in the "EE-only" subsample in the framework of the magnetar model, it was possible to confidently exclude the presence of a magnetar in 9 of them, defined as "EE-only (no magnetar)": this allowed to recompute the "magnetar" fraction considering only on the 49 bursts ("EE-only (no magnetar)"+ "magnetar"+ "failed magnetar"+"PL") for which it was possible to discriminate if a magnetar was present or not, obtaining the maximum value $f_{\rm mag}^{\rm max} = 0.245$.

The range of values derived for the "magnetar" fraction, $0.141 < f_{\rm mag} < 0.245$, was then exploited to derive physical constraints on the nature of the remnant itself.

Constraints on $M_{\rm max}$

The values of $f_{\rm mag}$ obtained in our work were exploited to infer an upper and lower bound for the maximum stable mass, $M_{\rm max}$, of the NS remnant of a BNS merger. The range of values derived simulating the merger of a sample population of 10^5 BNSs drawn from the galactic NS mass distribution is depicted in Fig. 5.4 for both values of $f_{\rm mag}$ and for $M_{\rm ej}$ in the range $[0 - 0.1]\,{\rm M}_\odot$. We obtained $2.20 < M_{\rm max}/{\rm M}_\odot < 2.31$: these values are subject to some uncertainties due to the fact that they were derived under the assumptions that *(i)* all SGRBs are produced by BNS mergers and *(ii)* a plateau phase can be produced only by an indefinitely stable remnant, which is strictly required to have a gravitational mass lower than $M_{\rm max}$. Letting go of either of these would affect to some extent the bounds mentioned above (as discussed in Section 4.4).

However, our derived range for $M_{\rm max}$ is consistent with the values obtained by GRMHD simulations performed in the past years, or by combining the GW observations of merging systems of BNS and quasi-universal relations (e.g. Piro et al., 2017; Rezzolla et al., 2018).

Future prospects

The natural extension of this Thesis work is the development of the energy injection in a jet with wide angular structure, in order to capture details of the observations that are not described by the current version of the model, like, e.g., the effect of a moderately off-axis view of the jet or the evolution of the broadband light-curve, including the optical data when available. This will allow a more accurate description of the available data and a better characterization of the magnetar physical properties, the spin period and the magnetic field strength.

An additional secure future development of the analysis will be to extend it to the whole sample of *Swift*'s SGRBs, taking into account also the more recent bursts and the bursts which were not considered in our initial sample because they lacked the information about the redshift, which instead resulted fundamental in the comparison of our results with the magnetar model. This would allow to derive the "plateau" fraction f_{plateau} on a much larger sample, leading to an even more solid and general value which could then be used as a strong reference for any work devoted to interpreting the origin of the plateau phase in SGRBs. Moreover, in this work f_{plateau} has been proven to be a good proxy of the "magnetar" fraction f_{plateau}: in this perspective, an eventual confirmation of its value even on a larger sample would provide us with additional evidence on the robustness of our conclusion regarding the maximum stable mass of BNS remnants.

In the forthcoming years, the current and future scientific runs of *Advanced* LIGO and *Virgo* and, even more so, the increased sensitivity that will be achieved by the *Einstein Telescope* will enable to derive information about the masses of NS components and of BNS merger remnants with an unprecedented detail. Therefore, the prospective confirmation of the values of M_{max} derived in this Thesis work will allow to further validate the hypothesis that SGRBs are produced by compact object mergers and to add a new, crucial piece of evidence in favour of the magnetar model.

Appendix A

Appendices

A1: E_{iso} values

Table A.1: Values of the isotropic equivalent energy E_{iso}, expressed in units of 10^{52} erg, for the 42/85 SGRBs in the initial sample for which it was possible to recover information about this value. Note that, depending on the reference, the range of energies chosen to compute E_{iso} may be different. Bold entries are the 15 SGRBs included in the "plateau" subsample.

GRB name	E_{iso} (10^{52} erg)	Reference
050724	0.024	Tsvetkova, Frederiks, Svinkin, et al., 2021
051221A	0.31	Tsvetkova, Frederiks, Golenetskii, et al., 2017
060313	2.9	W. Fong, Berger, Margutti, et al., 2015
060614	0.27	Tsvetkova, Frederiks, Golenetskii, et al., 2017
060801	0.478	Tsvetkova, Frederiks, Golenetskii, et al., 2017
061006	0.21	Tsvetkova, Frederiks, Golenetskii, et al., 2017
061201	0.017	Tsvetkova, Frederiks, Golenetskii, et al., 2017
070714B	0.64	Tsvetkova, Frederiks, Golenetskii, et al., 2017
070724A	0.03	W. Fong, Berger, Margutti, et al., 2015
070809	0.09	W. Fong, Berger, Margutti, et al., 2015
071227	0.059	Tsvetkova, Frederiks, Golenetskii, et al., 2017
080905A	0.02	W. Fong, Berger, Margutti, et al., 2015
081226A	0.09	W. Fong, Berger, Margutti, et al., 2015
090426	0.24	Tsvetkova, Frederiks, Svinkin, et al., 2021
090510	5.71	Tsvetkova, Frederiks, Golenetskii, et al., 2017
091109B	0.18	W. Fong, Berger, Margutti, et al., 2015

Continue on the next page

Table A.1: Values of the isotropic equivalent energy E_{iso}, expressed in units of 10^{52} erg, for the 42/85 SGRBs in the initial sample for which it was possible to recover information about this value. Note that, depending on the reference, the range of energies chosen to compute E_{iso} may be different. Bold entries are the 15 SGRBs included in the "plateau" subsample.(cont.).

GRB name	E_{iso} (10^{52} erg)	Reference
100117A	0.22	W. Fong, Berger, Margutti, et al., 2015
100206A	0.051	Tsvetkova, Frederiks, Golenetskii, et al., 2017
101219A	0.651	Tsvetkova, Frederiks, Golenetskii, et al., 2017
110112A	0.03	W. Fong, Berger, Margutti, et al., 2015
110402A	1.52	Minaev and Pozanenko, 2019
111117A	0.55	W. Fong, Berger, Margutti, et al., 2015
120804A	0.657	Tsvetkova, Frederiks, Golenetskii, et al., 2017
121226A	0.37	W. Fong, Berger, Margutti, et al., 2015
130603B	0.196	Tsvetkova, Frederiks, Golenetskii, et al., 2017
130912A	0.16	W. Fong, Berger, Margutti, et al., 2015
131004A	0.138	Tsvetkova, Frederiks, Svinkin, et al., 2021
140129B	0.07	W. Fong, Berger, Margutti, et al., 2015
140516A	0.02	W. Fong, Berger, Margutti, et al., 2015
140622A	0.07	W. Fong, Berger, Margutti, et al., 2015
140903A	0.08	W. Fong, Berger, Margutti, et al., 2015
140930B	0.40	W. Fong, Berger, Margutti, et al., 2015
150101B	0.004	W. Fong, Berger, Margutti, et al., 2015
150424A	0.434	Tsvetkova, Frederiks, Golenetskii, et al., 2017
151229A	0.12	Zhu et al., 2023
160410A	9.3	Tsvetkova, Frederiks, Golenetskii, et al., 2017
161001A	0.30	Zhu et al., 2023
170728B	0.40	Zhu et al., 2023
180618A	0.39	Zhu et al., 2023
210323A	0.43	Zhu et al., 2023
211211A	1.24	Zhu et al., 2023
191019A	0.1	Lazzati et al., 2023

A2: Results obtained from the light-curve fitting

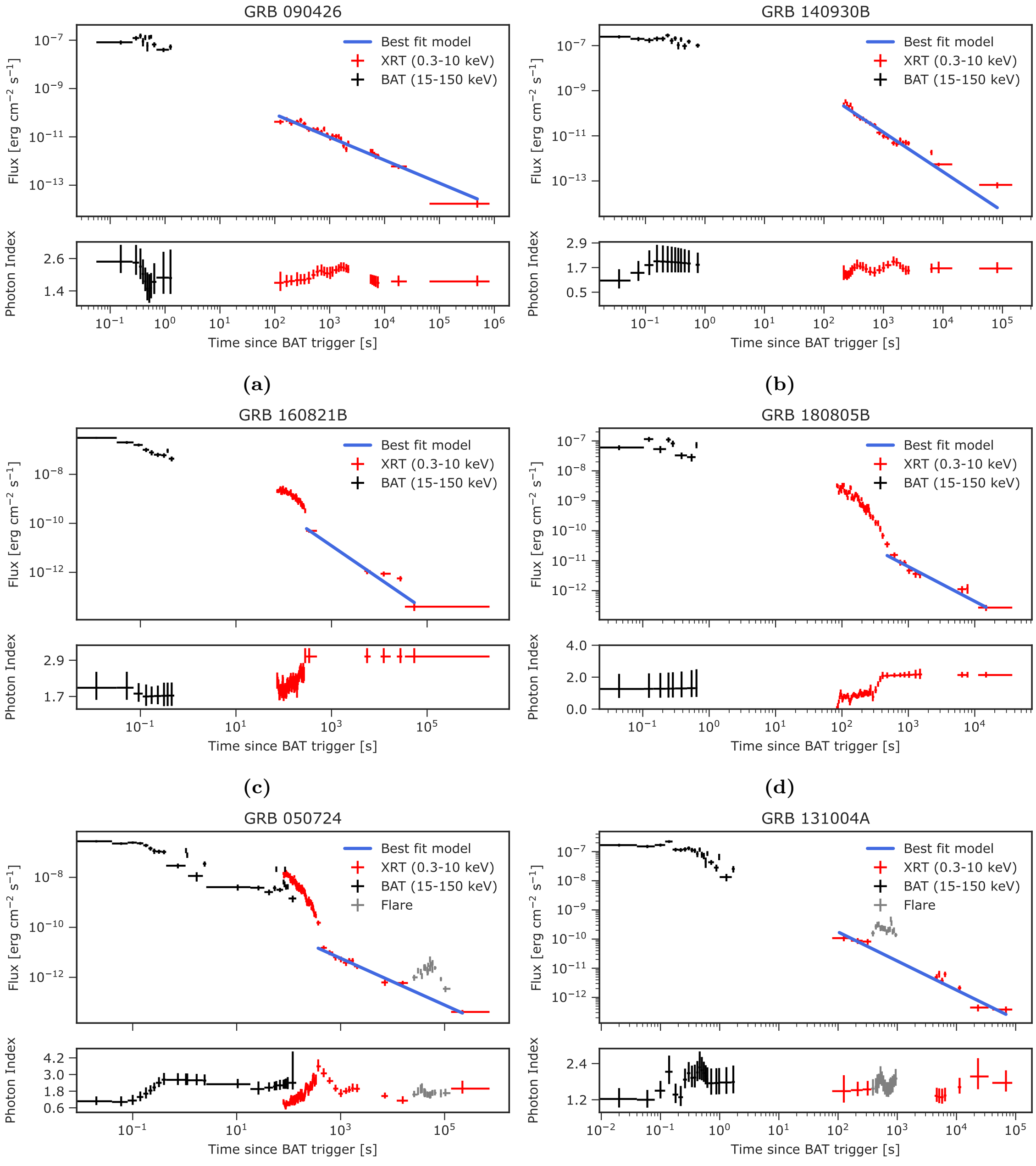

(a) (b) (c) (d) (e) (f)

Figure A.1: Light-curves of the SGRBs for which a power-law fit (PL, in green) was found to be was found to be enough to reproduce the data, since the broken power-law (BPL) was found to be not statistically significant. **(e)** and **(f)** are the two cases showing a flare, which was exvluded from the fit.

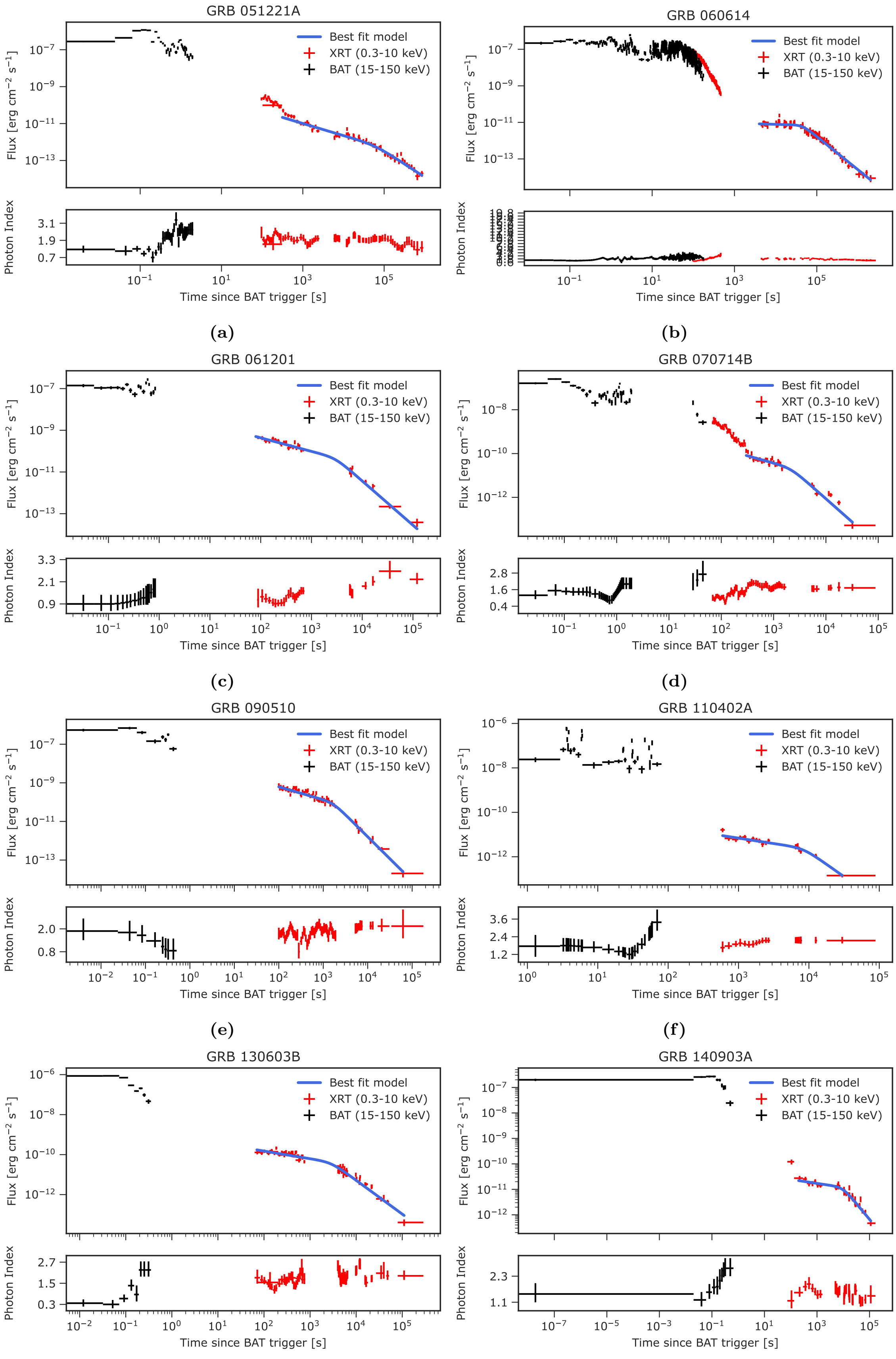

(a) (b) (c) (d) (e) (f) (g) (h)

Figure A.2: Light-curves of the 15 SGRBs for which a broken power-law fit (BPL, in blue) was found to be more statistically significant than the simple power-law (PL).

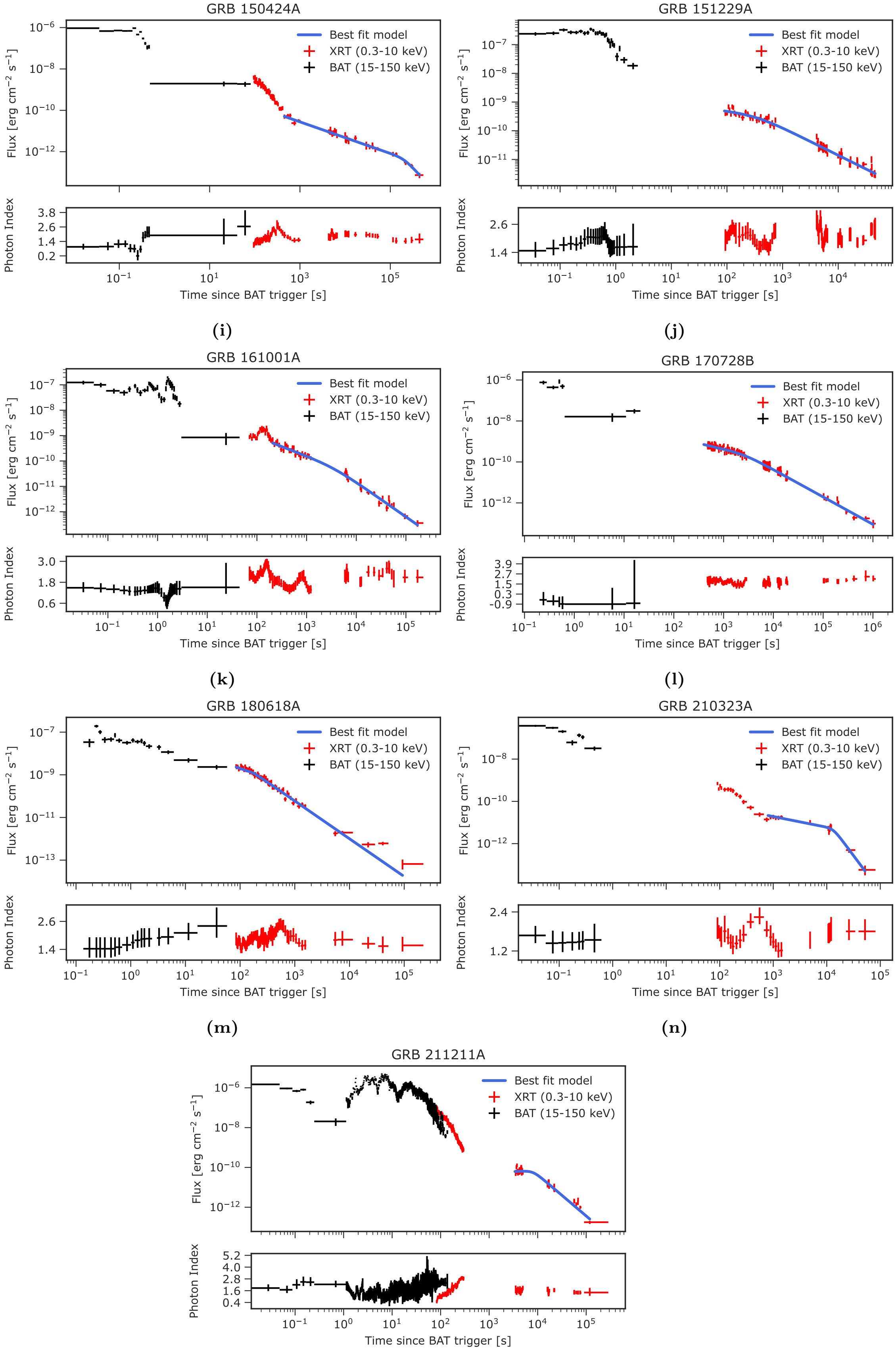

(i)

(j)

(k)

(l)

(m)

(n)

(o)

Figure A.2: *-continued*

A3: "EE-only" isotropic luminosity light-curves

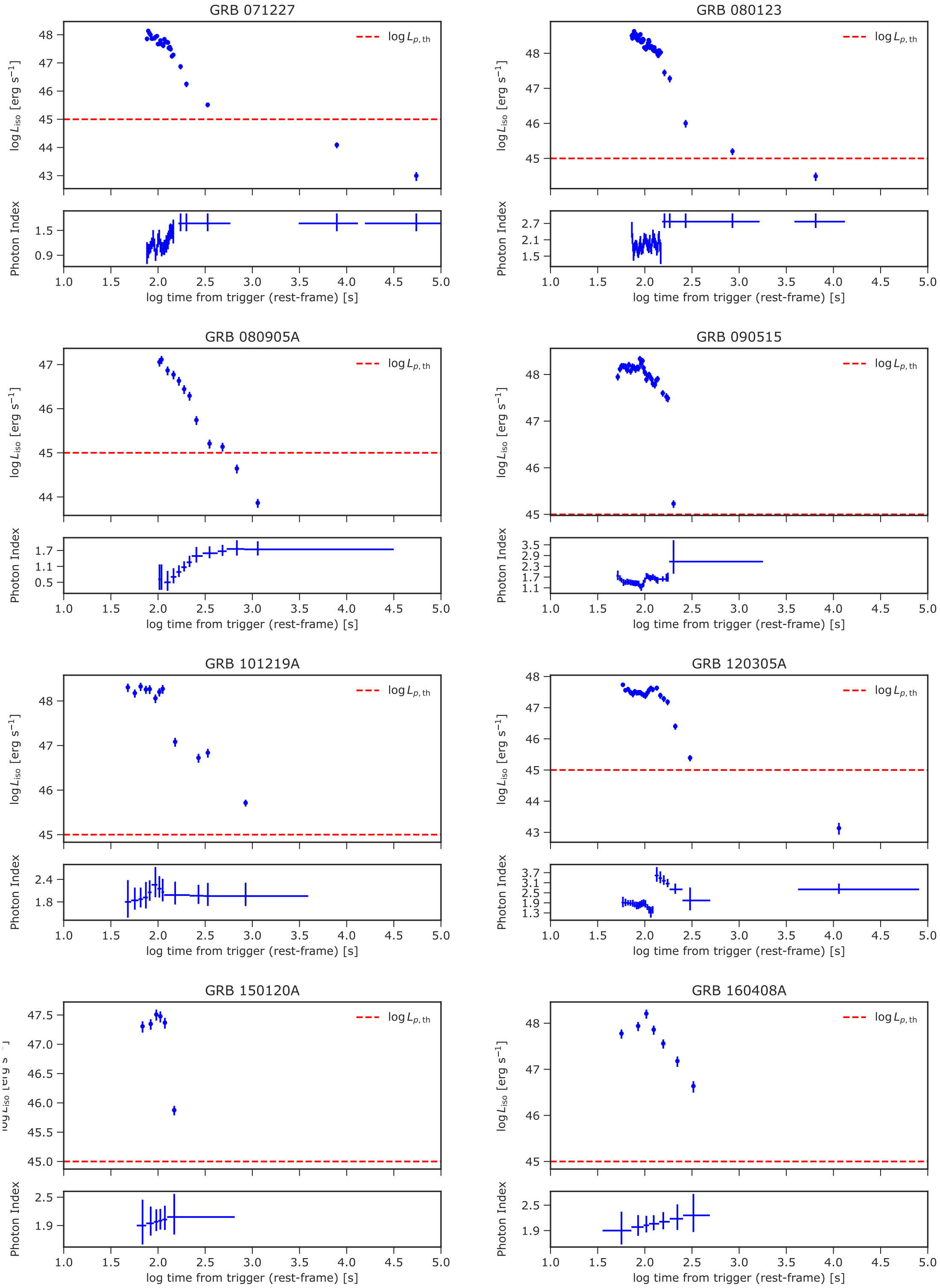

Figure A.3: Isotropic equivalent luminosity light-curves (rest frame) for some of the cases included in the "EE-only" subsample. The subplot shows the time behavior of the photon index Γ. These were extensively exploited in Section 4.3 to verify $L_{p,\mathrm{min}}$- and κ'-criteria. The red line indicate the threshold $L_{p,\mathrm{th}}$, defined in Eq.4.15.

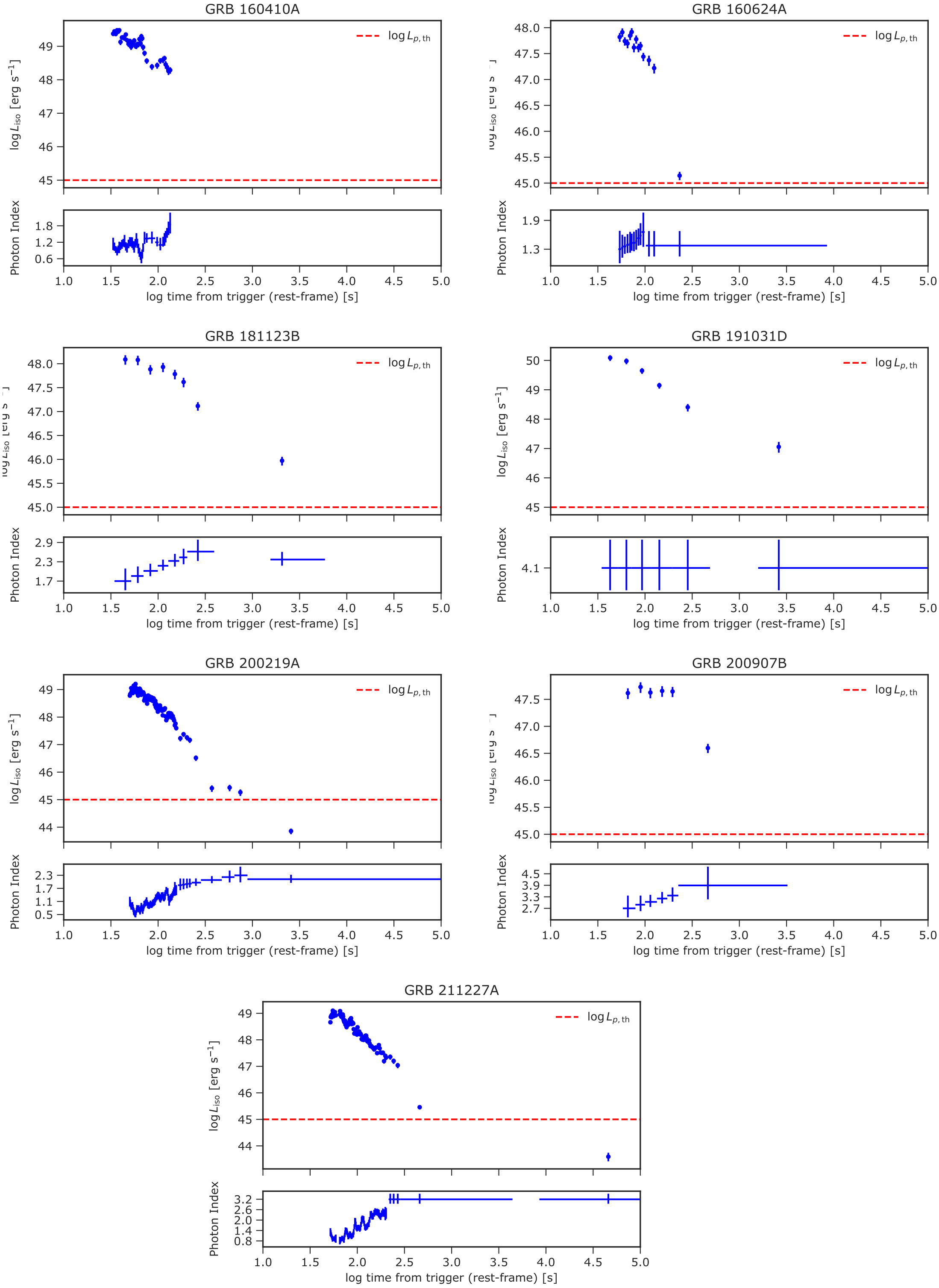

Figure A.3: *-continued*

A4: $M_{\max}$ computation python code

```python
"""
Created on Thu Nov 23 12:01:49 2023
@author: Luca Guglielmi
"""
import numpy as np
import numpy.polynomial.polynomial as pol
import statistics as st
from scipy.stats import norm
import matplotlib.pyplot as plt
plt.style.use('seaborn-ticks')
import pandas as pd

m_sun = 1.989e33   #solar mass in g

#PARAMETERS OF THE GAUSSIAN SAMPLE
mu = 1.33          #*m_sun, average NS mass in galactic distrib, ozel 2016
#mu = 1.32         # value from kilzilian2013
sigma = 0.09       #*m_sun, std for NS mass in galactic distrib, ozel2016
#sigma = 0.11      # value from kilzilian2013
n_sample = 100000 #number of outcomes that i want to generate
frac_min = 0.14117#min fraction of GRBs included in the magnetar subsample
frac_max = 0.2449 #max fraction of GRBs included in the magnetar subsample
m_ej = 0.          #mass of ejected material


#gaussian z score corresponding to the frac% left tail
z_min= norm.ppf(frac_min)
z_max= norm.ppf(frac_max)


#gravitational masses, what we measure from data,
#it's smaller than baryonic mass because it takes into
#account also the binding energy, negative contribute
m1_g = np.random.normal(mu, sigma, n_sample) #* m_sun
m2_g = np.random.normal(mu,sigma, n_sample) #* m_sun


#baryonic mass, real mass of the star, given
#by N_baryons*M_baryons, it is larger than the mass we measure
m1_b = m1_g  +  0.0602 * m1_g**2  +  0.0180 * m1_g**3
m2_b = m2_g  +  0.0602 * m2_g**2  +  0.0180 * m2_g**3
```

```

mu_b=  st.mean(m1_b)  #mean of the values of mtot_g
sigma_b  =  st.stdev(m1_b) #std of the values of mtot_g

#HERE I START THE FOR LOOP THAT COMPUTES THE VALUE OF Mmax FOR BOTH FRACTION AND FOR ALL THE VALUES OF Mej RANGING FROM 0 TO 0.01 Msun, INCREASING AT STEPS OF 0.005 Msun
import time
start=time.time()
for i in range(21):
    #baryonic mass of the remnant,
    mtot_b = m1_b + m2_b - m_ej

    mtot_b_mean =  st.mean(mtot_b)  #mean  of mtot_b
    mtot_b_std  =  st.stdev(mtot_b) #std of mtot_b

    #HERE I CALCULATE THE GRAVITATIONAL MASS OF THE REMNANT SOLVING A CUBIC EQUATION
    #i do a for loop because i want to act on all the outcomes i generated, mtot_g will be a list
    mtot_g = []
    for i in range(n_sample):
        coeff = [-mtot_b[i], 1, 0.0602, 0.0180] #list of the coefficients of the cubic equation
        poli = pol.Polynomial(coeff) #the object poli is my cubic equation
        roots = poli.roots()  #the method roots gives me a list of the three roots of the cubic equation, written as complex numer a + bj
        mtot_g.append(roots[2].real)          # i take  only the third root from the array because it is the only in the form a+0j (real solution) and i take only the real part and add it to the list

    #I convert mtot_g in an nparray, to do statistics on it
    mtot_g = np.array(mtot_g)
    mtot_g_mean =  st.mean(mtot_g)  #mean of the values of mtot_g
    mtot_g_std  =  st.stdev(mtot_g) #std of the values of mtot_g


    #Here i COMPUTE TH X VALUE CORRESPONDING TO THE z VALUE I IMPLEMENTED IN THE BEGINNIG z = x- mean/std
    m_gmax_1 = z_min * mtot_g_std + mtot_g_mean
    m_bmax_1 = z_min * mtot_b_std + mtot_b_mean

    m_gmax_2 = z_max * mtot_g_std + mtot_g_mean
    m_bmax_2 = z_max * mtot_b_std + mtot_b_mean
```

```


    #HERE I PLOT THE HISTOGRAM OF VALUES I OBTAINED AND I USE THE METHOD norm TO PLOT A CONTINUOUS GAUSSIAN DISTRIB WITH SAME MEAN AND STD

    fig = plt.figure()
    plt.hist(m1_g,bins=100,density=True, alpha=0.8, color='#FF7D40',label = r'Initial distrib, $\mu = $'+str("{0:.2f}".format(mu))+r', $\sigma =$'+str("{0:.2f}".format(sigma)))
    h=plt.hist(mtot_g, bins=100, density=True, alpha=0.6, color='b', label = r'Final distrib, $\mu = $'+str("{0:.2f}".format(mtot_g_mean))+r', $\sigma =$'+str("{0:.2f}".format(mtot_g_std)))
    plt.plot(h[1], norm.pdf(h[1],mtot_g_mean, mtot_g_std), color = 'r', label = r'Gauss, $\mu = $'+str("{0:.2f}".format(mtot_g_mean))+r', $\sigma =$'+str("{0:.2f}".format(mtot_g_std)),linewidth = 2)
    plt.vlines(m_gmax_1,0,3.2, linestyles='dashed', color = '#32CD32',label=r"$M_{g,max}$ = "+str("{0:.2f}".format(m_gmax_1))+r" $M_{\odot}\,(f_{plateau}=$"+str("{0:.2f}".format(frac_min*100))+"%)")
    plt.title(r'Initial and final $M_g$ distribution ($M_{ej}=$'+str("{0:.3f}".format(m_ej))+" $M_{\odot}$)")
    plt.xlabel(r'Initial and final $M_g$ [$M_{\odot}$]')
    plt.ylabel(r'Number (units of $10^3$)')
    plt.ylim([0,4.5])
    plt.legend(loc= 'upper center', fontsize=7)

    plt.savefig('./'+'14_'+str("{0:.3f}".format(m_ej))+'ej_magmassg.pdf', dpi = 600)
    print("For threshold at"+str("{0:.2f}".format(frac_min*100))+"% and mejecta ="+str("{0:.3f}".format(m_ej))+" Msun the maximum mass is ", m_gmax_1,"Msun")
    #plt.show()

    fig = plt.figure()
    plt.hist(m1_g,bins=100,density=True, alpha=0.8, color='#FF7D40',label = r'Initial distrib, $\mu = $'+str("{0:.2f}".format(mu))+r', $\sigma =$'+str("{0:.2f}".format(sigma)))
    h=plt.hist(mtot_g, bins=100, density=True, alpha=0.6, color='b', label = r'Final distrib, $\mu = $'+str("{0:.2f}".format(mtot_g_mean))+r', $\sigma =$'+str("{0:.2f}".format(mtot_g_std)))
    plt.plot(h[1], norm.pdf(h[1],mtot_g_mean, mtot_g_std), color = 'r', label = r'Gauss, $\mu = $'+str("{0:.2f}".format(mtot_g_mean))+r', $\sigma =$'+str("{0:.2f}".
```

```
        format(mtot_g_std)),linewidth = 2)
    plt.vlines(m_gmax_2,0,3.2, linestyles='dashed', color = '#32CD32',label=r"$M_{g,max}$ = "+str("{0:.2f}".format(m_gmax_2))+r" $M_{\odot}\,(f_{plateau}=$"+str("{0:.2f}".format(frac_max*100))+"%)")
    plt.title(r'Initial and final $M_g$ distribution ($M_{ej}=$'+str("{0:.3f}".format(m_ej))+" $M_{\odot}$)")
    plt.xlabel(r'Initial and final $M_g$ [$M_{\odot}$]')
    plt.ylabel(r'Number (units of $10^3$)')
    plt.ylim([0,4.5])
    plt.legend(loc= 'upper center', fontsize=7)

    plt.savefig('./'+'24_'+str("{0:.3f}".format(m_ej))+'ej_magmassg.pdf', dpi = 600)
    print("For threshold at"+str("{0:.2f}".format(frac_max*100))+"% and mejecta ="+str("{0:.3f}".format(m_ej))+"Msun the maximum mass is ", m_gmax_2,"Msun")


    m_ej+=0.005

end=time.time()
print("time=", end-start)
```

Listing A.1: Maximum stable mass computation code

Bibliography

Abbott, B. P. (Jan. 2019). “Properties of the Binary Neutron Star Merger GW170817”. In: *Phys. Rev. X* 9 (1), p. 011001.

Abbott, B. P. et al. (Oct. 2017). “Gravitational Waves and Gamma-Rays from a Binary Neutron Star Merger: GW170817 and GRB 170817A”. In: *The Astrophysical Journal Letters* 848.2, p. L13.

Achterberg, Abraham et al. (Dec. 2001). “Particle acceleration by ultrarelativistic shocks: theory and simulations”. In: *Monthly Notices of the Royal Astronomical Society* 328.2, pp. 393–408. ISSN: 0035-8711.

Ackermann, M. et al. (May 2010). “Fermi Observations of GRB 090510: a Short-Hard Gamma-Ray Burst with an Additional, Hard Power-Law component from 10 keV to GeV energies”. In: *The Astrophysical Journal* 716.2, p. 1178.

Aksulu, M D et al. (Jan. 2022). “Exploring the GRB population: robust afterglow modelling”. In: *Monthly Notices of the Royal Astronomical Society* 511.2, pp. 2848–2867. ISSN: 0035-8711.

Antoniadis, John et al. (2016). *The millisecond pulsar mass distribution: Evidence for bimodality and constraints on the maximum neutron star mass.*

Arnaud, K. et al. (2023). *XspecManual - HEASARC - NASA.* `https://heasarc.gsfc.nasa.gov/xanadu/xspec/manual/XspecManual.html`.

Baiotti, Luca, Bruno Giacomazzo, & Luciano Rezzolla (Oct. 2008). “Accurate evolutions of inspiralling neutron-star binaries: Prompt and delayed collapse to a black hole”. In: *Phys. Rev. D* 78 (8), p. 084033.

Band, D. et al. (Aug. 1993). “BATSE Observations of Gamma-Ray Burst Spectra. I. Spectral Diversity”. In: ApJ 413, p. 281.

Bauswein, A., S. Goriely, & H.-T. Janka (July 2013). “Systematics of Dyinamical Mass Ejection, Nucleosynthesis, and Radioactively Powered Electromagnetic Signals from Neutron-Star Mergers”. In: *The Astrophysical Journal* 773.1, p. 78.

Bauswein, Andreas, Oliver Just, et al. (Nov. 2017). “Neutron-star Radius Constraints from GW170817 and Future Detections”. In: *The Astrophysical Journal Letters* 850.2, p. L34.

Beniamini, Paz, Ramandeep Gill, & Jonathan Granot (June 2022). “Robust features of off-axis gamma-ray burst afterglow light curves”. In: *Monthly Notices of the Royal Astronomical Society* 515.1, pp. 555–570.

Beniamini, Paz, Kenta Hotokezaka, et al. (May 2019). “Formation rates and evolution histories of magnetars”. In: *Monthly Notices of the Royal Astronomical Society* 487.1, pp. 1426–1438.

Bernardini, Maria Grazia (Sept. 2015). “Gamma-ray bursts and magnetars: Observational signatures and predictions”. In: *Journal of High Energy Astrophysics* 7, pp. 64–72.

Bhattacharya, D. & E. P. J. van den Heuvel (Jan. 1991). “Formation and evolution of binary and millisecond radio pulsars”. In: Phys. Rep. 203.1-2, pp. 1–124.

Blackman, Eric G. & Insu Yi (Apr. 1998). “On Fueling Gamma-Ray Bursts and Their Afterglows with Pulsars”. In: *The Astrophysical Journal* 498.1, p. L31.

Blandford, R. D. & J. P. Ostriker (Apr. 1978). “Particle acceleration by astrophysical shocks.” In: ApJ 221, pp. L29–L32.

Bloom, Joshua S., Dale A. Frail, & Re’em Sari (June 2001). “The Prompt Energy Release of Gamma-Ray Bursts using a Cosmological k-Correction”. In: *The Astronomical Journal* 121.6, p. 2879.

Bucciantini, N. et al. (June 2006). “Relativistic magnetohydrodynamics winds from rotating neutron stars”. In: MNRAS 368.4, pp. 1717–1734.

Castro-Tirado, A. J. & Gorosabel, J. (1999). “Optical observations of GRB afterglows: GRB 970508 and GRB 980326 revisited ***”. In: *Astron. Astrophys. Suppl. Ser.* 138.3, pp. 449–450.

Cavallo, G. & M. J. Rees (May 1978). “A qualitative study of cosmic fireballs and gamma -ray bursts.” In: MNRAS 183, pp. 359–365.

Ciolfi, Riccardo et al. (Mar. 2017). “General relativistic magnetohydrodynamic simulations of binary neutron star mergers forming a long-lived neutron star”. In: *Physical Review D* 95.6.

Colgate, Stirling A. (Jan. 1974). “Early Gamma Rays from Supernovae”. In: ApJ 187, pp. 333–336.

Contopoulos, I. & A. Spitkovsky (Dec. 2006). “Modified pulsar spindown”. English (US). In: *Recent Advances in Astronomy and Astrophysics.* AIP Conference Proceedings. 7th International Conference of the Hellenic Astronomical Society ; Conference date: 08-09-2005 Through 11-09-2005, pp. 301–308. ISBN: 0735403430.

Costa, E. et al. (June 1997). “Discovery of an X-ray afterglow associated with the γ-ray burst of 28 February 1997”. In: Nature 387.6635, pp. 783–785.

Coulter, D. A. et al. (Dec. 2017). “Swope Supernova Survey 2017a (SSS17a), the optical counterpart to a gravitational wave source”. In: *Science* 358.6370, pp. 1556–1558.

Cucchiara, A. et al. (July 2011). “A Photometric Redshift of z ~9.4 for GRB 090429B”. In: ApJ 736.1, 7, p. 7.

Cummings, J. R. (Jan. 2015). “Short burst found in ground analysis of Swift-BAT data.” In: *GRB Coordinates Network* 17267, p. 1.

Dai, Z. G. & T. Lu (May 1998). “Gamma-ray burst afterglows and evolution of postburst fireballs with energy injection from strongly magnetic millisecond pulsars”. In: A&A 333, pp. L87–L90.

Dall’Osso, Simone & Luigi Stella (Jan. 2022). “Millisecond Magnetars”. In: *Astrophysics and Space Science Library*. Ed. by Sudip Bhattacharyya, Alessandro Papitto, & Dipankar Bhattacharya. Vol. 465. Astrophysics and Space Science Library, pp. 245–280.

Dall’Osso, Simone, Giulia Stratta, et al. (June 2023). “Magnetar Central Engines in Gamma-Ray Bursts Follow the Universal Relation of Accreting Magnetic Stars”. In: *The Astrophysical Journal Letters* 949.2, p. L32.

Dall’Osso, S et al. (2011). “Gamma-ray bursts afterglows with energy injection from a spinning down neutron star”. In: *Astronomy & Astrophysics* 526, A121.

Duncan, Robert C. & Christopher Thompson (June 1992). “Formation of Very Strongly Magnetized Neutron Stars: Implications for Gamma-Ray Bursts”. In: ApJ 392, p. L9.

Eichler, David et al. (July 1989). “Nucleosynthesis, neutrino bursts and γ-rays from coalescing neutron stars”. In: Nature 340.6229, pp. 126–128.

Endrizzi, A et al. (July 2016). “General relativistic magnetohydrodynamic simulations of binary neutron star mergers with the APR4 equation of state”. In: *Classical and Quantum Gravity* 33.16, p. 164001.

Escorial, Alicia Rouco et al. (2022). *The Jet Opening Angle and Event Rate Distributions of Short Gamma-ray Bursts from Late-time X-ray Afterglows.*

Evans, P. A., A. P. Beardmore, K. L. Page, J. P. Osborne, et al. (Aug. 2009). “Methods and results of an automatic analysis of a complete sample of Swift-XRT observations of GRBs”. In: MNRAS 397.3, pp. 1177–1201.

Evans, P. A., A. P. Beardmore, K. L. Page, L. G. Tyler, et al. (July 2007). “An online repository of Swift/XRT light curves of γ-ray bursts”. In: A&A 469.1, pp. 379–385.

Evans, P. A., R. Willingale, et al. (Sept. 2010). “The Swift Burst Analyser. I. BAT and XRT spectral and flux evolution of gamma ray bursts”. In: A&A 519, A102, A102.

Fishman, G. J. et al. (1994). “Discovery of Intense Gamma-Ray Flashes of Atmospheric Origin”. In: *Science* 264.5163, pp. 1313–1316.

Fong, W., E. Berger, & D. B. Fox (Jan. 2010). “Hubble Space Telescope Observations of Short Gamma-Ray Burst Host Galaxies: Morphologies, Offsets, and Local Environments”. In: ApJ 708.1, pp. 9–25.

Fong, W., E. Berger, R. Margutti, et al. (Dec. 2015). “A Decade of Short-duration Gamma-Ray Burst Broadband Afterglows: Energetics, Circumburst Densities, and Jet Opening Angles”. In: ApJ 815.2, 102, p. 102.

Fong, Wen-fai et al. (Nov. 2022). “Short GRB Host Galaxies. I. Photometric and Spectroscopic Catalogs, Host Associations, and Galactocentric Offsets”. In: ApJ 940.1, 56, p. 56.

Frail, D. A. et al. (Nov. 2001). “Beaming in Gamma-Ray Bursts: Evidence for a Standard Energy Reservoir”. In: ApJ 562.1, pp. L55–L58.

Gaensler, B. M. et al. (Apr. 2005). “An expanding radio nebula produced by a giant flare from the magnetar SGR 1806-20”. In: Nature 434.7037, pp. 1104–1106.

Galama, T. J. et al. (Oct. 1998). “An unusual supernova in the error box of the γ-ray burst of 25 April 1998”. In: Nature 395.6703, pp. 670–672.

Gehrels, N., G. Chincarini, et al. (Aug. 2004). “The Swift Gamma-Ray Burst Mission”. In: ApJ 611.2, pp. 1005–1020.

Gehrels, N., J. P. Norris, et al. (Dec. 2006). “A new γ-ray burst classification scheme from GRB 060614”. In: *Nature* 444.7122, pp. 1044–1046.

Gehrels, N., C. L. Sarazin, et al. (Oct. 2005). “A short γ-ray burst apparently associated with an elliptical galaxy at redshift z = 0.225”. In: Nature 437.7060, pp. 851–854.

Goldstein, A., R. D. Preece, et al. (Oct. 2013). “VizieR Online Data Catalog: The BATSE 5B GRB spectral catalog (Goldstein+, 2013)”. In: *VizieR Online Data Catalog*, J/ApJS/208/21, J/ApJS/208/21.

Goldstein, A., P. Veres, et al. (Oct. 2017). “An Ordinary Short Gamma-Ray Burst with Extraordinary Implications: Fermi-GBM Detection of GRB 170817A”. In: *The Astrophysical Journal Letters* 848.2, p. L14.

Granot, Jonathan (2006). *The Structure and Dynamics of GRB Jets.*

Hajela, A. et al. (Mar. 2022). “Evidence for X-Ray Emission in Excess to the Jet-afterglow Decay 3.5 yr after the Binary Neutron Star Merger GW 170817: A New Emission Component”. In: *The Astrophysical Journal Letters* 927.1, p. L17.

Harrison, F. A. et al. (Sept. 1999). “Optical and Radio Observations of the Afterglow from GRB 990510: Evidence for a Jet”. In: *The Astrophysical Journal* 523.2, p. L121.

Hjorth, Jens et al. (June 2003). “A very energetic supernova associated with the γ-ray burst of 29 March 2003”. In: Nature 423.6942, pp. 847–850.

Hotokezaka, K., E. Nakar, et al. (July 2019). “A Hubble constant measurement from superluminal motion of the jet in GW170817”. In: *Nature Astronomy* 3, pp. 940–944.

Hotokezaka, Kenta, Koutarou Kyutoku, et al. (June 2011). “Binary neutron star mergers: Dependence on the nuclear equation of state”. In: *Physical Review D* 83.12.

Kahn, S. M. & R. J. Blissett (Mar. 1979). “The Deconvolution of X-Ray Spectra: Refinements of the Blissett-Cruise Technique”. In: *Bulletin of the American Astronomical Society*. Vol. 11, p. 466.

Kalberla, P. M. W. et al. (Sept. 2005). “The Leiden/Argentine/Bonn (LAB) Survey of Galactic HI. Final data release of the combined LDS and IAR surveys with improved stray-radiation corrections”. In: A&A 440.2, pp. 775–782.

Kann, D.A. (2013). “Multi-Wavelength Observations of Short-Duration Gamma-Ray Bursts: Recent Results”. In: *EAS Publications Series* 61. Ed. by A.J. Castro-Tirado, J. Gorosabel, & I.H. Park, pp. 309–317.

Katz, J. I. (Sept. 1994). “Low-Frequency Spectra of Gamma-Ray Bursts”. In: ApJ 432, p. L107.

Kiziltan, Bülent et al. (Nov. 2013). “The Neutron Star Mass Distribution”. In: *The Astrophysical Journal* 778.1, p. 66.

Klebesadel, Ray W., Ian B. Strong, & Roy A. Olson (June 1973). “Observations of Gamma-Ray Bursts of Cosmic Origin”. In: ApJ 182, p. L85.

Kouveliotou, Chryssa et al. (Aug. 1993). “Identification of Two Classes of Gamma-Ray Bursts”. In: ApJ 413, p. L101.

Kovács, A. et al. (Jan. 2011). “Cosmology with Gamma-Ray Bursts Using k-correction”. In: *Acta Polytechnica* 51.1.

Kumar, Pawan & Bing Zhang (Feb. 2015). “The Physics of Gamma-Ray Bursts & Relativistic Jets”. In: *Physics Reports* 561, pp. 1–109.

Lattime, J & M Prakash (Apr. 2007). “Neutron star observations: Prognosis for equation of state constraints”. In: *Physics Reports* 442.1-6, pp. 109–165.

Lattimer, J.M. (2021). “Neutron Stars and the Nuclear Matter Equation of State”. In: *Annual Review of Nuclear and Particle Science* 71.1, pp. 433–464.

Lazzati, Davide et al. (June 2023). “GRB 191019A: A Short Gamma-Ray Burst in Disguise from the Disk of an Active Galactic Nucleus”. In: *The Astrophysical Journal Letters* 950.2, p. L20.

Li, Liang et al. (Sept. 2012). “A Comprehensive Study of Gamma-Ray Burst Optical Emission. I. Flares and Early Shallow Decay Component”. In: *The Astrophysical Journal* 758.1, p. 27.

Lien, Amy et al. (Sept. 2016). "The third Swift Burst Alert Telescope Gamma-Ray Burst Catalog". In: *The Astrophysical Journal* 829.1, p. 7.

Margalit, Ben & Brian D. Metzger (Nov. 2017). "Constraining the Maximum Mass of Neutron Stars from Multi-messenger Observations of GW170817". In: *The Astrophysical Journal Letters* 850.2, p. L19.

Meegan, Charles et al. (Sept. 2009). "The Fermi Gamma-ray Burst Monitor". In: ApJ 702.1, pp. 791–804.

Meszaros, P. (July 2006). "Gamma-ray bursts". In: *Reports on Progress in Physics* 69.8, pp. 2259–2321.

Meszaros, P. & M. J. Rees (Mar. 1993). "Relativistic Fireballs and Their Impact on External Matter: Models for Cosmological Gamma-Ray Bursts". In: ApJ 405, p. 278.

Mészáros, P. & M. J. Rees (Feb. 1997). "Optical and Long-Wavelength Afterglow from Gamma-Ray Bursts". In: ApJ 476.1, pp. 232–237.

— (2014). *Gamma-Ray Bursts.*

Metzger, B. D., D. Giannios, et al. (May 2011). "The protomagnetar model for gamma-ray bursts". In: *Monthly Notices of the Royal Astronomical Society* 413.3, pp. 2031–2056. ISSN: 0035-8711.

Metzger, Brian D., Todd A. Thompson, & Eliot Quataert (Mar. 2018). "A Magnetar Origin for the Kilonova Ejecta in GW170817". In: *The Astrophysical Journal* 856.2, p. 101. ISSN: 1538-4357.

Metzger, M. R. et al. (June 1997). "Spectral constraints on the redshift of the optical counterpart to the γ-ray burst of 8 May 1997". In: *Nature* 387.6636, pp. 878–880. ISSN: 1476-4687.

Minaev, P Y & A S Pozanenko (Dec. 2019). "The Ep,i–Eiso correlation: type I gamma-ray bursts and the new classification method". In: *Monthly Notices of the Royal Astronomical Society* 492.2, pp. 1919–1936. ISSN: 1365-2966.

Mukherjee, Soma et al. (Nov. 1998). "Three Types of Gamma-Ray Bursts". In: *The Astrophysical Journal* 508.1, pp. 314–327.

N. Aghanim, and et al. (Sept. 2020). "Planck 2018 results". In: *Astronomy & Astrophysics* 641, A6.

Nakar, E. (Apr. 2007). "Short-hard gamma-ray bursts". In: *Physics Reports* 442.1-6, pp. 166–236.

Narayan, Ramesh, Bohdan Paczynski, & Tsvi Piran (Aug. 1992). "Gamma-Ray Bursts as the Death Throes of Massive Binary Stars". In: ApJ 395, p. L83.

Norris, J. P. & J. T. Bonnell (May 2006). "Short Gamma-Ray Bursts with Extended Emission". In: *The Astrophysical Journal* 643.1, p. 266.

Norris, Jay P., Neil Gehrels, & Jeffrey D. Scargle (June 2010). “Threshold for Extended Emission in Short Gamma-Ray Bursts”. In: *The Astrophysical Journal* 717.1, pp. 411–419.

Nousek, J. A. et al. (May 2006). “Evidence for a Canonical Gamma-Ray Burst Afterglow Light Curve in the Swift XRT Data”. In: ApJ 642.1, pp. 389–400.

O’Connor, B et al. (July 2022). “A deep survey of short GRB host galaxies”. In: *Monthly Notices of the Royal Astronomical Society* 515.4, pp. 4890–4928.

Oganesyan, Gor et al. (Apr. 2020). “Structured Jets and X-Ray Plateaus in Gamma-Ray Burst Phenomena”. In: *The Astrophysical Journal* 893.2, p. 88.

Özel, Feryal & Paulo Freire (Sept. 2016). “Masses, Radii, and the Equation of State of Neutron Stars”. In: *Annual Review of Astronomy and Astrophysics* 54.1, pp. 401–440. ISSN: 1545-4282.

Paciesas, William S. et al. (June 1999). “The Fourth BATSE Gamma-Ray Burst Catalog (Revised)”. In: *The Astrophysical Journal Supplement Series* 122.2, pp. 465–495.

Paczynski, B. (Sept. 1986). “Gamma-ray bursters at cosmological distances”. In: ApJ 308, pp. L43–L46.

Paczyński, Bohdan (Feb. 1998). “Are Gamma-Ray Bursts in Star-Forming Regions?” In: ApJ 494.1, pp. L45–L48.

Piran, Tsvi (June 1999). “Gamma-ray bursts and the fireball model”. In: *Physics Reports* 314.6, pp. 575–667.

Piro, Anthony L., Bruno Giacomazzo, & Rosalba Perna (Aug. 2017). “The Fate of Neutron Star Binary Mergers”. In: ApJ 844.2, L19, p. L19.

Poolakkil, S. et al. (May 2021). “The Fermi-GBM Gamma-Ray Burst Spectral Catalog: 10 yr of Data”. In: *The Astrophysical Journal* 913.1, p. 60.

Popham, Robert, S. E. Woosley, & Chris Fryer (June 1999). “Hyperaccreting Black Holes and Gamma-Ray Bursts”. In: *The Astrophysical Journal* 518.1, p. 356.

Preece, R. D. et al. (Jan. 2000). “The BATSE Gamma-Ray Burst Spectral Catalog. I. High Time Resolution Spectroscopy of Bright Bursts Using High Energy Resolution Data”. In: *The Astrophysical Journal Supplement Series* 126.1, p. 19.

Rastinejad, Jillian C. et al. (Dec. 2022). “A kilonova following a long-duration gamma-ray burst at 350 Mpc”. In: Nature 612.7939, pp. 223–227.

Rezzolla, Luciano, Elias R. Most, & Lukas R. Weih (Jan. 2018). “Using Gravitational-wave Observations and Quasi-universal Relations to Constrain the Maximum Mass of Neutron Stars”. In: *The Astrophysical Journal Letters* 852.2, p. L25.

Rhoads, James E. (Nov. 1999). “The Dynamics and Light Curves of Beamed Gamma-Ray Burst Afterglows”. In: ApJ 525.2, pp. 737–749.

Ripa, J. & A. Meszaros (2015). “What is the Astrophysical Meaning of the Intermediate Subgroup of GRBs?” In.

Ronchini, S. et al. (July 2023). “Combined X-ray and optical analysis to probe the origin of the plateau emission in γ-ray burst afterglows”. In: *Astronomy & Astrophysics* 675, A117.

Rossi, A. et al. (Apr. 2020). “A comparison between short GRB afterglows and kilonova AT2017gfo: shedding light on kilonovae properties”. In: MNRAS 493.3, pp. 3379–3397.

Rosswog, Stephan (Mar. 2015). “The multi-messenger picture of compact binary mergers”. In: *International Journal of Modern Physics D* 24.05, p. 1530012.

Rowlinson, A. et al. (Apr. 2013). “Signatures of magnetar central engines in short GRB light curves”. In: MNRAS 430.2, pp. 1061–1087.

Ruderman, M. (Oct. 1975). “Theories of gamma -ray bursts.” In: *Seventh Texas Symposium on Relativistic Astrophysics*. Ed. by P. G. Bergman, E. J. Fenyves, & L. Motz. Vol. 262, pp. 164–180.

Ruiz, Milton et al. (June 2016). “Binary Neutron Star Mergers: a Jet Engine for Short Gamma-Ray Bursts”. In: *The Astrophysical Journal* 824.1, p. L6.

Salmon, Lána, Lorraine Hanlon, & Antonio Martin-Carrillo (2022). “Two Dimensional Clustering of Swift/BAT and Fermi/GBM Gamma-ray Bursts”. In: *Galaxies* 10.4. ISSN: 2075-4434.

Sari, Re’em, Ramesh Narayan, & Tsvi Piran (Dec. 1996). “Cooling Timescales and Temporal Structure of Gamma-Ray Bursts”. In: ApJ 473, p. 204.

Sari, Re’em, Tsvi Piran, & J. P. Halpern (July 1999). “Jets in Gamma-Ray Bursts”. In: ApJ 519.1, pp. L17–L20.

Sari, Re’em, Tsvi Piran, & Ramesh Narayan (Apr. 1998). “Spectra and Light Curves of Gamma-Ray Burst Afterglows”. In: ApJ 497.1, pp. L17–L20.

Shapiro, Stuart L. & Saul A. Teukolsky (1983). *Black holes, white dwarfs and neutron stars. The physics of compact objects.*

Shibata, Masaru & Kenta Hotokezaka (2019). “Merger and Mass Ejection of Neutron Star Binaries”. In: *Annual Review of Nuclear and Particle Science* 69.1, pp. 41–64.

Spitkovsky, Anatoly (Sept. 2006). “Time-dependent Force-free Pulsar Magnetospheres: Axisymmetric and Oblique Rotators”. In: ApJ 648.1, pp. L51–L54.

Stratta, Giulia et al. (Dec. 2018). “On the Magnetar Origin of the GRBs Presenting X-Ray Afterglow Plateaus”. In: *The Astrophysical Journal* 869.2, p. 155.

Tang, Chen-Han et al. (Oct. 2019). “Statistical Study of Gamma-Ray Bursts with a Plateau Phase in the X-Ray Afterglow”. In: *The Astrophysical Journal Supplement Series* 245.1, p. 1.

Troja, E. (Aug. 2020). *Swift: Swift Technical Handbook — swift.gsfc.nasa.gov.*

Troja, E. et al. (Oct. 2017). “The X-ray counterpart to the gravitational-wave event GW170817”. In: *Nature* 551.7678, pp. 71–74.

Tsvetkova, A., D. Frederiks, S. Golenetskii, et al. (Dec. 2017). “The Konus-Wind Catalog of Gamma-Ray Bursts with Known Redshifts. I. Bursts Detected in the Triggered Mode”. In: ApJ 850.2, 161, p. 161.

Tsvetkova, Anastasia, Dmitry Frederiks, Dmitry Svinkin, et al. (Feb. 2021). “The Konus-Wind Catalog of Gamma-Ray Bursts with Known Redshifts. II. Waiting-Mode Bursts Simultaneously Detected by Swift/BAT”. In: ApJ 908.1, 83, p. 83.

Usov, V. V. (June 1992). “Millisecond pulsars with extremely strong magnetic fields as a cosmological source of γ-ray bursts”. In: Nature 357.6378, pp. 472–474.

Woosley, S. E. (Mar. 1993). “Gamma-Ray Bursts from Stellar Mass Accretion Disks around Black Holes”. In: ApJ 405, p. 273.

Woosley, Stan (Dec. 2001). “Blinded by the light”. In: *Nature* 414.6866, pp. 853–854. ISSN: 1476-4687.

Yang, Bin et al. (June 2015). “A possible macronova in the late afterglow of the long–short burst GRB 060614”. In: *Nature Communications* 6.1, p. 7323. ISSN: 2041-1723.

Yi, Shuang-Xi et al. (June 2016). “Comprehensive Study of the X-Ray Flares from Gamma-Ray Bursts Observed by Swift”. In: *The Astrophysical Journal Supplement Series* 224.2, p. 20.

Yuanyue, Pan, Wang Na, & Zhang Chengmin (Apr. 2013). “Binary Pulsars in Magnetic Field versus Spin Period Diagram”. In: *arXiv e-prints*, arXiv:1304.2489, arXiv:1304.2489.

Zhang, Bin-Bin, En-Wei Liang, & Bing Zhang (Sept. 2007). “A Comprehensive Analysis of Swift XRT Data. I. Apparent Spectral Evolution of Gamma-Ray Burst X-Ray Tails”. In: *The Astrophysical Journal* 666.2, p. 1002.

Zhang, Bing (2018). *The Physics of Gamma-Ray Bursts.*

Zhang, Bing, Y. Z. Fan, et al. (May 2006). “Physical Processes Shaping Gamma-Ray Burst X-Ray Afterglow Light Curves: Theoretical Implications from the Swift X-Ray Telescope Observations”. In: ApJ 642.1, pp. 354–370.

Zhang, Bing & Peter Mészáros (May 2001). “Gamma-Ray Burst Afterglow with Continuous Energy Injection: Signature of a Highly Magnetized Millisecond Pulsar”. In: ApJ 552.1, pp. L35–L38.

Zhang et al. (June 2015). “An Analysis of Chandra Deep Follow-Up Gamma-Ray Bursts: Implications for Off-Axis Jets”. In: *The Astrophysical Journal* 806.1, p. 15.

Zhu, Si-Yuan et al. (June 2023). “The Intrinsic Statistical Properties and Correlations of Short Gamma-Ray Bursts”. In: ApJ 950.1, 30, p. 30.

Acknowledgments

I would like to express sincere gratitude to my supervisor Marcella Brusa, for the enthusiasm with which she supported me in the last months. I am also extremely thankful to both my co-supervisors, Giulia Stratta and Simone Dall'Osso, for all the calls we did, for all the questions they answered and for all the patience they had to follow me during the whole period during which I worked on this Thesis: Giulia, thank you also for all the coffees and biscuits you offered me; and Simone, thanks for all the calls and the e-mails, you answered even when you were on a train, a plane, a car or wherever, that was appreciated a lot.

I want to express sincere appreciation to Boris Sbarufatti for sharing his expertise on Swift-XRT data reduction procedure and for the time spent in explaining *Swift*'s data reduction and processing: it was extremely fascinating to understand the secrets behind this wonderful satellite and the people working on it.

Additionally, I thank all of my university colleagues and friends: this two years have been life-changing for me, and this is also thanks to all of you.

At last, I am endlessly grateful to my parents, because I am perfectly aware that dealing with me is not easy but you were there for me in every moment; and also my sister, who never forgets to remember me how "happy" she is of me being around: I am happy too, sis. And, at last, thanks to my grandparents because, even if you cannot tell me in person, I know you are proud of me.